UNIVERSITY OF TWENTE.

Faculty of Science and Technology
Faculty of Electrical Engineering, Mathematics
and Computer Science

Interfaces and Correlated Electrons
Mathematics of Computational Science

Modeling and Analysis of Layered Josephson junctions

Vincent Bosboom

Supervisors:
Dr. A.A. Golubov
Prof. Dr. Ir. J.J.W. van der Vegt
Dr. M.Yu. Kupriyanov

Graduation committee:
Dr. A.A. Golubov
Prof. Dr. Ir. J.J.W. van der Vegt
Prof. Dr. Ir. J.W.M. Hilgenkamp
Dr. M. Schlottbom
Dr. G.H.L.A. Brocks
Dr. F.P. Schuller

Abstract

In this thesis, we develop a quantitative 2D model describing the distribution of the supercurrent density and density of states in SN-N-NS type Josephson junctions. This model is based on the self-consistent solution of the quasi-classical Usadel equations using the finite element method. We investigate the influence of the proximity effect and the phase difference on the properties of the junction for various spatial dimensions and material parameters of the S and N materials. We show that these results are consistent with analytical solutions in the thin N layer limit and show logical behavior for a large range of junction parameters. We extend our model to the case of a junction with homogeneous in- and outflow current to investigate depairing effects in the superconducting electrodes. Furthermore, we extend our model to ferromagnetic junctions by including the effect of an exchange field, showing spin separation of the density of states and the occurrence of a 0-π transition. These results may assist in improving the design of nanoscale Josephson junctions for use in superconducting digital circuits.

Keywords: Usadel equations, critical current, proximity effect, density of states, ferromagnetism, finite element method

Acknowledgments

This thesis is the result of almost a year of hard work and it marks the end of six years as a student. I would definitely not have been able to finish this without the help and support of many people that deserve to be mentioned.

First of all, I want to thank my supervisors: Alexander Golubov, Jaap van der Vegt, and Mikhail Kupriyanov. Alexander, thank you for the great discussions we had. Amid all the numerical work I did, you always managed to provide me with new physical insights through small remarks that you made. Jaap, thank you for your optimism and all your advice. Even though the physics of this project was quite unfamiliar to you, you always gave many sharp comments on how to improve my code and all other parts of my thesis. Mikhail, thank you for joining our discussions all the way from Russia. Each meeting you managed to motivate me with your theoretical insights and your enthusiasm.

Furthermore, I want to thank all other members of my graduation committee: Hans Hilgenkamp, Matthias Schlottbom, Geert Brocks, and Frederic Schuller. Thank you for taking the time to read this somewhat lengthy thesis.

Also, I want to thank my parents and sister. Thank you for always believing in me and supporting me and for all the gezelligheid at home (and for paying my rent).

I want to thank all the wonderful people I met during my time as a student. You always helped me relax when I needed it, either with all the card games we played, the races we did together, or during all the other sometimes idiotic things we did together. You really made me enjoy my time as a student.

Lastly, I want to thank Pauline. You always helped me relax when my mind was full of math and were always able to convince me that things are going ok. Without you, the graduation would have definitely been much more stressful.

Contents

Chapter 1

Introduction

1.1 Motivation

In recent years, the field of superconducting electronics has seen rapid developments. These developments are motivated by the high energy efficiency and clock frequencies that superconducting electronic elements possess compared to standard electronics [1,2]. These superconducting elements can have widespread applications in electronics, for example as logic gates or memory elements [3]. One of the important problems in superconducting electronics is the downscaling of these elements. Superconducting elements are still relatively large compared to their semiconducting counterparts, which makes them impractical for many applications [4].

One of the main challenges in the scaling of superconducting electronics is the design of Josephson junctions, which are nonlinear elements of superconducting circuits. Ideally, these junctions should have high enough critical parameters such as I_c and the $I_C R_N$ product (where I_c is the critical current and R_N is the resistance of the junction in the non-superconducting state), and at the same time be scalable down to nanoscale sizes.

In the past decades, many different types of Josephson junctions have been invented. Mostly, as combinations of superconductors (S), insulators (I), normal non-superconducting metals (N), and other types of materials. A common type of Josephson junction is the sandwich superconductor/insulator/superconductor (SIS) junction. These junctions possess high critical currents, but are difficult to scale down, while ensuring the homogeneity of the junction required for large-scale production.

An alternative type of junction that can also sustain large currents is a superconductor/normal metal/superconductor (SNS) junction. In practice, these junctions, however, often have lower critical currents than SIS junctions

due to the suppression of the superconductivity inside the electrodes by the proximity effect. To remedy this problem junctions with a variable thickness geometry are often considered, where the junction consists of layers of different thicknesses. One of such junctions is the SN-N-NS junction, where the normal metal is placed underneath the electrodes. This type of junction seems promising for possessing high critical currents and good scalability [5]. Determining the exact properties of this type of junction is thus particularly interesting.

Theoretically, Josephson junctions are often described by one-dimensional models, constructed under specific assumptions on the junction geometry and interface parameters. These models often provide insightful analytical solutions, but are not suitable for all situations.

For junctions consisting of multiple layers, such as SN or SF type variable thickness junctions, the junction geometry can be quite complex and the interfaces between the layers cause complicated proximity coupling. These types of junctions can often only be described by one-dimensional models in a handful of limiting cases. For a more general analysis of these junctions, higher-dimensional models are required.

In recent years, the interest in higher-dimensional models of superconducting junctions has increased [6–10]. Numerical solutions of these models yield predictions of junction properties for non-trivial geometries and general values of interface parameters. These solutions allow for a better comparison with experiments than those of one-dimensional models. To our knowledge, the properties of the SN-N-NS junction have not yet been investigated in two dimensions. It is the goal of this thesis to do so.

1.2 Structure of the thesis

The structure of this thesis is as follows. In Chapter 2 we introduce the basic physical principles describing Josephson junctions and derive the equations and boundary conditions that can be used to model these junctions. In Chapter 3 we explain the basic principles of the finite element method, consider the weak formulation of the equations describing the SN-N-NS junction, and derive and illustrate the numerical discretization and iterative solution methods that can be used in a numerical model. In Chapter 4 we model the SN-N-NS Josephson junction and explore the distribution of supercurrents and the density of states inside the junction based on 1D and 2D numerical models. We compare our numerical results with analytical solutions derived for one-dimensional models and extend our treatment to the case of a junction with homogeneous current inflow. In Chapter 5 we extend our model on

the SN-N-NS junction to a ferromagnetic Josephson junction and investigate the effect of an exchange field on the current density and density of states inside the junction. In Chapter 6 we discuss our main findings, reflect on our research and provide an outlook for future work. In appendix A we give a more detailed derivation and description of the numerical methods we use throughout this thesis.

1.3 Remarks on notation

Before the start of this thesis, we wish to make a few remarks on the notation. In all equations the physical constants $\hbar$ and k_b have been omitted to coincide with the notation commonly used in literature. The reader should imagine an $\hbar$ in front of all frequency variables ($\omega = \hbar\omega$) and a k_b in front of all temperature variables ($T = k_bT$).

Secondly, often in this report variables will be normalized to a dimensionless form. After the introduction of a normalization all subsequent references to a variable, except in figures, will refer to the normalized variable. Furthermore, a full list of symbols used in this thesis can be found in appendix B for clarity.

Lastly, we wish to clarify some mathematical notation. In this thesis we will use ∇ and $\nabla\cdot$ to denote the gradient and divergence operators. In cases when these operators act on matrices, this operation is defined elementwise. Furthermore, we use the notation $\left(\nabla A\right)^2 \equiv \nabla A \cdot \nabla A$. Lastly we denote the conjugate of a variable B by B^*.

Chapter 2

Physical aspects

In this chapter we will introduce the basic physical principles underlying the SN-N-NS Josephson junction. We begin with a brief introduction to superconductivity and ferromagnetism and develop the theory of Green's functions for superconducting systems. Using these Green's functions we derive the Usadel equations and discuss appropriate boundary conditions to model Josephson junctions. Lastly, we give three parametrizations of the Usadel equations that are suitable for analytical and numerical solutions.

2.1 Superconductivity

In 1911 a remarkable discovery was made by Heike Kamerlingh Onnes. While performing measurements on solid mercury he discovered that its resistance would disappear once it was immersed in liquid helium of about 4.2 Kelvin [11]. He immediately recognized the importance of his discovery and called this new phenomenon the "superconductive state". This new state of matter turned out to display many other interesting phenomena such as the Meissner effect [12], which is the expulsion of magnetic fields from the superconductor.

After this initial discovery considerably more research has been done on these materials. Many theoretical models were constructed, including the London equations in 1935 [13], the Ginzburg-Landau theory of superconductivity in 1950 [14], the BCS-theory in 1957 [15] and the Gorkov equations in 1958 [16]. Experimentally, many different superconducting materials have been discovered with critical temperatures ranging from 10^{-4} to 135 Kelvin and superconductivity has found its way into a wide variety of applications. Eight times already the Nobel prize in physics has been awarded for work in the field of superconductivity and many more are likely to come in the future.

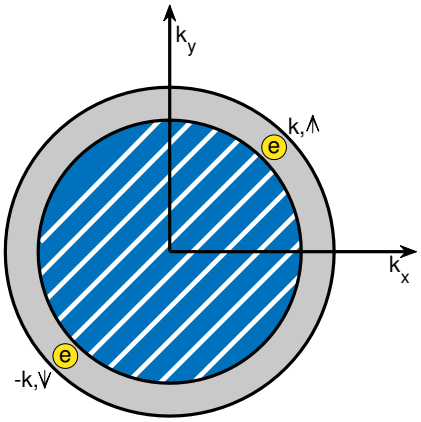

Figure 2.1: Depiction of the momentum space of a superconductor. k_x and k_y denote directions in momentum space. The blue region indicates the occupied states in a normal material. Two electrons with opposite spin and momentum combine to form a Cooper pair.

2.1.1 BCS Theory

The groundwork of the field of superconductivity was laid by the microscopic theory of Bardeen, Cooper, and Schrieffer (BCS) in 1957 [15]. They conjectured that in some materials through the interaction with the atomic lattice, two electrons with opposite spin and momentum can condense into a single *Cooper pair* [17], as shown in Figure 2.1.

This process of condensation is temperature-dependent. Below a critical temperature T_c it becomes energetically favorable for electrons to form these Cooper pairs. Since Cooper pairs have zero total spin they are Bosons and can thus all condense into the same ground state. Below the critical temperature thus a sudden phase transition takes place when all Cooper pairs condense into one state and the material becomes superconducting. One of the key properties of such a condensate is that it remains phase-coherent over long length scales and can be described by a superconducting phase φ.

Since it is energetically favorable to form Cooper pairs, the new superconducting ground state has a lower energy than the original ground state. This means that a finite energy is needed to break the Cooper pairs up into regular electrons. BCS superconductors are thus characterized by an *energy gap* Δ which separates the Cooper pairs and the normal electrons in energy. The magnitude of the energy gap is quite small, which explains why superconductivity occurs only at very low temperatures. This energy gap is also

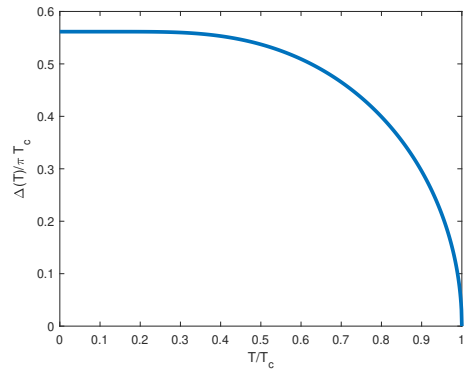

(a) Temperature dependence of the energy gap in BCS theory.

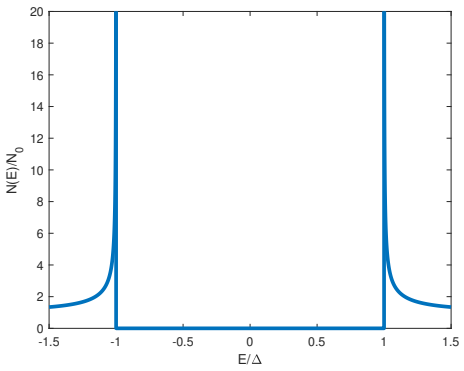

(b) Normalized density of states in BCS theory.

Figure 2.2

responsible for the most famous property of superconductors: perfect conductivity. Small currents do not provide enough energy to break the Cooper pairs and therefore flow through the superconductor without any resistance.

The magnitude of this energy gap Δ can be calculated self-consistently at any temperature T:

$$\ln \frac{T}{T_c} + 2\pi T \sum_{n=0}^{\infty} \left[\frac{1}{\epsilon_n} - \frac{1}{\sqrt{\epsilon_n^2 + \Delta^2}} \right] = 0, \tag{2.1}$$

where $\epsilon_n = (2n+1)\pi T$. This equation can be solved efficiently at every temperature [18]. At low temperatures the energy gap has a value of

$$\Delta(T \to 0) \approx 1.76 T_c, \tag{2.2}$$

while near the critical temperature it goes to zero as

$$\Delta(T \to T_c) \approx 1.74 \left(1 - \frac{T}{T_c}\right)^{1/2}. \tag{2.3}$$

The full dependence of the energy gap on temperature is shown in Figure 2.2a.

Another interesting quantity to calculate for superconductors is the *density of states* (DOS) $N(E)$, which describes the number of electronic states per unit volume that can be occupied in a superconductor at energy E.

To derive the DOS, suppose that we want to add one electron to the superconductor. Since it is a single electron its energy cannot be smaller than the energy gap Δ and can thus be written as

$$E = \sqrt{\xi^2 + \Delta^2}. \tag{2.4}$$

Since the total number of states doesn't change during a phase transition from the normal to the superconducting state, the density of states should satisfy

$$N(E)dE = N_0(\xi)d\xi. \tag{2.5}$$

with N_0 the density of states of the material in the normal state. For energies near the energy gap the normal density of states can be approximated by its value at the Fermi energy E_F, the energy of the highest occupied state: $N_0(\xi) \approx N_0(E_F)$. The superconducting density of states can then be calculated as

$$\frac{N(E)}{N_0} = \frac{d\xi}{dE} = \frac{E}{\sqrt{E^2 - \Delta^2}}, \qquad E > \Delta. \tag{2.6}$$

For $E < \Delta$ the density of states is zero because these states are occupied by the Cooper pairs. The complete DOS is thus

$$\frac{N(E)}{N_0} = \mathrm{Re}\left[\frac{E}{\sqrt{E^2 - \Delta^2}}\right]. \tag{2.7}$$

This is the density of states of a bulk superconductor according to BCS theory. The DOS is shown in Figure 2.2b. It contains two singularities at the energies $E = \pm\Delta$, which indicate the edges of the energy gap typical for superconductors, and reduces to the normal density of states for large energies.

2.1.2 Proximity effect

BCS theory describes a bulk superconductor without any interaction with its environment. Interesting effects occur, however, when a superconductor is put into contact with a normal metal. The Cooper pairs originating from the superconductor can penetrate the normal metal and induce superconducting effects. Simultaneously, this leakage of Cooper pairs into the normal metal leads to a reduction of the superconductivity in the superconductor itself as shown in Figure 2.3a. These two processes are, respectively, called the *proximity effect* and the *inverse proximity effect*. These effects occur only over small length scales in the normal and superconducting materials called the coherence lengths ξ_N and ξ_S.

The mechanism behind the proximity effect is *Andreev reflection* [19]. An electron in the normal metal incident at the interface with an energy below the energy gap cannot enter the superconductor, since it needs an extra available electron with opposite spin and momentum to form a Cooper pair.

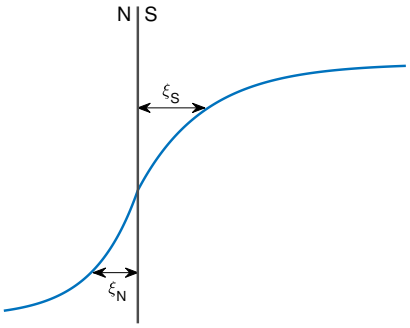

(a) Behavior of the Cooper pair density near a superconductor -normal metal (SN) interface.

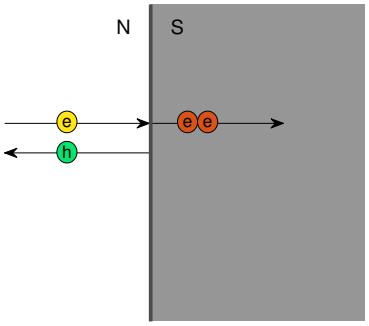

(b) Andreev reflection: an incoming electron (yellow) is retro-reflected into a hole (green) at a superconductor-normal metal (SN) interface with transmission of a Cooper pair (red).

Figure 2.3

Instead, due to Andreev reflection it is reflected back as a hole with opposite spin and momentum, while a Cooper pair is formed inside the superconductor as shown in Figure 2.3b. This process regulates the in- and outflow of Cooper pairs at the interface and is the origin of the proximity effect.

2.1.3 Josephson effect

One of the most interesting effects of superconductivity is the *Josephson effect*, first predicted theoretically by Brian Josephson in 1962 [20]. Josephson predicted that when two superconductors are separated by a small barrier made out of an insulating material, a small supercurrent I_s can run through the junction without requiring an applied voltage. The magnitude of this current depends on the sine of the phase difference φ between the wavefunctions of the two superconducting electrodes,

$$I_s = I_c \sin(\varphi). \tag{2.8}$$

The maximally attainable current I_c is called the *critical current*. Equation (2.8) is called the DC-Josephson effect and defines the *current-phase relationship* (CPR) of a junction.

The mechanism behind the Josephson effect is Andreev reflection. Consider an electron in the weak link region between the superconductors moving

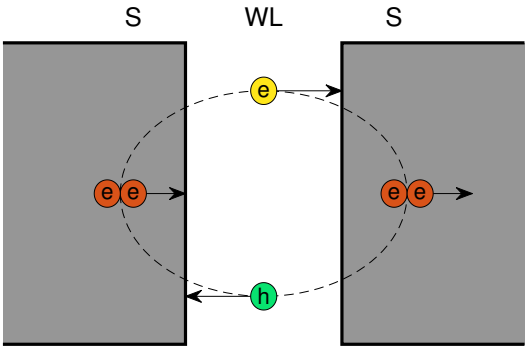

Figure 2.4: Current flow through a Josephson junction via Andreev reflection. An electron (yellow) and hole (green) in the weak link region (WL) are Andreev reflected at the boundaries with the superconductors (S) resulting in the transfer of a Cooper pair (red) through the junction.

towards one of the boundaries. At the boundary it is Andreev reflected into a hole with the transmission of a Cooper pair in the superconductor, this hole is then subsequently reflected back into an electron at the other interface, destroying a Cooper pair in the second superconductor, as depicted in Figure 2.4. Each cycle of this process thus transfers Cooper pairs between the superconductors resulting in a net supercurrent flow. Since the Andreev reflection amplitudes depend on the phases of the superconductors the resulting supercurrent will depend on the phase difference over the junction.

The Josephson effect does not only occur in junctions consisting of superconducting electrodes separated by an insulating layer (SIS junctions) as described by Josephson, but has also been observed in junctions containing a separation layer consisting of a normal non-superconducting material (SNS junctions), ferromagnetic materials (SFS junctions), junctions with some geometrical deformation in the center (SsS junctions) and many other junctions consisting of multiple layers of these materials. In general junctions, the current-phase relationship is not strictly sinusoidal, but takes on different forms depending on the layer types, geometry, and temperature of the junctions [21].

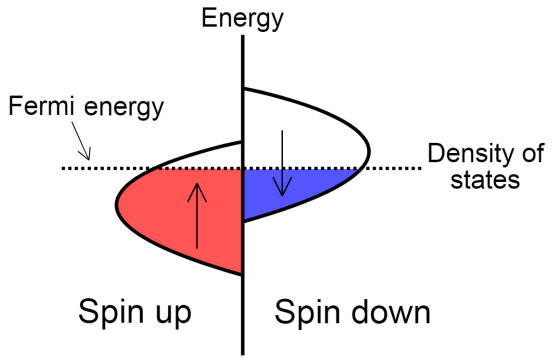

Figure 2.5: Exchange field induced splitting of the energy bands for different spins in a ferromagnet. From [22].

2.2 Ferromagnetism

Electrons carry not only a charge, but also a small magnetic moment, characterized by their spin, which can have two values, spin up and spin down. In normal metals the effect of spin can be neglected and both spin up and spin down electrons can occupy states with the same energies.

Spin is however an important factor in a process called exchange interaction. This process stems from the Pauli exclusion principle, which states that two particles cannot share the exact same quantum mechanical state. This implies that two electrons with equal spin cannot occupy the same orbital state.

In a crystal, where the orbitals of the different atoms overlap, electrons with equal spins thus tend to be further apart than electrons with opposite spins, due to this exclusion principle. This larger separation reduces the electrostatic energy between these electrons making the parallel orientation of the spins energetically favorable compared to the antiparallel orientation.

Materials with large exchange interactions are called *ferromagnetic materials*. In these materials the electrons tend to align their spins. The energy levels of the electrons with different spins are separated as shown in Figure 2.5. This separation between these energy levels is called the *exchange energy* H.

2.3 Green's functions

To find out the exact properties of a superconducting junction one needs to solve the Schrödinger equation for the system, including all interaction and potential terms for all particles in the junction. Because of the unimaginably

large number of particles in such a junction this approach is feasible neither analytically nor numerically. A better approach is to resort to *Green's functions*.

For a quantum many-body system the Green's function is defined as the probability amplitude to find the system in its ground state at time t_2 with an extra particle at position $\mathbf{r_2}$ if at time t_1 the system was in its ground state with an extra particle added at position $\mathbf{r_1}$ [23]. Formally this Green's function is defined as

$$G(\mathbf{r_1}, \mathbf{r_2}, t_1, t_2) = -i\Big\langle \Psi_0 \Big| \hat{T}\big[\hat{\psi}(\mathbf{r_2}, t_2)\hat{\psi}^\dagger(\mathbf{r_1}, t_1)\big] \Big| \Psi_0 \Big\rangle,$$

where Ψ_0 denotes the ground state of the system, $\hat{\psi}$ and $\hat{\psi}^\dagger$ are operators that, respectively, annihilate and create a particle at a specific position and time, the angle brackets define the inner product between two states and $\hat{T}$ is the time ordering operator, it ensures that the creation operator acts before the annihilation operator. It is defined as

$$\hat{T}\big[\hat{\psi}(\mathbf{r_2}, t_2)\hat{\psi}^\dagger(\mathbf{r_1}, t_1)\big] = \begin{cases} \hat{\psi}(\mathbf{r_2}, t_2)\hat{\psi}^\dagger(\mathbf{r_1}, t_1), & t_2 > t_1, \\ -\hat{\psi}^\dagger(\mathbf{r_1}, t_1)\hat{\psi}(\mathbf{r_2}, t_2), & t_1 > t_2. \end{cases}$$

Let $\Big|\Psi(\mathbf{r_i}, t_i)\Big\rangle$ denote the state of the system at position $\mathbf{r_i}$ and time t_i.The function G is called a Green's function because of the relation

$$\Big|\Psi(\mathbf{r_2}, t_2)\Big\rangle = \Big\langle G(\mathbf{r_1}, \mathbf{r_2}, t_1, t_2)\Big|\Psi(\mathbf{r_1}, t_1)\Big\rangle. \tag{2.9}$$

This relation is very similar to that of the regular Green's function considered in the study of linear differential equations.

For superconducting systems the spins of the added and annihilated particles are important, since Cooper pairs consist of electrons with opposite spin. In these systems the creation and annihilation operators must be extended to also include the spin degree of freedom: $\hat{\psi}^\dagger \to \hat{\psi}^\dagger_{\uparrow,\downarrow}$, $\hat{\psi} \to \hat{\psi}_{\uparrow,\downarrow}$, which respectively create and annihilate a particle with spin up or spin down.

Because the pairing between particles with opposite spin is so important in superconductors, Gorkov [16] defined two different Green's functions:

$$G_{1,2} = -i\Big\langle \hat{T}\big[\hat{\psi}_{2\uparrow}\hat{\psi}^\dagger_{1\uparrow}\big] \Big\rangle,$$
$$F_{1,2} = -i\Big\langle \hat{T}\big[\hat{\psi}_{2\uparrow}\hat{\psi}_{1\downarrow}\big] \Big\rangle.$$

Here we condensed the notation for the time and position indices to a single index and left out the ground state symbol. The first function is the regular

Green's function for spin up particles, while the second function, also called the anomalous Green's function, acts on particles with opposite spins. These two Green's functions can be combined into a 2x2 matrix function in so-called Nambu spin space [24] as

$$\hat{G}_{1,2} = -i\left\langle \hat{T}\left[\hat{\Psi}_2 \hat{\Psi}_1^\dagger\right]\right\rangle = \begin{pmatrix} G_{1,2} & F_{1,2} \\ F_{1,2}^\dagger & G_{1,2}^\dagger \end{pmatrix}.$$

Here $\hat{\Psi} = \begin{pmatrix} \hat{\psi}_\uparrow \\ \hat{\psi}_\downarrow^\dagger \end{pmatrix}$ and $\hat{\Psi}^\dagger = \begin{pmatrix} \hat{\psi}_\uparrow^\dagger & \hat{\psi}_\downarrow \end{pmatrix}$ are called the pseudo spinors. The daggers above the Green's functions indicate that the creation and annihilation operators have been swapped. Gorkov derived that this matrix Green's function satisfies the equation of motion

$$\begin{pmatrix} i\frac{\partial}{\partial t_1} + \frac{\nabla_1^2}{2m} + \mu & \Delta \\ -\Delta^* & -i\frac{\partial}{\partial t_1} + \frac{\nabla_1^2}{2m} + \mu \end{pmatrix} \hat{G}_{1,2} = \delta(1-2), \tag{2.10}$$

where i is the imaginary unit, m is the mass of an electron, μ is the chemical potential and Δ is the *pair potential* defined through the anomalous Green's function as

$$\Delta = \lambda \lim_{2 \longrightarrow 1} F_{1,2}.$$

Here, λ is the electron-phonon coupling constant.

Often the Hamiltonian of the system is time-independent and the Green's functions only depend on the time difference $t_2 - t_1$. In this setting it is more convenient to switch to the Fourier transformed Green's function

$$\hat{G}(\mathbf{r_1}, \mathbf{r_2}, E) = \frac{1}{2\pi} \int \hat{G}(\mathbf{r_1}, \mathbf{r_2}, t_2 - t_1) e^{iE(t_2 - t_1)} d(t_2 - t_1).$$

2.3.1 Quasiclassical approximation

In principle, the Gorkov equations (2.10) can be solved directly to determine the properties of superconducting systems, but in practice, these equations are numerically intractable. The reason is that the Gorkov Green's functions often contain oscillations in $|\mathbf{r_1} - \mathbf{r_2}|$ on length scales much smaller than the typical length of a superconducting junction. For superconducting junctions these oscillations are not significant and it is sufficient to look only at the dependence of the Green's functions on the center of mass coordinate $\mathbf{r} = (\mathbf{r_1} + \mathbf{r_2})/2$.

In this regime Larkin and Ovchinnikov [25] and Eilenberger [26] derived a quasiclassical version of the Fourier transformed Gorkov equations by integrating out the dependence of the Green's functions on the difference coordinate $|\mathbf{r_1} - \mathbf{r_2}|$:

$$\hat{g}(\mathbf{r}, k, E) = \frac{i}{\pi} \frac{1}{(2\pi)^3} \int \int \hat{G}_{1,2} e^{i\mathbf{k}\cdot(\mathbf{r_1}-\mathbf{r_2})} d(\mathbf{r_1} - \mathbf{r_2}) d\xi,$$

where $\xi = \frac{|\mathbf{k}|^2}{2m} - \mu$ and E is the energy. The full Green's function can be written in matrix form as

$$\hat{g} = \begin{pmatrix} g & f \\ f^\dagger & -g \end{pmatrix}.$$

This Green's function satisfies the so-called Eilenberger equation

$$\mathbf{v_F} \cdot \nabla_\mathbf{r} \hat{g} + [\hat{\tau}^3 E + i\hat{\Delta} - \frac{i}{\tau} <\hat{g}>, \hat{g}] = 0. \tag{2.11}$$

Here $\mathbf{v_F}$ is the Fermi velocity, τ is the impurity scattering time, square brackets denote the commutation operation and angular brackets denote averaging over the angle k. The matrices $\hat{\tau}^3$ and $\hat{\Delta}$ are defined as

$$\hat{\tau}^3 = \begin{pmatrix} 1 & 0 \\ 0 & -1 \end{pmatrix}, \qquad \hat{\Delta} = \begin{pmatrix} 0 & \Delta \\ \Delta^* & 0 \end{pmatrix}.$$

The value of Δ can be calculated from $\hat{g}$ using the so-called self consistency equation

$$\Delta \ln \frac{T}{T_c} - 2\pi T \sum_{n=0}^{\infty} \left(\frac{\Delta}{\omega_n} - <f> \right) = 0,$$

where the $\omega_n = (2n+1)\pi T$ are the Matsubara frequencies. The Eilenberger Green's function $\hat{g}$ satisfies the normalization condition

$$\hat{g}^2 = 1.$$

2.4 Usadel equations

Whenever a superconducting material satisfies the so-called dirty limit condition $l \ll \xi$, where l is the mean free path and ξ the superconducting coherence length, the Eilenberger equation can be further simplified into the

quasi-classical Usadel equation [27], which contains no angular dependence. The Usadel equation is a 2x2 matrix equation for the matrix $\hat{G}(\mathbf{r}, E)$:

$$-iD\nabla \cdot \left[\hat{G}\nabla\hat{G}\right] + \left[\hat{\tau}^3 E + i\hat{\Delta}, \hat{G}\right] = 0. \tag{2.12}$$

Here D is the diffusion constant of the material considered. For a thorough derivation of the Usadel equation see for example [28, 29]. The Green's function $\hat{G}$ satisfies the normalization condition

$$\hat{G}^2 = 1. \tag{2.13}$$

Because of this normalization condition the matrix contains only two independent components and can be written as

$$\hat{G} = \begin{pmatrix} G & F_1 \\ F_2 & -G \end{pmatrix}, \qquad G^2 + F_1 F_2 = 1.$$

We can distinguish multiple types of Green's functions depending on the value of the energy E. On the one hand we have the retarded Green's function $\hat{G}^R(E, \mathbf{r})$ for real values of E, which describe the energy-dependent properties of a system in thermal equilibrium, and on the other hand there is the thermal Green's function $\hat{G}^T(\omega_n, \mathbf{r})$ [30], which is defined only at the discrete imaginary energies $E = i\omega_n$.

This thermal Green's function can be used to calculate the stationary properties of a system. In general, the thermal Green's functions are much smoother than the retarded Green's functions and will not contain any oscillations or singularities.

The retarded Green's functions can be obtained from the thermal Green's functions by analytical continuation to real energies $\omega = -iE$. For this reason we will denote both Green's functions by $\hat{G}$. These Green's functions can be used to calculate different physical quantities; Using the thermal Green's function we can calculate the pair potential and the supercurrent density by summing over all Matsubara frequencies:

$$\Delta \ln \frac{T_c}{T} = \pi T \sum_{n=-\infty}^{\infty} \left[\frac{\Delta}{\omega_n} - F_1(\omega_n, \mathbf{r})\right], \tag{2.14}$$

$$\mathbf{J}(\mathbf{r}) = -\frac{i\pi}{2\rho_N e} T \sum_{n=-\infty}^{\infty} \mathrm{Tr}\left[\hat{\tau}^3 \hat{G}(\omega_n, \mathbf{r}) \nabla \hat{G}(\omega_n, \mathbf{r})\right]. \tag{2.15}$$

Here Tr denotes the trace operator, ρ_N is the resistivity of the material in the normal state and e is the elementary unit of charge. Using the retarded

Green's functions the density of states can be calculated as

$$N(E,\mathbf{r}) = \frac{1}{2}N_0 \,\mathrm{Tr}\left[\hat{\tau}^3 \,\mathrm{Re}\left\{\hat{G}(E,\mathbf{r})\right\}\right]. \tag{2.16}$$

Equations (2.12)-(2.14) together are commonly called the Usadel equations since they must be solved self-consistently to obtain the Green's functions. In order to solve the Usadel equations and calculate all relevant physical quantities the following procedure can be used

1. Solve equations (2.12)-(2.14) for the thermal Green's functions and determine $\Delta(\mathbf{r})$ and $\mathbf{J}(\mathbf{r})$.

2. Since Δ does not depend on ω, we use the obtained value of $\Delta(\mathbf{r})$ to solve the Usadel equations for the retarded Green's functions at all real energies E and calculate $N(E,\mathbf{r})$.

For the numerical solution of the Usadel equations it is convenient to parametrize the matrix $\hat{G}$ to provide a stable and convergent method. Different parametrizations can be used for the retarded and the thermal Green's functions.

2.4.1 Φ-parametrization

The thermal Green's functions are defined only at the imaginary energies $E = i\omega_n$. In this case the off-diagonal components of the Green's functions are complex conjugates and the Green's function $\hat{G}$ can be conveniently parametrized using the so-called Φ-parametrization [21]:

$$\hat{G}(\omega_n,\mathbf{r}) = \begin{pmatrix} \frac{\omega_n}{\sqrt{\omega_n^2+|\Phi|^2}} & \frac{\Phi}{\sqrt{\omega_n^2+|\Phi|^2}} \\ \frac{\Phi^*}{\sqrt{\omega_n^2+|\Phi|^2}} & -\frac{\omega_n}{\sqrt{\omega_n^2+|\Phi|^2}} \end{pmatrix}.$$

The function $\Phi(\omega_n,\mathbf{r})$ is in general a complex function. This parametrization automatically satisfies the normalization condition (2.13). Using this parametrization, equation (2.12) splits into four equations:

$$2\omega_n\Phi G - D\nabla\cdot\left[G^2\nabla\Phi\right] = 2\omega_n\Delta G, \tag{2.17}$$

$$2\omega_n\Phi^* G - D\nabla\cdot\left[G^2\nabla\Phi^*\right] = 2\omega_n\Delta^* G, \tag{2.18}$$

$$D\nabla\cdot\left[G^2(\Phi\nabla\Phi^* - \Phi^*\nabla\Phi)\right] = 2\omega_n G(\Delta\Phi^* - \Delta^*\Phi), \tag{2.19}$$

$$D\nabla\cdot\left[G^2(\Phi^*\nabla\Phi - \Phi\nabla\Phi^*)\right] = 2\omega_n G(\Delta^*\Phi - \Delta\Phi^*), \tag{2.20}$$

with $G = \frac{\omega_n}{\sqrt{\omega_n^2+|\Phi|^2}}$. For real values of ω_n these equations are not independent. Equation (2.18) is the conjugate of equation (2.17) and equations (2.19) and (2.20) are linear combinations of these two equations. This means that effectively one only needs to solve equation (2.17).

This equation must be supplemented by equation (2.14) to self-consistently calculate Δ, which in this parametrization can be written as:

$$\Delta \ln\left(\frac{T}{T_c}\right) + \pi T \sum_{n=-\infty}^{\infty} \left[\frac{\Delta}{\omega_n} - \frac{\Phi(\omega_n, \mathbf{r})}{\sqrt{\omega_n^2 + |\Phi|^2}}\right] = 0. \tag{2.21}$$

The supercurrent density inside the junction $\mathbf{J}(\mathbf{r})$ can be calculated as

$$\mathbf{J} = \frac{\pi}{2e\rho_N} \sum_{n=-\infty}^{\infty} \left[\omega_n^{-2} \operatorname{Im}(G_n^2 \Phi_n^* \nabla \Phi_n)\right], \tag{2.22}$$

with $G_n = G(\omega_n), \Phi_n = \Phi(\omega_n)$. For a numerical implementation of these equations it is convenient to write them in a dimensionless form. For this purpose we introduce the coherence length ξ and the normalized temperature t

$$\xi = \sqrt{\frac{D}{2\pi T_c}}, \qquad t = \frac{T}{T_c},$$

and proceed to normalize the quantities Φ_n, ω_n and Δ by πT_c and all lengths by ξ. Now the normalized Usadel equations can be written as

$$\omega_n \Phi_n G_n - \nabla \cdot \left[G_n^2 \nabla \Phi_n\right] = \omega_n \Delta G_n, \tag{2.23}$$

$$\Delta \ln(t) + t \sum_{n=-\infty}^{\infty} \left[\frac{\Delta}{\omega_n} - \frac{\Phi(\omega_n, \mathbf{r})}{\sqrt{\omega_n^2 + |\Phi|^2}}\right] = 0. \tag{2.24}$$

and the supercurrent through the junction can be calculated as

$$\frac{eR_N \mathbf{I_s}}{4\pi T_c} = tl \sum_{n=-\infty}^{\infty} \left[\omega_n^{-2} \operatorname{Im}(G_n^2 \Phi_n^* \nabla \Phi_n)\right], \tag{2.25}$$

where R_N is the resistance of the junction in the normal state given by

$$R_N = \frac{\rho_N L}{dW}, \tag{2.26}$$

with L, W and d are respectively the length, width and thickness of the junction. $\mathbf{I_s} = \mathbf{J_s} dW$ is the supercurrent through the junction and $l = \frac{L}{\xi}$.

In the Φ-parametrization the Usadel equations thus simplify into a single equation. In Chapter 3 we will however see that this simplicity also comes at a cost.

2.4.2 θ, χ-parametrization

The retarded Green's functions are defined for all real energies E. For real energies the quantity G in equation (2.17) is not always real and equations (2.17)-(2.20) in general cannot be solved simultaneously. Another choice of parametrization is thus needed. A convenient choice is the θ, χ-parametrization [31], which parametrizes the Green's function as

$$\hat{G} = \begin{pmatrix} \cos\theta & e^{i\chi}\sin\theta \\ e^{-i\chi}\sin\theta & -\cos\theta \end{pmatrix}.$$

Here θ and χ are complex functions that depend on the energy E and the position. Using this parametrization the four components of the Usadel equation can be written as

$$D\nabla\cdot\Big[\sin^2\theta\nabla\chi\Big] = i\sin\theta(\Delta e^{-i\chi} - \Delta^* e^{i\chi}), \tag{2.27}$$

$$D\Big[-\nabla^2\theta + \sin\theta\cos\theta(\nabla\chi)^2 - i\big((2-2\sin^2\theta)\nabla\theta\cdot\nabla\chi + \sin\theta\cos\theta\nabla^2\chi\big)\Big] = 2iE\sin\theta + 2\Delta\cos\theta e^{-i\chi}, \tag{2.28}$$

$$D\Big[-\nabla^2\theta + \sin\theta\cos\theta(\nabla\chi)^2 + i\big((2-2\sin^2\theta)\nabla\theta\cdot\nabla\chi + \sin\theta\cos\theta\nabla^2\chi\big)\Big] = 2iE\sin\theta + 2\Delta^*\cos\theta e^{i\chi}, \tag{2.29}$$

$$D\nabla\cdot\Big[\sin^2\theta\nabla\chi\Big] = i\sin\theta(\Delta e^{-i\chi} - \Delta^* e^{i\chi}). \tag{2.30}$$

These four equations can be reduced to two independent equations when summing equations (2.28) and (2.29):

$$D\nabla\cdot\Big[\sin^2\theta\nabla\chi\Big] = i\sin\theta(\Delta e^{-i\chi} - \Delta^* e^{i\chi}), \tag{2.31}$$

$$D\Big[-\nabla^2\theta + \sin\theta\cos\theta(\nabla\chi)^2\Big] = 2iE\sin\theta + \cos\theta(\Delta e^{-i\chi} + \Delta^* e^{i\chi}). \tag{2.32}$$

After applying normalization these equations can be written as

$$\nabla\cdot\Big[\sin^2\theta\nabla\chi\Big] = \frac{i}{2}\sin\theta\big(\Delta e^{-i\chi} - \Delta^* e^{i\chi}\big), \tag{2.33}$$

$$-\nabla^2\theta + \sin\theta\cos\theta(\nabla\chi)^2 = iE\sin\theta + \frac{1}{2}\cos\theta(\Delta e^{-i\chi} + \Delta^* e^{i\chi}). \tag{2.34}$$

From the solution of these equations at an energy E the local density of states normalized to N_0 can be calculated as

$$N(E,\mathbf{r}) = \mathrm{Re}\{\cos(\theta(E,\mathbf{r}))\}.$$

For strictly imaginary energies $E = i\omega$ the Φ- and θ, χ-parametrizations are related by the substitutions

$$\theta = \text{atan}(|\Phi|/\omega), \tag{2.35}$$

$$\chi = -i \ln\left(\frac{\Phi}{|\Phi|}\right), \tag{2.36}$$

$$\Phi = \omega \tan\theta e^{i\chi}. \tag{2.37}$$

2.4.3 Riccati parametrization

For real energy calculations for junctions with ferromagnetic layers the θ, χ-parametrization is not stable enough. For stability it is better to resort to the Riccati parametrization [32], in which the Usadel Green's functions are parametrized as

$$\hat{G} = \begin{pmatrix} (1+\alpha\beta)N & 2\alpha N \\ -2\beta N & -(1+\alpha\beta)N \end{pmatrix}, \tag{2.38}$$

where α and β are complex functions and $N = (1-\alpha\beta)^{-1}$. This parametrization is in general more stable than the θ, χ-parametrization because for real energies the functions α and β are bounded ($|\alpha|, |\beta| < 1$), whereas θ and χ are not necessarily.

Using the Riccati parametrization, the Usadel equations in (2.12) reduce to two equations for α and β:

$$-\nabla^2\alpha - 2N\beta\nabla\alpha\cdot\nabla\alpha = iE\alpha + \frac{\Delta}{2} - \alpha^2\frac{\Delta^*}{2}, \tag{2.39}$$

$$-\nabla^2\beta - 2N\alpha\nabla\beta\cdot\nabla\beta = iE\beta - \frac{\Delta^*}{2} + \beta^2\frac{\Delta}{2}. \tag{2.40}$$

2.4.4 Boundary conditions

The Usadel equations must be supplemented by suitable boundary conditions before they can be solved uniquely. These boundary conditions should reflect the physical situation. In this section we derive the boundary conditions needed for the junctions that we will consider in this thesis.

Boundary with insulator: In a superconductor, Cooper pairs can form and move around to create a supercurrent. These pairs can however not exist in an insulator outside of the superconductor. There can thus not be

any supercurrent flowing through a boundary separating the superconductor and the insulator. From equation (2.25) it can be seen that this no-current condition is satisfied by the condition

$$\nabla\Phi \cdot \mathbf{n} = 0, \tag{2.41}$$

where $\mathbf{n}$ is the outward normal vector of the boundary considered. Similarly, in the θ, χ-parametrization we have the conditions

$$\nabla\theta \cdot \mathbf{n} = 0, \tag{2.42}$$
$$\nabla\chi \cdot \mathbf{n} = 0. \tag{2.43}$$

In the Riccati parametrization this boundary condition reduces to

$$\nabla\alpha \cdot \mathbf{n} = 0, \tag{2.44}$$
$$\nabla\beta \cdot \mathbf{n} = 0. \tag{2.45}$$

Bulk superconductor: Far enough away from any phase gradients or other suppressive effects a superconductor will approach its equilibrium bulk state as described by BCS theory. In equilibrium there will be no current flowing through the superconductor. By neglecting the gradient terms in (2.23) it is clear that this bulk superconducting state is characterized by

$$\Phi = \Delta_0 e^{i\varphi}. \tag{2.46}$$

Here Δ_0 and φ are respectively the absolute value and the phase of the pair potential in the superconductor. Similarly in the θ, χ-parametrization we have the conditions

$$\cos\theta = \frac{E}{\sqrt{E^2 - \Delta_0^2}}, \tag{2.47}$$
$$\chi = \varphi. \tag{2.48}$$

In the Riccati parametrization the bulk solution is

$$\alpha = \frac{\Delta_0 e^{i\varphi}}{-iE + \sqrt{\Delta_0^2 - E^2}}, \tag{2.49}$$
$$\beta = \frac{-\Delta_0 e^{-i\varphi}}{-iE + \sqrt{\Delta_0^2 - E^2}}. \tag{2.50}$$

Boundary between two materials: At the boundary between two materials, which can be either two superconductor or two metals or a combination of these, the boundary condition must ensure the continuity of the supercurrent flowing through this boundary. The correct boundary conditions for the Usadel equations in this setting were derived in [33] to be

$$\gamma_B \xi_1 \hat{G}_1 \nabla \hat{G}_1 \cdot \mathbf{n} = \left[\hat{G}_1, \hat{G}_2\right], \tag{2.51}$$

$$\gamma \xi_1 \hat{G}_1 \nabla \hat{G}_1 = \xi_2 \hat{G}_2 \nabla \hat{G}_2. \tag{2.52}$$

Here $\hat{G}_1$ and $\hat{G}_2$ are the matrix Green's functions in material 1 and 2, respectively, ξ_i is the coherence length in material i, and γ_B and γ are dimensionless parameters denoting the effect of the interface and the proximity effect

$$\gamma_B = \frac{R_B}{\rho_1 \xi_1}, \qquad \gamma = \frac{\rho_2 \xi_2}{\rho_1 \xi_1},$$

where R_B is the interface resistance times area and ρ_i is the normal-state resistivity of material i. In the Φ-parametrization these boundary conditions can be written as

$$\gamma_B \xi_1 G_1 \nabla \Phi_1 \cdot \mathbf{n} = G_2(\Phi_2 - \Phi_1), \tag{2.53}$$

$$\gamma_B \xi_2 G_2 \nabla \Phi_2 \cdot \mathbf{n} = \gamma G_1(\Phi_1 - \Phi_2). \tag{2.54}$$

In the θ, χ-parametrization the boundary conditions become

$$\gamma_B \xi_1 \sin^2\theta_1 \nabla \chi_1 \cdot \mathbf{n} = \sin\theta_2 \sin\theta_1 \sin(\chi_2 - \chi_1), \tag{2.55}$$

$$\gamma_B \xi_2 \sin^2\theta_2 \nabla \chi_2 \cdot \mathbf{n} = \gamma \sin\theta_1 \sin\theta_2 \sin(\chi_1 - \chi_2), \tag{2.56}$$

$$\gamma_B \xi_1 \nabla \theta_1 \cdot \mathbf{n} = \sin\theta_2 \cos\theta_1 \cos(\chi_2 - \chi_1) - \cos\theta_2 \sin\theta_1, \tag{2.57}$$

$$\gamma_B \xi_2 \nabla \theta_2 \cdot \mathbf{n} = \gamma\left[\sin\theta_1 \cos\theta_2 \cos(\chi_1 - \chi_2) - \cos\theta_1 \sin\theta_2\right]. \tag{2.58}$$

In the Riccati parametrization they are given by

$$\gamma_B \xi_1 \nabla \alpha_1 \cdot \vec{n} = (\alpha_2 - \alpha_1)(1 - \alpha_1\beta_2) N_2, \tag{2.59}$$

$$\gamma_B \xi_1 \nabla \beta_1 \cdot \vec{n} = (\beta_2 - \beta_1)(1 - \beta_1\alpha_2) N_2, \tag{2.60}$$

$$\gamma_B \xi_2 \nabla \alpha_2 \cdot \vec{n} = \gamma(\alpha_1 - \alpha_2)(1 - \alpha_2\beta_1) N_1, \tag{2.61}$$

$$\gamma_B \xi_2 \nabla \beta_2 \cdot \vec{n} = \gamma(\beta_1 - \beta_2)(1 - \beta_2\alpha_1) N_1. \tag{2.62}$$

The boundary conditions (2.41)-(2.45) can be derived from these expressions in the limit $\gamma_B \to \infty$.

Chapter 3

Numerical Discretization of the Usadel Equations

In this chapter, we introduce the numerical methods used to solve the Usadel equations. We start by deriving the weak formulation of the Usadel equations for an SN-N-NS junction in the Φ-parameterization. Subsequently, we apply a finite element method with linear basis functions resulting in a system of nonlinear algebraic equations. Furthermore, we introduce three fixed-point methods that can be used to solve these nonlinear algebraic equations and check the convergence of our numerical method.

3.1 Weak formulation

There are many different numerical methods for solving PDEs. In this thesis we will consider the *finite element method* (FEM). The main reason why we choose this method is that it adapts very easily to different geometries, which is convenient when considering junctions with varying shapes. To illustrate the ideas behind FEM and our numerical procedure we consider the Usadel equations in the left superconducting electrode of an SN-N-NS junction as depicted in Figure 3.1 in the Φ-parametrization:

$$\omega_n \Phi_S G_S - \xi^2 \nabla \cdot \left[G_S^2 \nabla \Phi_S \right] = \omega_n \Delta G_S \qquad \text{in } S_1, \tag{3.1}$$

Subject to:

$$\nabla \Phi_S \cdot \mathbf{n} = 0 \qquad \text{on } \Gamma_I, \tag{3.2}$$

$$\xi \gamma_B G_S \nabla \Phi_S \cdot \mathbf{n} = \gamma G_N (\Phi_N - \Phi_S) \qquad \text{on } \Gamma_{SN}, \tag{3.3}$$

$$\Phi_S = \Delta_0 e^{-i\varphi/2} \qquad \text{on } \Gamma_-. \tag{3.4}$$

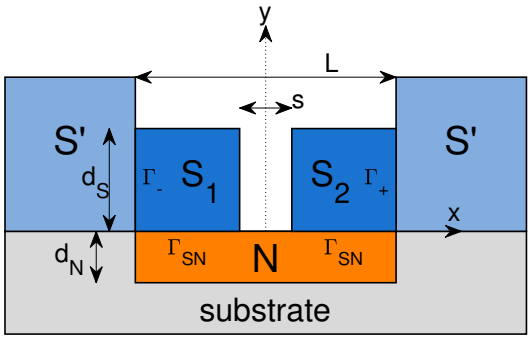

Figure 3.1: Sketch of the SN-N-NS junction. Dark blue regions indicate superconductors, the orange region denotes the non-superconducting metal, grey denotes a dielectric substrate, and light blue denotes bulk superconductors. All boundaries that are not labeled are denoted by Γ_I.

An explanation of the geometry of the SN-N-NS junction and the full Usadel equations in this junction will be given in Chapter 4, the solution procedures in other parametrizations are addressed in Appendix A.

For numerical purposes it is better to first rewrite our equations into a so-called *weak formulation* that allows us to relax the smoothness requirements and to seek a solution with only a first derivative in the space $H^1(S_1)$.

The function space $H^k(\Omega)$ on a domain Ω is called a Sobolev space and is defined as

$$H^k(\Omega) := \{u \in L^2(\Omega) \ : \ D^\alpha u \in L^2(\Omega), \ \forall |\alpha| \leq k\},$$

with $L^2(\Omega)$ the function space of square integrable functions over Ω, $\alpha = (\alpha_1, \ldots, \alpha_n)$ and

$$D^\alpha u = \frac{\partial^{|\alpha|} u}{\partial x_1^{\alpha_1} \ldots \partial x_n^{\alpha_n}},$$

To obtain the weak formulation, the PDE is multiplied by an arbitrary test function $\eta_S \in H_0^1(S_1)$, and integrated over the domain S_1,

$$-\xi^2 \int_{S_1} \eta_S \nabla \cdot \Big[G_S^2(\Phi_S) \nabla \Phi_S \Big] dS + \int_{S_1} \eta_S \omega_n \Phi_S G_S(\Phi_S) dS \tag{3.5}$$

$$= \int_{S_1} \eta_S \omega_n \Delta G_S(\Phi_S) dS. \tag{3.6}$$

Here $H_0^1(S_1)$ denotes the space of functions in $H^1(S_1)$ that have zero trace at Γ_-.

This formulation still requires the existence of the second derivative of the solution in the first term. To get rid of this second derivative, we employ the divergence theorem on this term:

$$\xi^2 \int_{S_1} G_S^2 \nabla \Phi_S \cdot \nabla \eta_S dS + \int_{S_1} \omega_n G_S \Phi_S \eta_S dS - \xi^2 \int_{\Gamma} \eta_S G_S^2 \nabla \Phi_S \cdot \mathbf{n} d\Gamma = \int_{S_1} \omega_n \Delta G_S \eta_S dS. \tag{3.7}$$

Here Γ denotes the full boundary of the domain S_1. By applying boundary conditions (3.2) and (3.3) and the properties of η_S, the resulting weak formulation is: Find $\Phi_S \in H^1(S_1)$ such that for all $\eta_S \in H_0^1(S_1)$

$$\xi^2 \int_{S_1} G_S^2 \nabla \Phi_S \cdot \nabla \eta_S dS + \int_{S_1} \omega_n G_S \Phi_S \eta_S dS + \frac{\xi\gamma}{\gamma_B} \int_{\Gamma_{SN}} G_S G_N \Phi_S \eta_S d\Gamma = \int_{S_1} \omega_n \Delta G_S \eta_S dS + \frac{\xi\gamma}{\gamma_B} \int_{\Gamma_{SN}} G_S G_N \Phi_N \eta_S d\Gamma. \tag{3.8}$$

In the weak formulation two types of boundary are enforced in different ways. At the boundary Γ_- Dirichlet boundary conditions are imposed, which require the test function η_S to be zero at this boundary, and are therefore called *essential* boundary conditions. At the other boundaries, the boundary conditions can be directly incorporated into the weak formulation and are therefore called *natural* boundary conditions.

The weak formulation is equivalent to the original formulation if the solution has sufficient regularity.

3.2 Elements and basis functions

The weak formulation is solved using a *Galerkin finite element method*. The domain S_1 is subdivided into *elements* $K \in \mathcal{T}_h$, with $\mathcal{T}_h$ a tessellation of non-overlapping elements covering S_1. The solution is represented using basis functions chosen from a finite element space V_h.

The definition of the finite element spaces V_h is a key choice in the finite element method. These spaces depend on the elements used to tessellate the domain. The index h of the space V_h denotes the size of these elements.

In this thesis, we will only consider triangular elements as shown in Figure 3.2. A function in the space V_h can then be defined element-wise as a polynomial over each element. Since we require our finite element solution

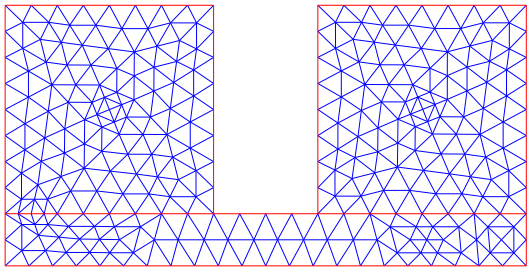

Figure 3.2: Subdivision of the domain of the SN-N-NS junction into triangular elements. Red lines indicate the boundaries of the different materials.

to converge to a solution in the space $H_1(S_1)$, the functions in V_h should be continuous at the element boundaries.

Since each function space V_h has a finite dimension $N_{S,h}$, it is spanned by a finite basis $\phi_{S,i}, i = 1, 2, \ldots, N_{S,h}$. The choice of this basis is not unique, but a requirement is that the basis functions overlap as little as possible, since this results in a sparse system of algebraic equations that can be solved efficiently.

In this thesis, we will only consider linear two-dimensional Lagrangian basis functions of the form

$$\phi_i(\mathbf{x}) = \alpha_i + \beta_i x + \gamma_i y.$$

An example basis function is sketched in Figure 3.3. On a triangular element with vertices $\mathbf{x}_1, \mathbf{x}_2, \mathbf{x}_3$ only three basis functions are nonzero. These can be computed by solving the following system of linear equations [34]

$$\begin{bmatrix} 1 & x_1 & y_1 \\ 1 & x_2 & y_2 \\ 1 & x_3 & y_3 \end{bmatrix} \begin{bmatrix} \alpha_1 & \alpha_2 & \alpha_3 \\ \beta_1 & \beta_2 & \beta_3 \\ \gamma_1 & \gamma_2 & \gamma_3 \end{bmatrix} = \begin{bmatrix} 1 & 0 & 0 \\ 0 & 1 & 0 \\ 0 & 0 & 1 \end{bmatrix}. \tag{3.9}$$

The function spaces V_h are thus defined as the spaces of continuous functions which are linear on each element, hence:

$$V_h := \{u \in C^0(S_1) \ : \ u|_K = \{\text{linear polynomial } \forall K \in \mathcal{T}_h\}\},$$

with C^0 the space of continuous functions on S_1.

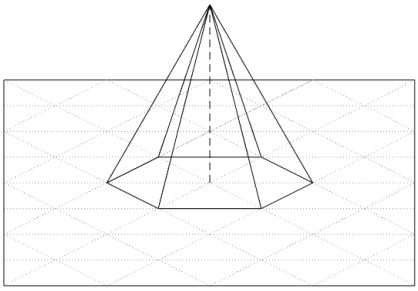

Figure 3.3: Sketch of a linear basis function on a triangular mesh.

3.3 Discretization

An approximate solution to the weak formulation (3.8) in the space V_h can be found by expanding into a set of basis functions:

$$\Phi_S \approx \Phi_{S_h}(\mathbf{r}) = \sum_{j=1}^{N_{S,h}} s_{1,j}\phi_{S,j}(\mathbf{r}). \tag{3.10}$$

Furthermore, the test function η_S was arbitrary and can thus be chosen equal to the basis functions $\phi_{S,i}$ for $i = 1, \ldots, N_{S,h}$.

Using this basis expansion the weak formulation (3.8) reduces to a finite set of algebraic equations for the coefficients $s_{1,j}$,

$$\big[S_1(s_1) + M_1(s_1) + B_1(s_1)\big]s_1 = f_1(s_1) + f_{B1}(s_1), \tag{3.11}$$

with

$$S_{1_{i,j}}(s_1) = \xi^2 \int_{S_1} \frac{\omega_n^2}{\omega_n^2 + |\sum_{k=1}^{N_{S,h}} s_{1,k}\phi_{S,k}|^2} \nabla\phi_{S,i}\nabla\phi_{S,j}dS, \tag{3.12}$$

$$M_{1_{i,j}}(s_1) = \int_{S_1} \frac{\omega_n^2}{\sqrt{\omega_n^2 + |\sum_{k=1}^{N_{S,h}} s_{1,k}\phi_{S,k}|^2}} \phi_{S,i}\phi_{S,j}dS, \tag{3.13}$$

$$B_{1_{i,j}}(s_1) = \frac{\xi\gamma}{\gamma_B} \int_{\Gamma_{SN}} \frac{\omega_n^2}{\sqrt{\omega_n^2 + |\sum_{k=1}^{N_{S,h}} s_{1,k}\phi_{S,k}|^2}\sqrt{\omega_n^2 + |\sum_{l=1}^{N_{N,h}} n_l\phi_{N,l}|^2}} \phi_{S,i}\phi_{S,j}d\Gamma, \tag{3.14}$$

$$f_{1_i}(s_1) = \int_{S_1} \frac{\Delta\omega_n^2}{\sqrt{\omega_n^2 + |\sum_{k=1}^{N_{S,h}} s_{1,k}\phi_{S,k}|^2}} \phi_{S,i} dS, \tag{3.15}$$

$$f_{B1_i}(s_1) = \frac{\xi\gamma}{\gamma_B} \int_{\Gamma_{SN}} \frac{\omega_n^2 \sum_{m=1}^{N_{N,h}} n_m \phi_{N,m}}{\sqrt{\omega_n^2 + |\sum_{k=1}^{N_{S,h}} s_{1,k}\phi_{S,k}|^2}\sqrt{\omega_n^2 + |\sum_{l=1}^{N_{N,h}} n_l\phi_{N,l}|^2}} \phi_{S,i} d\Gamma, \tag{3.16}$$

These matrices and vectors can be calculated efficiently in MATLAB using sparse matrix and vectorization techniques [35]. Since each basis function is unity at a specific node in our mesh the essential boundary condition in (3.4) can be straightforwardly implemented by fixing the coefficients of the basis functions corresponding to the nodes on this boundary.

The system of equations (3.11) with coefficients (3.12)-(3.16) is nonlinear and depends on the solution in the normal metal $\Phi_N \approx \sum_{k=1}^{N_{N_h}} n_k \phi_{N,k}$. To solve the Usadel equations in the SN-N-NS junction this system thus needs to be solved iteratively together with the system arising from the Usadel equations in the normal layer and the other superconducting electrode. We must therefore solve the following system

$$S(u)u = f(u), \tag{3.17}$$

subject to the essential boundary conditions

$$s_{1,2} = \Delta_0 e^{\mp i\varphi/2} \qquad \text{on } \Gamma_{\mp}, \tag{3.18}$$

with

$$S(u) = \operatorname{diag}\begin{pmatrix} S_1(u) + M_1(u) + B_1(u) \\ S_2(u) + M_2(u) + B_2(u) \\ S_N(u) + M_N(u) + B_N(u) \end{pmatrix},$$

$$u = \begin{pmatrix} s_1 \\ s_2 \\ n \end{pmatrix},$$

$$f(u) = \begin{pmatrix} f_1(u) + f_{B1}(u) \\ f_2(u) + f_{B2}(u) \\ f_{BN}(u) \end{pmatrix}.$$

Here the subscripts $1, 2$ and N denote, respectively, the first and second superconductor and the normal metal. This system of equations is nonlinear and therefore needs to be solved iteratively using a fixed-point method, but this can only be done after the integrals in S, u and f defined in (3.12)-(3.16) have been evaluated numerically.

3.4 Numerical integration

The integrals (3.12)-(3.16) in the finite element discretization cannot be computed analytically and we therefore have to resort to numerical integration techniques.

There are many types of numerical integration schemes available in literature. We use the *Gaussian quadrature* scheme, which has the advantage that it is especially efficient for integrals of polynomial functions. The Gaussian quadrature scheme approximates an integral over a domain Ω by a finite sum of the integrand at a specific set of points x_i with weights w_i,

$$\int_\Omega f(\mathbf{x})d\Omega \approx \frac{A_\Omega}{2}\sum_{i=1}^{n} w_i f(\mathbf{x}_i). \tag{3.19}$$

Here A_Ω denotes the area of the domain Ω.

For one-dimensional intervals the main power of Gaussian quadrature is that it can be used to calculate integrals of polynomials up to degree $2(n-1)$ exactly when at least n quadrature points are used. The exact weights and quadrature points are determined by the quadrature rule used. We use the Gauss-Legendre quadrature rule in 1D. The error of this quadrature rule is given by [36]

$$\int_a^b f(x)dx - \frac{b-a}{2}\sum_{i=1}^{n} w_i f(x_i) = \frac{(b-a)^{2n+1}(n!)^4}{(2n+1)[(2n)!]^3} f^{(2n)}(\eta), \tag{3.20}$$

for some $\eta \in (a,b)$, where a and b are the endpoints of the interval of integration.

In two dimensions the weights and points depend on the geometry of the integration domain Ω. For the triangular domains used in our calculations symmetric quadrature rules have been established by Dunavant [37]. In our code we use a 6 point quadrature rule, which is exact for polynomials up to fourth order and provides sufficient accuracy for our calculations.

3.5 Fixed-point iteration

In the finite element method nonlinear PDEs will be discretized into nonlinear systems of algebraic equations, which cannot be solved directly using basic linear algebra techniques. They should instead be solved iteratively using a *fixed-point iteration*. For a nonlinear system of equations of the form

$$S(u)u = f(u) \tag{3.21}$$

many different fixed-point techniques exist. The simplest method is the so-called *Picard method*. Given the nonlinear system defined by (3.21) and an initial guess u^0 the Picard method is given by

Algorithm 1: Picard method

Input: Initial guess $u^{(0)}$, system $S(u)u = f(u)$, tolerance tol
Output: Solution u up to the tolerance tol
Procedure:
$k = 0$;
Diff $= \infty$;
while *Diff* $>$ *tol* **do**
  $u^{(k+1)} = S^{-1}(u^{(k)})f(u^{(k)})$;
  Diff $= \left\|u^{(k+1)} - u^{(k)}\right\|_2$;
  $k = k + 1$;
end

There exists a very simple sufficient condition for convergence using the Banach fixed-point theorem. It can be shown that the Picard iteration converges linearly, meaning that the logarithm of the error of the approximation decreases linearly with the number of iterations.

Another frequently used fixed-point method is the *Newton method*. This is technically a root finding method, but can be turned into a fixed-point method by defining the function

$$h(u) = S(u)u - f(u).$$

The system of equations (3.21) can be solved by finding the roots of h using the Newton method shown in Algorithm 2

Algorithm 2: Newton method

Input: Initial guess $u^{(0)}$, function $h(u) = Su - f$, tolerance tol
Output: Solution u up to the tolerance tol
Procedure:
$k = 0$;
while $\left\|h(u^{(k)})\right\|_2 >$ *tol* **do**
  $J_{i,j} = \frac{\partial h_i(u^{(k)})}{\partial u_j^{(k)}}$;
  $u^{(k+1)} = u^{(k)} - J^{-1}h(u^{(k)})$;
  $k = k + 1$;
end

By the Banach-fixed point theorem linear convergence can also be shown for this method, but often even quadratic convergence can be achieved, which can make this method preferable over the Picard method.

A disadvantage of the Newton method is that it requires an accurate initial guess to converge. If the initial choice is chosen to far from the correct solution, subsequent iterations might jump over the solution and diverge [38]. To account for this problem the Newton method can be extended with a line search method to determine how far the next iteration should lie from the current iterative solution as in Algorithm 3

Algorithm 3: Newton method with line search

Input: Initial guess $u^{(0)}$, function $h(u) = Su - f$, tolerance tol
Output: Solution u up to the tolerance tol
Procedure:
$k = 0$;
while $\left\|h(u^{(k)})\right\|_2 > tol$ **do**
  $J_{i,j} = \frac{\partial h_i(u^{(k)})}{\partial u_j^{(k)}}$, $p_k = -J^{-1}h$;
  $\alpha = 1$;
  $\tilde{u} = u^{(k)} + \alpha p_k$;
  while $\|h(\tilde{u})\|_2 > (1 - 10^{-4}\alpha)\left\|h(u^{(k)})\right\|_2$ **do**
    $\alpha = \alpha/2$;
    $\tilde{u} = u^{(k)} + \alpha p_k$;
  end
  $u^{(k+1)} = \tilde{u}$;
  $k = k + 1$;
end

The condition in the while loop is called the condition of sufficient decrease. The coefficient 10^{-4} in front of the step size α is chosen to make this condition as easy as possible to satisfy. We chose the value 10^{-4} following literature [38, 39].

In some cases both the Picard method and the Newton method will not converge to the correct solution or the convergence is very slow. One reason may be that the current iterate is so far from the correct solution that a step in the computed descent direction only makes the approximation solution worse. In this case it can help to mix the descent directions from multiple previous iterations to balance out these errors. A frequently used accelera-

tion method is the *Anderson acceleration* method [40], which is applied to the Picard method, given by Algorithm 4

Algorithm 4: Anderson accelerated Picard method

Input: Initial guess $u^{(0)}$, $m \geq 1$, fixed point function $g(u)$, tolerance tol

Output: Solution u up to the tolerance tol

Procedure:

$c = 1$;
$u^{(1)} = g(u^{(0)})$;
$Diff = \left\| u^{(1)} - u^{(0)} \right\|_2$;
$k = 1$;
while $Diff > tol$ **do**
  $m_k = \min(m, c)$;
  $g_k = g(u^{(k)}), \quad f_k = g_k - u^{(k)}$;
  $F_k = (\Delta f_{k-m_k}, \ldots, \Delta f_{k-1})$, where $\Delta f_{k-1} = f_k - f_{k-1}$;
  $G_k = (\Delta g_{k-m_k}, \ldots, \Delta g_{k-1})$, where $\Delta g_{k-1} = g_k - g_{k-1}$;
  $\gamma^{(k)} = \arg\min \|f_k - F_k\gamma\|_2^2$;
  $u^{(k+1)} = g_k - G_k\gamma^{(k)}$;
  $Diff = \left\| u^{(k+1)} - u^{(k)} \right\|_2$;
  $k = k + 1$;
  if $mod(k, m) = 0$ **then**
    c = 1;
  end
  else
    c = c+1;
  end
end

The last six lines of the pseudo code perform a restart of the Anderson acceleration, which has been shown to improve convergence [41].

For the system of equations (3.17) resulting from the Usadel equations on the SN-N-NS bridge in the Φ-parametrization we can test the performance of the different fixed-point methods. There is, however, one small problem; the Newton method cannot be applied to this system. The reason is that the matrix S contains terms proportional to the absolute value of the solution. These terms are not differentiable over the complex numbers, prohibiting us from calculating the Jacobian matrix needed in Algorithm 3.

To overcome this problem we split u into its real and imaginary part and

write equation (3.17) as

$$\hat{S}(\hat{u})\hat{u} = \hat{f}(\hat{u}), \tag{3.22}$$

with

$$\hat{u} = \begin{pmatrix} \mathrm{Re}(u) \\ \mathrm{Im}(u) \end{pmatrix}, \ \hat{f} = \begin{pmatrix} \mathrm{Re}(f) \\ \mathrm{Im}(f) \end{pmatrix}, \ \hat{S} = \begin{pmatrix} \mathrm{Re}(S) & -\mathrm{Im}(S) \\ \mathrm{Im}(S) & \mathrm{Re}(S) \end{pmatrix}.$$

System (3.22) is holomorphic with respect to the real and imaginary parts of u and the Newton method can readily be applied. The downside is that we now have twice as many equations to solve. One could say that the non-differentiability of equation (3.17) is the price you pay for using a one-parameter parametrization.

A comparison of the performance of the different fixed-point methods applied to the system in (3.17) shown in Figure 3.4.

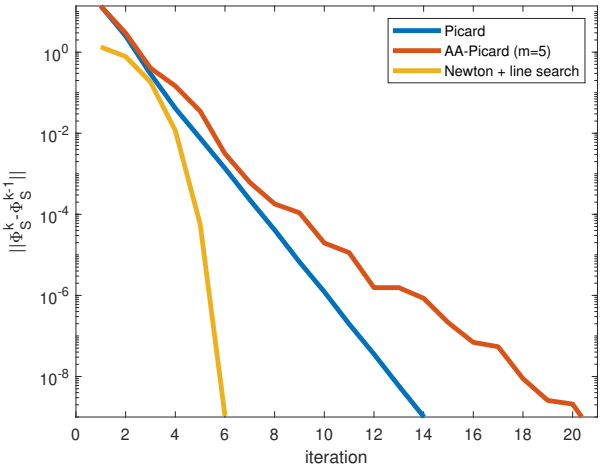

Figure 3.4: Rate of convergence of different fixed-point algorithms for solving the system in (3.17).

It can be seen that all fixed-point methods converge to a approximate solution. As predicted, the Picard iteration converges linearly, while the Newton method converges quadratically. The Anderson method does not seem to improve the convergence of the Picard iteration, and even reduces the rate of convergence. This makes sense given the fact that the Picard method has no problem converging whatsoever. The Newton method is slightly slower than the Picard method in terms of computation time because it induces a

larger system of equations and requires a line search, which is computationally more expensive. Therefore in the Φ-parametrization the Picard iteration is our method of choice.

In Appendix A the fixed-point methods are compared for other parametrizations of the Usadel equations and it is shown that in many cases the Picard iteration does not converge at all and that a Newton method with line search is required to solve the Usadel equations.

3.6 Convergence analysis

In order to solve the Usadel equations numerically we need to discretize the PDE by introducing the finite element spaces V_h. This discretization induces an error compared to the real solution of the Usadel equations, because on each element the solution is approximated by linear polynomials. The interpolation error should in general decrease as h decreases i.e. by using a finer mesh.

To obtain bounds on this error we need to define two length scales on a triangular element K:

$$h_K = \text{Diameter of } K := \sup_{x,y \in K} |x - y|,$$

$$\rho_K = \text{Supremum of the diameters of the circles inscribed in } K.$$

We call a mesh *regular* if for successive mesh refinements $h_K \to 0$ and there exists a constant σ independent of K such that $\frac{h_K}{\rho_K} \leq \sigma$.

Furthermore, given a function $v : K \to \mathbb{R}$ and the vertices $(\mathbf{x_1}, \mathbf{x_2}, \mathbf{x_3})$ of K, let

$$\Pi_K v = \sum_{i=1}^{3} v(\mathbf{x_i})\phi_i$$

denote the *interpolation operator* on K. Furthermore we define the norm on the Sobolev spaces

$$\|u\|_{H^k(\Omega)} = \left(\sum_{|\alpha| \leq k} \int_\Omega |D^\alpha u|^2 d\Omega \right)^{\frac{1}{2}}.$$

With these definitions in place, we can look at the error induced by the Lagrangian basis functions. For these basis functions the following theorem holds.

Theorem 1 (Interpolation error).

Let $\mathcal{T}_h$ be a tessellation of the domain Ω such that all triangular elements are regular, and let h be the maximum over all triangle diameters. Furthermore, let Π_K be the interpolation operators defined on the elements by first order Lagrangian basis functions, then there exists a constant C independent of the triangle shapes such that for all functions $v \in H^2(\Omega)$,

$$\|v - \Pi_K v\|_{L^2(\Omega)} \leq Ch^2 \|v\|_{H^2(\Omega)} .$$

Proof See for example [42].

The interpolation error gives an upper bound for the convergence rate that can be expected for the finite element discretization. A theoretical bound for the total error requires, however, also a bound for the discretization error, but this analysis is beyond the scope of this thesis. We will only investigate the convergence rate by comparing the numerical solutions with analytical solutions.

For smooth solutions the L^2-norm of the interpolation error induced by the linear Lagrangian basis functions should decrease quadratically with the mesh size. Before we can trust our numerical results we must verify that this is indeed the case in our calculations.

As a verification we show in Figure 3.5 the dependence on the mesh size of the numerically calculated L^2-norm of the difference between Green's function Φ_S in the right superconducting electrode of the junction and the analytical solution

$$\Phi_S = \Delta_0 e^{i\varphi/2}$$

in the limit $\gamma = 0$. This norm appears to go to zero as the mesh size decreases. From the slope it can clearly be seen that the convergence is indeed quadratic.

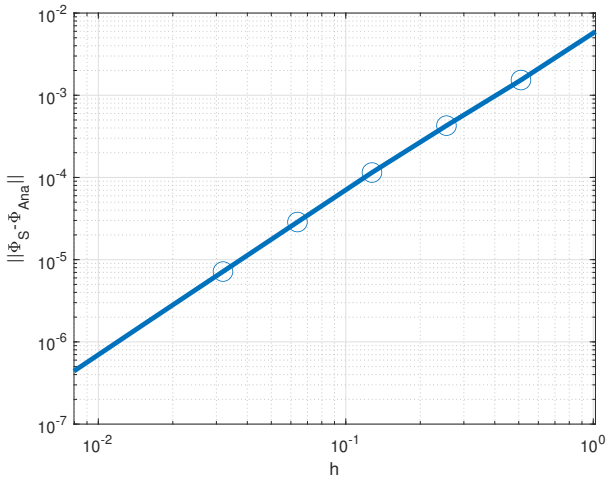

Figure 3.5: L^2-norm of the interpolation error of the solution inside the superconductor as a function of the triangle diameter h. The open circles denote numerically calculated values. The blue line denotes a quadratic fit.

Chapter 4

SN-N-NS Junction

In this chapter, we will apply our numerical methods to solve the Usadel equations in the SN-N-NS junction and to calculate the dependence of the current density and density of states on the junction parameters in one and two dimensions. Furthermore, we will validate our results with analytical solutions derived in the 1D limit. Lastly, we will extend our model to a junction with homogeneous current in- and outflow to search for depairing effects in the superconducting electrodes.

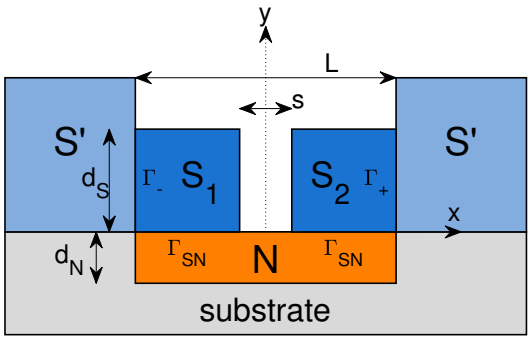

Figure 4.1: Sketch of the SN-N-NS junction. The superconducting material (dark blue) and normal metal (orange) are deposited on a dielectric substrate (grey). Far away from the weak link region the superconducting materials go over into thicker bulk superconducting electrodes of the same material (light blue). The axis origin lies at the top center of the normal metal strip.

4.1 Mathematical Model

We will consider the case of a Josephson junction consisting of layers of superconductors (S) and normal metals (N) as shown in Figure 4.1. In this junction two superconducting electrodes of lengths $(L-s)/2$ and thickness d_S are connected to each other by a small bridge of thickness d_N and length L made of a normal metal that suppresses the superconductivity of the electrodes and induces the Josephson effect.

For metals and superconductors satisfying the dirty limit condition, the properties of this junction at arbitrary temperature are described by the Usadel equations. In our model we consider only the S and N regions in Figure 4.1. The other materials enter the equations only through effective boundary conditions; The boundary Γ_{SN} denotes a boundary between the superconducting and normal materials, $\Gamma_{\pm}$ the boundaries where the superconductors go over into their bulk state. The remaining part of the boundary, here denoted by Γ_I is modeled as a boundary with a perfect insulator.

The behavior in the normal metal can be described by using the Usadel equations for superconducting materials with $\Delta = 0$. A complete description of this junction in the Φ-parametrization is thus given by

PDEs :

$$\omega_n \Phi_S G_S - \xi^2 \nabla \cdot \left[G_S^2 \nabla \Phi_S \right] = \omega_n \Delta G_S \qquad \text{in } S, \tag{4.1}$$

$$\omega_n \Phi_N G_N - \nabla \cdot \left[G_N^2 \nabla \Phi_N \right] = 0 \qquad \text{in } N, \tag{4.2}$$

Subject to:

$$\nabla \Phi \cdot \mathbf{n} = 0 \qquad \text{on } \Gamma_I, \tag{4.3}$$

$$\gamma_B G_N \nabla \Phi_N \cdot \mathbf{n} = G_S(\Phi_S - \Phi_N) \qquad \text{on } \Gamma_{SN}, \tag{4.4}$$

$$\gamma_B \xi G_S \nabla \Phi_S \cdot \mathbf{n} = \gamma G_N(\Phi_N - \Phi_S) \qquad \text{on } \Gamma_{SN}, \tag{4.5}$$

$$\Phi_S = \Delta_0 e^{\pm i\varphi/2} \qquad \text{on } \Gamma_{\pm}, \tag{4.6}$$

Here Φ_S, G_S and Φ_N, G_N denote the Green's functions in, respectively, the superconducting and normal material. All lengths are normalized with respect to the coherence length of the normal metal ξ_N and we use the dimensionless parameters

$$\xi = \frac{\xi_S}{\xi_N}, \qquad \gamma_B = \frac{R_B}{\rho_N \xi_N}, \qquad \gamma = \frac{\rho_S \xi_S}{\rho_N \xi_N}.$$

Δ_0 and φ are, respectively, the BCS energy gap and the phase of the bulk superconducting electrodes.

In a similar fashion the junction can be described in the θ, χ-parametrization by

PDE :

In S :

$$-\xi^2\nabla^2\theta_S + \xi^2 \sin\theta_S \cos\theta_S (\nabla\chi_S)^2 = iE\sin\theta_S + \frac{1}{2}\cos\theta_S\big(\Delta e^{-i\chi_S} + \Delta^* e^{i\chi_S}\big), \tag{4.7}$$

$$-\xi^2\nabla\cdot\Big[\sin^2\theta_S\nabla\chi_S\Big] = -\frac{i}{2}\sin\theta_S\big(\Delta e^{-i\chi_S} - \Delta^* e^{i\chi_S}\big), \tag{4.8}$$

In N :

$$-\nabla^2\theta_N + \sin\theta_N\cos\theta_N(\nabla\chi_N)^2 = iE\sin\theta_N, \tag{4.9}$$

$$-\nabla\cdot\Big[\sin^2\theta_N\nabla\chi_N\Big] = 0, \tag{4.10}$$

Subject to :

On $\Gamma_{\mathbf{I}}$:

$$\nabla\theta\cdot\mathbf{n} = 0, \tag{4.11}$$

$$\nabla\chi\cdot\mathbf{n} = 0, \tag{4.12}$$

On $\Gamma_{\mathbf{SN}}$:

$$\gamma_B\xi\sin^2\theta_S\nabla\chi_S\cdot\mathbf{n} = \gamma\sin\theta_N\sin\theta_S\sin(\chi_N-\chi_S), \tag{4.13}$$

$$\gamma_B\xi\nabla\theta_S\cdot\mathbf{n} = \gamma\big[\sin\theta_N\cos\theta_S\cos(\chi_N-\chi_S) - \cos\theta_N\sin\theta_S\big], \tag{4.14}$$

$$\gamma_B\sin^2\theta_N\nabla\chi_N\cdot\mathbf{n} = \sin\theta_S\sin\theta_N\sin(\chi_S-\chi_N), \tag{4.15}$$

$$\gamma_B\nabla\theta_N\cdot\mathbf{n} = \big[\sin\theta_S\cos\theta_N\cos(\chi_S-\chi_N) - \cos\theta_S\sin\theta_N\big], \tag{4.16}$$

On $\Gamma_{\pm}$:

$$\cos\theta_S = \frac{E}{\sqrt{E^2-\Delta_0^2}}, \tag{4.17}$$

$$\chi_S = \pm\frac{\varphi}{2}. \tag{4.18}$$

4.2 1D model

Before we consider the full SN-N-NS junction we first consider a special case in which the Usadel equations can be reduced to one-dimensional equations in the N layer. This simplifies the model and allows for certain analytical solutions. The results give a good starting point for the full 2D model.

4.2.1 Supercurrent

In Figure 4.1 the x-axis is taken to have its origin exactly at the center of the bridge, while $y = 0$ corresponds to the top of the normal metal layer.

For symmetric SN interfaces the symmetry of equations (4.1)-(4.2) and condition (4.6) allow us to consider only the right half ($0 \leq x \leq L/2$) of the junction with the additional boundary conditions

$$\frac{\partial}{\partial x}\,\mathrm{Re}(\Phi_N) = 0 \qquad \text{at } x = 0, \tag{4.19}$$

$$\mathrm{Im}(\Phi_N) = 0 \qquad \text{at } x = 0. \tag{4.20}$$

The analysis of the SN-N-NS junction was simplified in [5] in the case of small bridge thickness $d_N \ll 1$ and no inverse proximity effect $\gamma \approx 0$. The latter condition implies that the superconductivity in the S layers is not suppressed by the presence of the normal bridge. and the Green's function Φ_S is constant in the whole layer

$$\Phi_S = \Delta_0 e^{i\varphi/2}. \tag{4.21}$$

Now the Usadel equations need only be solved in the normal layer. When the normal layer thickness d_N is sufficiently small, we can assume the functions Φ_N and G_N to be independent of y in first approximation. Then by integration of equation (4.2) in the y-direction and application of boundary conditions (4.3) and (4.4) we obtain the following equations describing the one-dimensional SN-N-NS junction:

$$\frac{d}{dx}\left[G_N^2\frac{d\Phi_N}{dx}\right] = \omega_n\Phi_N G_N \qquad \text{for } 0 \le x \le s/2,$$
$$\frac{\gamma_{BM}}{G_N}\frac{d}{dx}\left(G_N^2\frac{d\Phi_N}{dx}\right) - \Big(G_S + \omega_n\gamma_{BM}\Big)\Phi_N = -G_S\Phi_S \qquad \text{for } s/2 \le x \le L/2,$$

Subject to :

$$\frac{d}{dx}\,\mathrm{Re}(\Phi_N) = 0 \qquad \text{at } x = 0,$$
$$\mathrm{Im}(\Phi_N) = 0 \qquad \text{at } x = 0,$$
$$\frac{d}{dx}\Phi_N = 0 \qquad \text{at } x = L/2,$$
$$\Phi_S = \Delta_0 e^{i\varphi/2}.$$

Here $\gamma_{BM} = \gamma_B d_N$. In general these equations cannot be solved analytically, however, in [5] two limiting cases were found where an analytical solution is possible.

Case 1: $\qquad \sqrt{\gamma_{BM}} \ll s \ll 1$

In this case the SN boundaries are very transparent and the suppression of the superconductivity coming from the S electrode by the proximity effect in the N layers is negligible. In the region $s/2 \le x \le L/2$, Φ_N will differ only slightly from Φ_S. In this limit the solution is given by

$$\Phi_N = \delta\cos\frac{\varphi}{2} + i\sqrt{\omega_n^2 + \delta\cos^2\frac{\varphi}{2}}\,\tan\left(\frac{2}{s}\,\mathrm{atan}\left[\frac{\Delta_0\sin\frac{\varphi}{2}}{\Omega_1}x\right]\right), \tag{4.22}$$

with

$$\Omega_1 = \sqrt{\Omega^2 + \Delta_0^2\cos^2\frac{\varphi}{2}},\ \Omega = \omega_n\Big(1 + \gamma_{BM}\sqrt{\omega_n^2 + \Delta_0^2}\Big),\ \delta = \frac{G_S\Delta_0}{G_S + \gamma_{BM}\omega_n}.$$

The supercurrent through the junction in this limit is given by

$$\frac{eI_sR_N}{2\pi T_c} = t\sum_{n=0}^{\infty}\frac{\Delta_0\cos\frac{\varphi}{2}}{\Omega_1}\,\mathrm{atan}\left(\frac{\Delta_0\sin\frac{\varphi}{2}}{\Omega_1}\right), \tag{4.23}$$

In the limit of $\gamma_{BM} \to 0$ this result reduces to the KO1 result derived by Kulik and Omelyanchuk [43] for superconducting bridges.

Case 2: $s \ll \frac{\gamma_{BM}}{1+\gamma_{BM}}$

In this case γ_{BM} is very large and the SN boundary is very opaque. In this limit the solution is given by

$$\Phi_N = \delta \cos\frac{\varphi}{2} + i\sqrt{\omega_n^2 + \delta\cos^2\frac{\varphi}{2}}\tan\left(\frac{\sqrt{2}\Delta_0 \sin\frac{\varphi}{2}}{\sqrt{\gamma_{BM}}\sqrt{\sqrt{\omega_n^2+\Delta_0^2}(\sqrt{\Omega^2+\Delta_0^2}+\Omega_1)}}\right). \tag{4.24}$$

The supercurrent through the junction is then given by

$$\frac{eI_sR_N}{2\pi T_c} = t\sum_{n=0}^{\infty}\frac{\sqrt{2}\Delta_0^2\sin\varphi}{\Omega_1\sqrt{(\sqrt{\Omega^2+\Delta_0^2}+\Omega_1)\sqrt{\omega_n^2+\Delta_0^2}}}. \tag{4.25}$$

In between these limits the supercurrent has to be calculated numerically. Figure 4.2 shows the critical current calculated numerically for a short SN-N-NS junction satisfying the geometrical constraints for equations (4.23) and (4.25) to be valid. From this figure it can be seen that by varying the interface parameter γ_{BM} the critical current interpolates perfectly between these two analytical expressions. At every temperature the critical current reaches its maximal value at $\gamma_{BM} = 0$, when the SN boundary is fully transparent. For more opaque boundaries the critical current decays to zero as $1/\gamma_{BM}$.

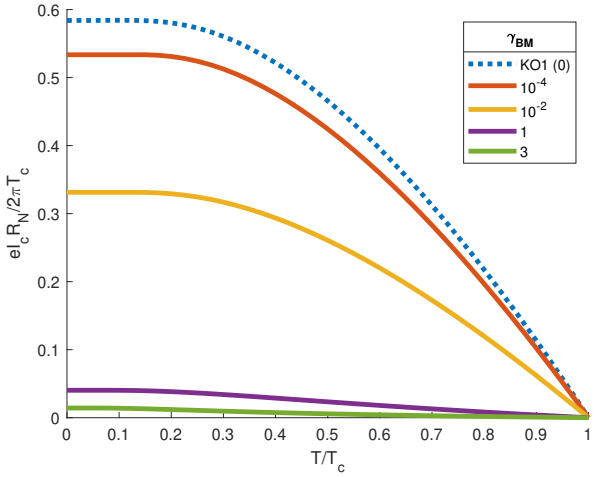

Figure 4.2: Critical current of a 1D SN-N-NS Josephson junction with dimensions $s = 0.3$, $L = 5$ calculated numerically for different interface parameters and temperatures. The dashed line indicates the analytical result by Kulik and Omelyanchuk [43].

For larger junction sizes these analytical solutions are not valid, but the shape of the critical current curves stays roughly the same as shown in Figure 4.3.

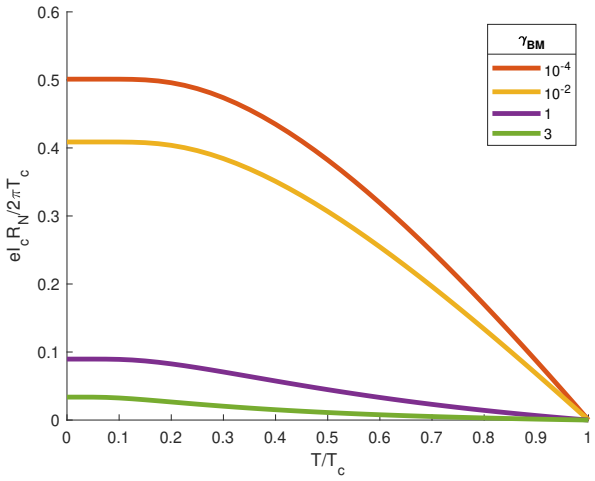

Figure 4.3: Critical current of a 1D SN-N-NS Josephson junction with dimensions $s = 1$, $L = 5$ calculated with a FEM model for different interface parameters and temperatures.

The effect of the junction length s on the I_cR_N product is twofold. Firstly it decreases the critical current density J_c because of spreading throughout the junction, but at the same time it increases the junction resistance R_N. For transparent junctions this leads to a net decrease of the I_cR_N product, while for more opaque boundaries it leads to a net increase.

4.2.2 Density of states

Next, we investigate the density of states inside the SN-N-NS junction. To calculate the density of states of this junction we need to consider real values of the energy E. For this purpose we need to consider the Usadel equations in the θ, χ-parametrization (4.7)-(4.18). By applying the same approximations ($d_N \ll 1,\ \gamma \approx 0$) to these equations as in the above section the SN-N-NS junction can be described by the following one-dimensional equations

$\mathbf{0 \leq x \leq s/2}$:

$$-\frac{d^2\theta_N}{dx^2} + \sin\theta_N \cos\theta_N \left(\frac{d\chi_N}{dx}\right)^2 = iE \sin\theta_N, \tag{4.26}$$

$$-\frac{d}{dx}\left[\sin^2\theta_N \frac{d\chi_N}{dx}\right] = 0, \tag{4.27}$$

$\mathbf{s/2 \leq x \leq L/2}$:

$$-\gamma_{BM}\frac{d^2\theta_N}{dx^2} + \gamma_{BM}\sin\theta_N \cos\theta_N \left(\frac{d\chi_N}{dx}\right)^2 = \gamma_{BM} iE \sin\theta_N + \cos\theta_N \sin\theta_S \cos(\chi_S - \chi_N) - \sin\theta_N \cos\theta_S, \tag{4.28}$$

$$-\gamma_{BM}\frac{d}{dx}\left[\sin\theta_N^2 \frac{d\chi_N}{dx}\right] = \sin\theta_S \sin\theta_N \sin(\chi_S - \chi_N), \tag{4.29}$$

Subject to:

$$\frac{d\theta_N}{dx} = 0, \quad \chi_N = 0 \qquad \text{at } x = 0, \tag{4.30}$$

$$\frac{d\theta_N}{dx} = 0, \quad \frac{d\chi_N}{dx} = 0 \qquad \text{at } x = \frac{L}{2}, \tag{4.31}$$

$$\cos\theta_S = \frac{E}{\sqrt{E^2 - \Delta_0^2}}, \quad \chi_S = \varphi/2. \tag{4.32}$$

Before we go to the numerical solution of these equations we first consider a few cases analytically.

The normal solution

Equations (4.26)-(4.31) allow the simple constant solution

$$\theta_N = k\pi,$$
$$\chi_N = \begin{cases} 0 & \text{for } 0 \leq x \leq s/2, \\ \chi_S + \frac{\pi}{2} + l\pi & \text{for } s/2 \leq x \leq L/2. \end{cases}$$

In fact the solution of χ_N in the region $0 \leq x \leq s/2$ is arbitrary as long as it satisfies $\chi_N(0) = 0$. The physical meaning of this solution becomes clear when we look at the local density of states $N(E, \mathbf{r}) = \cos(\theta_N) = (-1)^k$. For odd k this solution produces a negative density of states, which is non-physical. This is a consequence of the parametrization, which results in an infinite number of solutions. In general k must always be chosen zero, or in other words θ_N must be restricted to the interval $-\pi \leq \theta_N < \pi$ for a

physical solution. This solution describes the normal material in its normal non-superconducting state. Luckily there are more exotic solutions.

Case 1:	$\sqrt{\gamma_{BM}} \ll s \ll 1, \qquad \varphi = 0$

It is clear that for $\varphi = 0$, χ_N has the simple solution $\chi_N = 0$, which satisfies all boundary conditions. In this case equations (4.26) and (4.28) reduce to

$$-\frac{d^2\theta_N}{dx^2} = iE\sin\theta_N \qquad \text{for } 0 \le x \le s/2, \tag{4.33}$$

$$-\gamma_{BM}\frac{d^2\theta_N}{dx^2} - \gamma_{BM} iE\sin\theta_N = \sin(\theta_S - \theta_N) \text{ for } s/2 \le x \le L/2. \tag{4.34}$$

Now we consider the equations for θ_N in both regions separately.

$\mathbf{0 \le x \le s/2}$: The second derivative term in equation (4.33) scales as $\frac{\theta_N}{s^2}$, while the second term scales as θ_N. In the case $s \ll 1$ we can thus neglect the second term and approximate the equation as

$$-\frac{d^2\theta_N}{dx^2} = 0. \tag{4.35}$$

Together with boundary condition (4.30) this yields the solution $\theta_N = C$ for some constant C.

$\mathbf{s/2 \le x \le L/2}$: For $\gamma_{BM} = 0$ equation (4.34) yields the solution $\theta_N = \theta_S$. Thus for small values of γ_{BM} we can try the ansatz $\theta_N = \theta_S + \delta_\theta$. Inserting this into equation (4.34) gives

$$-\gamma_{BM}\frac{d^2\delta_\theta}{dx^2} - \gamma_{BM} iE\sin(\theta_S + \delta_\theta) = -\sin(\delta_\theta). \tag{4.36}$$

Now since θ_N is close to θ_S we can linearize this equation

$$\gamma_{BM}\frac{d^2\delta_\theta}{dx^2} + \gamma_{BM} iE\sin\theta_S + \gamma_{BM} iE\cos\theta_S\delta_\theta = \delta_\theta. \tag{4.37}$$

The general solution of this equation is given by

$$\delta_\theta = \frac{iE\sin\theta_S}{z} + Ae^{\sqrt{z}x} + Be^{-\sqrt{z}x}, \tag{4.38}$$

with

$$z = \frac{1}{\gamma_{BM}} - iE\cos\theta_S = \frac{1}{\gamma_{BM}} - \frac{E^2}{\sqrt{\Delta_0^2 - E^2}}. \tag{4.39}$$

The constants A and B can be found by enforcing the continuity of θ_N at $x = s/2$ and boundary condition (4.31). Together these give

$$A = Be^{-\sqrt{z}L}, \tag{4.40}$$

$$B = \frac{C - \theta_S - iE\sin\theta_S/z}{e^{\sqrt{z}(\frac{s}{2}-L)} + e^{-\sqrt{z}\frac{s}{2}}}. \tag{4.41}$$

To determine the constant C we note that at $x = s/2$ the solution θ_N must satisfy both equations (4.26) and (4.28). The constant C must thus satisfy

$$-\gamma_{BM} iE \sin C = \sin(\theta_S - C), \tag{4.42}$$

which can be solved to give

$$C = \arccos\left(\frac{\cos(\theta_S) - \gamma_{BM} iE}{\sqrt{1 - 2\gamma_{BM} iE\cos(\theta_S) - \gamma_{BM}^2 E^2}}\right). \tag{4.43}$$

In first approximation the density of states in this limit is then given by

$$N(E,x) = \begin{cases} \mathrm{Re}\left\{ \frac{-iE\left(1+\gamma_{BM}\sqrt{\Delta_0^2 - E^2}\right)}{\left[\Delta_0^2 - E^2\left(1+\gamma_{BM}\sqrt{\Delta_0^2-E^2}\right)^2\right]^{1/2}} \right\} & \text{for } 0 \le x \le s/2, \\ \mathrm{Re}\left\{ \cos\left(\theta_S + \frac{\gamma_{BM} iE\sin\theta_S}{1-\gamma_{BM} iE\cos\theta_S} \right.\right. & \\ \qquad \left.\left. + Ae^{\sqrt{z}x} + Be^{-\sqrt{z}x}\right)\right\} & \text{for } s/2 \le x \le L/2. \end{cases} \tag{4.44}$$

The DOS obtains its minimal value in the center of the junction $0 \le x \le s/2$, and then increases exponentially over the barrier towards a constant value in the L-region under the superconductor. As $\gamma_{BM} \to 0$ the solution will converge to $\theta_N = \theta_S$ and the density of states reduces to the BCS result.

Case 2: $\qquad s \ll 1 \ll \sqrt{\gamma_{BM}}, \qquad \varphi = 0$

$\mathbf{0 \le x \le s/2}$: In this region equation (4.33) has the solution $\theta_N = C$, with C given by equation (4.43).

$\mathbf{s/2 \le x \le L/2}$: In the limit $\gamma_{BM} \to \infty$ equation (4.34) has the constant solution $\theta_N = 0$. For large, but finite values of γ_{BM} it is reasonable to try the ansatz $\theta_N = \delta_\theta$. Inserting this into equation (4.34) gives

$$-\gamma_{BM}\frac{d^2\delta_\theta}{dx^2} - \gamma_{BM} iE\sin(\delta_\theta) = \sin(\theta_S - \delta_\theta). \tag{4.45}$$

Linearizing this equation then gives

$$\gamma_{BM}\frac{d^2\delta_\theta}{dx^2} + \gamma_{BM} iE\delta_\theta = -\sin\theta_S + \delta_\theta \cos\theta_S. \tag{4.46}$$

This equation has the general solution

$$\delta_\theta = \frac{\sin\theta_S}{\cos\theta_S - \gamma_{BM} iE} + Ae^{\sqrt{z}x} + Be^{-\sqrt{z}x}, \tag{4.47}$$

with

$$z = \frac{1}{\gamma_{BM}}\cos\theta_S - iE. \tag{4.48}$$

By enforcing the boundary conditions and continuity of the solution the constants A and B can be determined as

$$A = Be^{-\sqrt{z}L}, \tag{4.49}$$

$$B = \frac{C - \frac{\sin\theta_S}{\gamma_{BM} z}}{e^{\sqrt{z}(\frac{s}{2}-L)} + e^{-\sqrt{z}\frac{s}{2}}}. \tag{4.50}$$

The density of states in this limit is then given by

$$N(E,x) = \begin{cases} \mathrm{Re}\left\{ \frac{-iE\left(1+\gamma_{BM}\sqrt{\Delta_0^2-E^2}\right)}{\left[\Delta_0^2-E^2\left(1+\gamma_{BM}\sqrt{\Delta_0^2-E^2}\right)^2\right]^{1/2}} \right\} & \text{for } 0 \le x \le s/2, \\ \mathrm{Re}\left\{ \cos\left(\frac{\sin\theta_S}{\cos\theta_S - \gamma_{BM} iE} \right.\right. & \\ \qquad \left.\left. + Ae^{\sqrt{z}x} + Be^{-\sqrt{z}x} \right) \right\} & \text{for } s/2 \le x \le L/2. \end{cases} \tag{4.51}$$

In the region $0 \le x \le s/2$ the density of states is given by the same expression for both small and large values of γ_{BM}. This density of states has two singularities. One at $E = \Delta_0$, which denotes the superconducting energy gap and another one at $E/\Delta_0 = z_0$, with

$$z_0 = -\frac{1}{3} + \frac{(\beta^2-3)^{\frac{1}{2}}}{3\beta}\Big([1 + (A^2-1)^{\frac{1}{2}}]^{\frac{1}{3}} + [1 - (A^2-1)^{\frac{1}{2}}]^{\frac{1}{3}} \Big), \tag{4.52}$$

$$A = \beta(18-\beta^2)/(\beta^2-3)^{\frac{3}{2}}, \tag{4.53}$$

$$\beta = \gamma_{BM}\Delta_0. \tag{4.54}$$

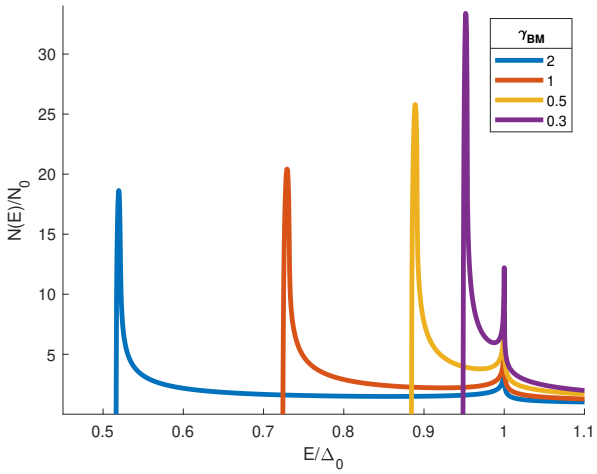

Figure 4.4: Density of states in a 1D SN-N-NS junction with dimensions $s = 0.02, L = 20$ and $\varphi = 0$, $t = 0.5$ calculated with a FEM model at $x = 0$ for different values of γ_{BM}.

To verify these analytical results we calculated the density of states in the center of the junction numerically for different values of γ_{BM} as shown in Figure 4.4. At $\gamma_{BM} \gtrsim 0.1$ the peak in the DOS splits into two separate peaks with the separation increasing for larger γ_{BM}. One peak remains at the superconducting energy gap Δ, while the other shifts to lower energies.

Below this second peak the density of states vanishes, therefore this point is called the *subgap*. The numerical results are in good agreement with equations (4.44) and (4.51). In this setting, for zero phase difference, our model reduces to that of a SN-bilayer and the results agree with earlier results in literature [44, 45].

Case 3:	$\gamma_{BM} = 0, \qquad s \ll 1$

In the presence of a nonzero phase difference, χ_N will not be zero anymore. Instead both χ_N and θ_N will be a function of φ. In the case $\gamma_{BM} = 0$ the solution of equations (4.28) and (4.29) in the region under the superconducting electrodes takes on the simple form $\theta_N = \theta_S$, $\chi_N = \chi_S$.

In the limit of $s \ll 1$ the last term in equation (4.26) can be neglected and an analytical solution is possible [46]:

$$\theta_N = \operatorname{acos}\left(\frac{\sqrt{\alpha^2+1}}{\alpha}\cos[j_E\alpha(x-\chi_0)]\right), \tag{4.55}$$

$$\chi_N = \chi_0 - \operatorname{atan}\left(i\alpha\tan[j_E\alpha(x-\chi_0)]\right). \tag{4.56}$$

The constants α, χ_0 and j_E are determined from the boundary conditions and by enforcing continuity at $x = s/2$. In this limit they are

$$\chi_0 = 0, \tag{4.57}$$

$$\alpha = \frac{\sqrt{E^2 - \Delta_0^2 \cos^2(\varphi/2)}}{\Delta_0 \cos(\varphi/2)}, \tag{4.58}$$

$$j_E = \frac{2\Delta_0 \cos(\varphi/2)}{s\sqrt{E^2 - \Delta_0^2 \cos^2(\varphi/2)}} \operatorname{acos}\left(\sqrt{\frac{E^2 - \Delta_0^2 \cos^2(\varphi/2)}{E^2 - \Delta_0^2}}\right). \tag{4.59}$$

The density of states in this limit is then given by

$$N(E,x) = \begin{cases} \operatorname{Re}\left\{\frac{\sqrt{\alpha^2+1}}{\alpha} \cos[j_E \alpha x]\right\} & \text{for } 0 \le x \le s/2, \\ \operatorname{Re}\left[\cos\theta_S\right] & \text{for } s/2 \le x \le L/2. \end{cases} \tag{4.60}$$

Now it becomes clear what the effect of the phase difference is on the density of states. At $x = \frac{s}{2}$ the density of states reduces to the BCS value

$$N(E, s/2) = \operatorname{Re}\left[\cos\theta_S\right] = \operatorname{Re}\left[\frac{E}{\sqrt{E^2 - \Delta_0^2}}\right],$$

while at the center of the bridge at $x = 0$ the density of states becomes

$$N(E, 0) = \operatorname{Re}\left[\frac{E}{\sqrt{E^2 - \Delta_0^2 \cos^2(\varphi/2)}}\right].$$

The presence of a phase difference thus leaves the energy gap at $s/2$ intact, but reduces the energy gap in the center of the junction by a factor of $\cos(\varphi/2)$, as seen in Figure 4.5. For zero phase difference the energy gap reduces to the BCS gap, while at a phase difference of π the energy gap closes completely.

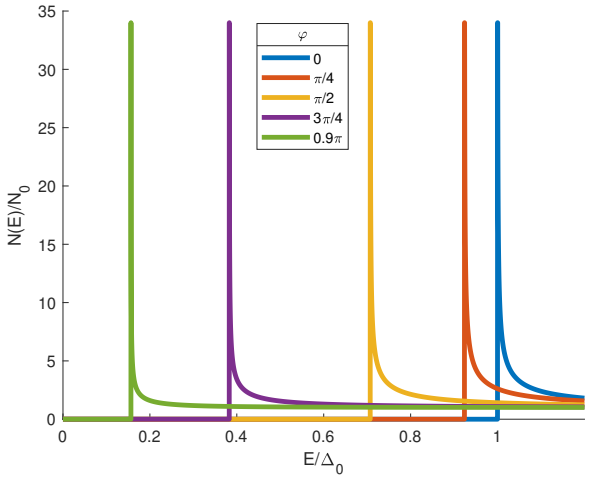

Figure 4.5: Density of states of a 1D SN-N-NS Josephson junction with dimensions $s = 0.1, L = 5$ and $\gamma_{BM} = 10^{-4}$, $t = 0.5$ calculated with a FEM model at $x = 0$ for different values of φ.

General case:	$s \ll 1$

For arbitrary values of γ_{BM} and φ both of the above described effects take place. In the short junction limit $s \ll 1$ an analytical solution in the region $0 \leq x \leq s/2$ can be found by using the general solution in (4.56) and applying the boundary conditions and continuity conditions at $x = s/2$. The general analytical solution is then given by

$$\theta_N = \operatorname{acos}\left(\frac{\sqrt{\alpha^2+1}}{\alpha}\cos[j_E\alpha(x-\chi_0)]\right), \tag{4.61}$$

$$\chi_N = \chi_0 - \operatorname{atan}\left(i\alpha\tan[j_E\alpha(x-\chi_0)]\right), \tag{4.62}$$

with the constants

$$\chi_0 = 0, \tag{4.63}$$

$$\alpha = \frac{\sqrt{\tilde{E}^2 - \Delta_0^2\cos^2(\varphi/2)}}{\Delta_0\cos(\varphi/2)}, \tag{4.64}$$

$$j_E = \frac{2\Delta_0\cos(\varphi/2)}{s\sqrt{\tilde{E}^2 - \Delta_0^2\cos^2(\varphi/2)}}\operatorname{acos}\left(\sqrt{\frac{\tilde{E}^2 - \Delta_0^2\cos^2(\varphi/2)}{\tilde{E}^2 - \Delta_0^2}}\right), \tag{4.65}$$

$$\tilde{E} = E\left(1 + \gamma_{BM}\sqrt{\Delta_0^2 - E^2}\right). \tag{4.66}$$

This solution reduces to the results found previously in the limits $\varphi = 0$ and $\gamma_{BM} = 0$, respectively. The density of states at $s/2$ still satisfies equation (4.51), but at the center of the junction $x = 0$ it is now given by

$$N(E, 0) = \mathrm{Re}\left[\frac{\tilde{E}}{\sqrt{\tilde{E}^2 - \tilde{\Delta}_0^2}}\right], \tag{4.67}$$

with $\tilde{\Delta}_0 = \Delta_0 \cos(\varphi/2)$. An exact expression for the poles of the DOS is too long to write down on this page, but it is worth noting that the singularity at $E = \Delta_0$ that existed in the density of states at $\varphi = 0$ reduces to a local maximum at nonzero phase differences.

Numerical results in this limit are shown in Figures 4.6 and 4.7 and are in good agreement with this analytical solution. It can be seen that the density of states at the junction center still contains one singularity that depends on both γ_{BM} and φ and lies at energies lower than those given in (4.52). As $\varphi \to \pi$ the singularity shifts to zero energy and the energy gap closes.

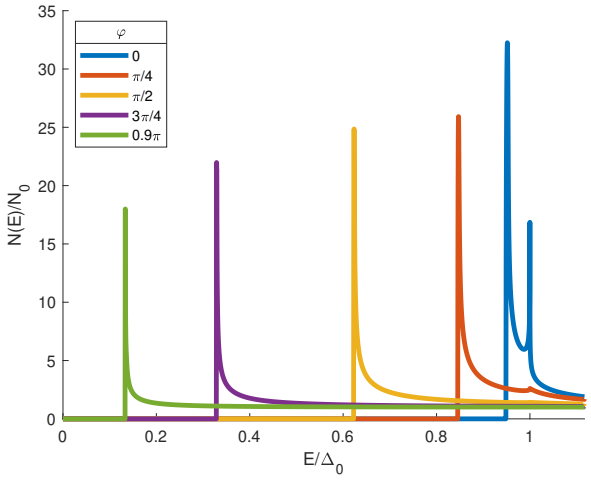

Figure 4.6: Density of states in a 1D SN-N-NS junction with dimensions $s = 0.1, L = 5$ and $\gamma_{BM} = 0.3, t = 0.5$ calculated with a FEM model at $x = 0$ for different values of φ.

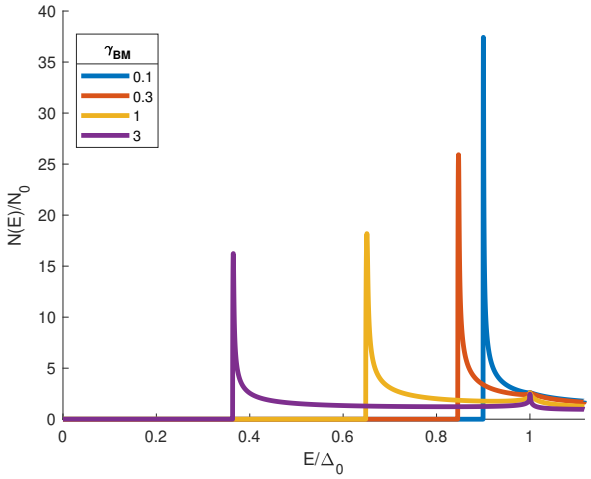

Figure 4.7: Density of states in a 1D SN-N-NS junction with dimensions $s = 0.1, L = 5$ and $\varphi = \pi/4, t = 0.5$ calculated with a FEM model at $x = 0$ for different values of γ_{BM}.

Influence of bridge length

So far, all our results were derived in the limit $s \ll 1$. In this limit the density of states contains up to two singularities of which the first one indicates the edge of the subgap. For lager values of the bridge length the density of states has to be calculated numerically. Increasing the bridge length distorts the DOS as seen in Figure 4.8. It can be seen that the peak present at $E = \Delta_0$ remains at larger bridge lengths, but that the singularity at a lower energy is smeared out, leading to a decrease of the magnitude of the energy gap. Furthermore, a new peak appears in between the two old singularities. As s increases the energy gap becomes smaller, eventually vanishing as $s \to \infty$. For larger s the spacing between the electrodes increases and fewer Cooper pairs can penetrate up to the center of the normal metal, leading to a reduction of the energy gap.

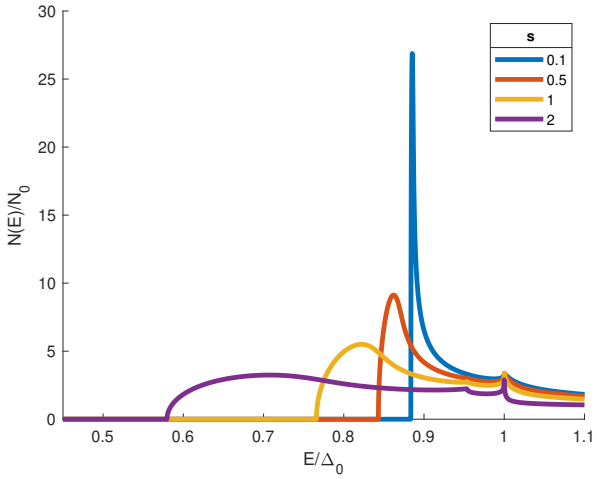

Figure 4.8: Density of states in a 1D SN-N-NS junction with dimension $L = 20$ and $\varphi = 0.6, \gamma_{BM} = 0.3, t = 0.5$, calculated with a FEM model at $x = 0$ for different bridge lengths s.

4.3 2D model

4.3.1 Supercurrent

All the results obtained using the one-dimensional model were derived under the following assumptions:

- The inverse proximity effect can be neglected ($\gamma = 0$) so inside the S electrodes the Green's functions take on their bulk value, not being influenced by the proximity of the N layer.
- The normal layer thickness d_N is small enough so that the Green's functions Φ_n are independent of y in the first approximation on d_N.

To generalize the one-dimensional results the full equations (4.1)-(4.6) need to be solved. To solve these equations a finite element method is implemented making use of first order Lagrangian basis functions. Since the analytical solution is discontinuous at the SN interface by virtue of equations (4.4) and (4.5), the solution over these interfaces can not be approximated by continuous basis functions. Instead, it must be calculated in each layer individually and be matched by making use of these boundary conditions.

In two dimensions the Usadel equations need to be solved self-consistently. In addition to equations (4.1)-(4.6) one also has to solve the self-consistency

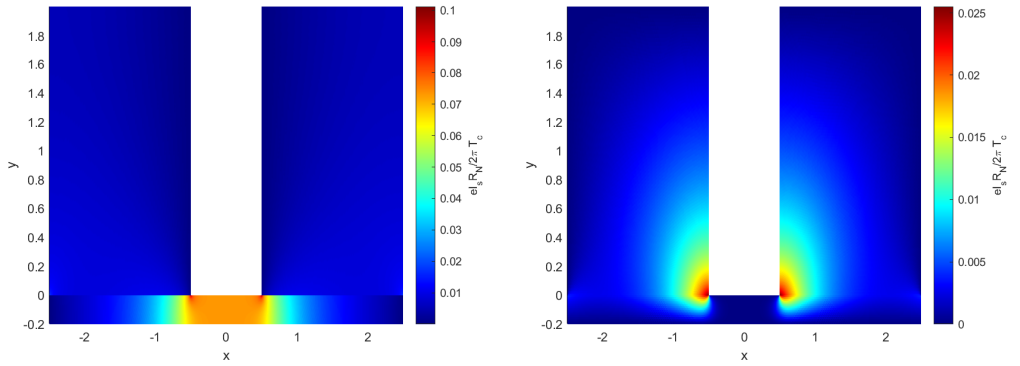

(a) (b)

Figure 4.9: Spatial distribution of the normalized current density in the SN-N-NS junction. (a) depicts the x-component of the current density, (b) depicts the y-component of the current density. Parameters used were $\xi = 1$, $\gamma_B = 1.5$, $\gamma = 1$, $t = 0.5$, $\varphi = \pi/2$, $s = 1, L = 5, d_S = 2, d_N = 0.2$.

equation

$$\Delta \ln(t) + t \sum_{n=-\infty}^{\infty} \left[\frac{\Delta}{\omega_n} - \frac{\Phi(\omega_n, \mathbf{r})}{\sqrt{\omega_n^2 + |\Phi|^2}} \right] = 0. \tag{4.68}$$

This equation has to be solved iteratively and requires the solution of the Usadel equation at all Matsubara frequencies during each iteration. The procedure used for solving the self-consistency equation can be found in Appendix A.1.

In the full 2D case the current density can be calculated inside the complete junction as shown in Figures 4.9a and 4.9b. It can be seen that the current density is symmetric and varies strongly throughout the junction. It is the highest inside the weak link region at the center of the normal metal. It peaks at the edges of the weak link region due to the sharp angle between the ends of the superconductors and the normal metal strip. Inside the superconductors the current density is much smaller than the density inside the normal metal layer, even at high values of γ. By virtue of (2.52) the y-component of the current density is continuous over the SN-interface, ensuring continuity of the current component perpendicular to the interface.

The influence of the normal layer thickness d_N and the proximity effect parameter γ on the critical current is illustrated in Figures 4.10a and 4.10b. It can be seen that the current density decreases monotonically, both as a function of d_N and of γ at every temperature. The influence of d_N is

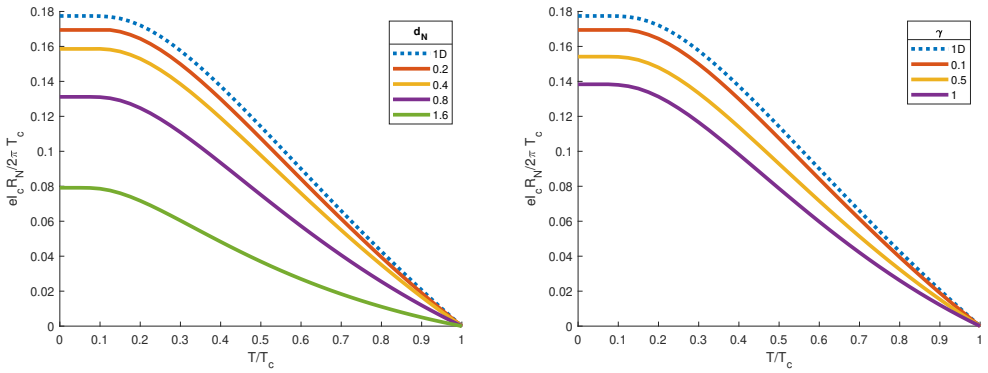

(a) (b)

Figure 4.10: Normalized critical current in the SN-N-NS junction dependence on temperature for various values of (a) the normal layer thickness d_N for $\gamma = 0.1$ (b) the proximity effect parameter γ for $d_N = 0.2$. Dashed lines indicate results obtained numerically using the one-dimensional model of [5]. Other parameters used were $\xi = 1, \gamma_{BM} = 0.3, s = 1, L = 5, d_S = 5$.

stronger than that of γ. Figures 4.11a and 4.11b show the dependence of the current density on d_N and γ. The current density decreases approximately exponentially, both with d_N and γ. In the limit $d_N \to 0, \gamma \to 0$ the one-dimensional results in [5] are recovered.

4.3.2 Density of states

The influence of the normal metal thickness and the proximity effect on the density of states in the junction can be investigated by using a 2D model. For a full 2D calculation the energy gap Δ needs to be known inside the two superconducting layers. This can be calculated self-consistently in the Φ-parametrization by solving equations (4.1)-(4.6) and (4.68). Using the resulting value we proceed to solve equations (4.7)-(4.18). Using this method the DOS can be calculated not only in the normal metal, but also in the superconductors. An example of the distribution of the DOS inside the junction is shown in Figure 4.12.

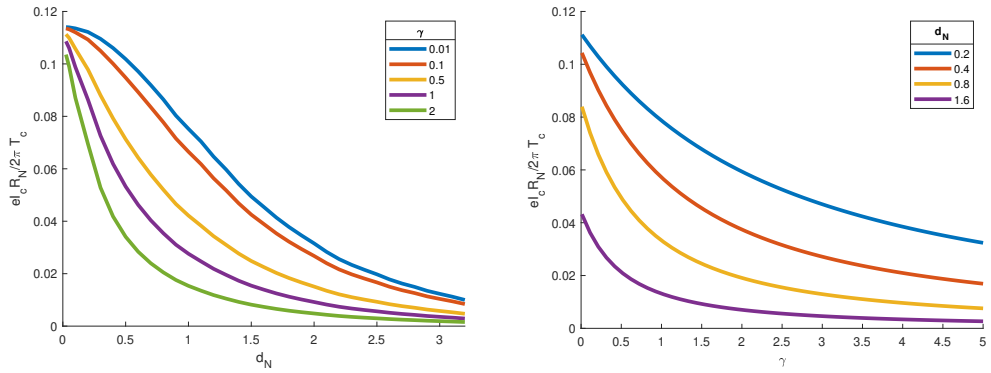

(a) (b)

Figure 4.11: Normalized critical current in the SN-N-NS junction dependence on (a) the normal layer thickness d_N for various values of γ (b) the proximity effect parameter γ for various values of d_N. Other parameters used were $\xi = 1, \gamma_{BM} = 0.3, t = 0.5, s = 1, L = 5$ and $d_S = 5$.

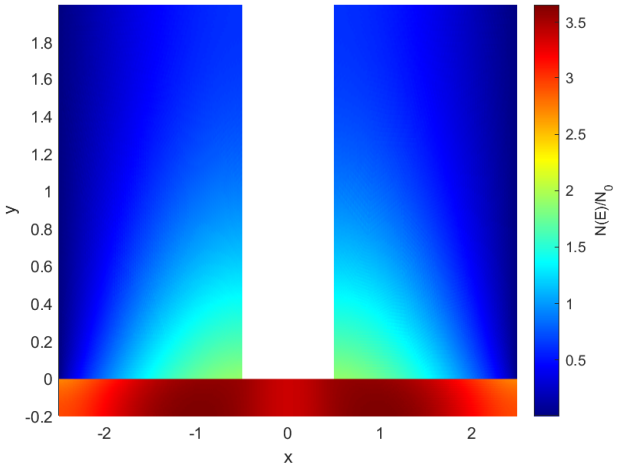

Figure 4.12: Normalized density of states distribution in the SN-N-NS junction at $E = 0.9\Delta_0, \gamma_B = 1.5$, $\gamma = 1$, $\varphi = 0$ and $t = 0.5$.

Using this two-dimensional model we can investigate the effect of d_N and γ on the density of states at the center of the normal metal. These effects are illustrated in Figures 4.13a and 4.13b. It can be seen that both increasing d_N and increasing γ results in a decrease of the subgap. An increase in the normal layer thickness further separates the superconductors and the center of the normal metal, causing fewer Cooper pairs to penetrate towards this

point, which leads to a reduction of the subgap. Increasing γ suppresses the number of Cooper pairs in the superconductors, which means that fewer pairs can penetrate into the normal metal, thus reducing the subgap. The

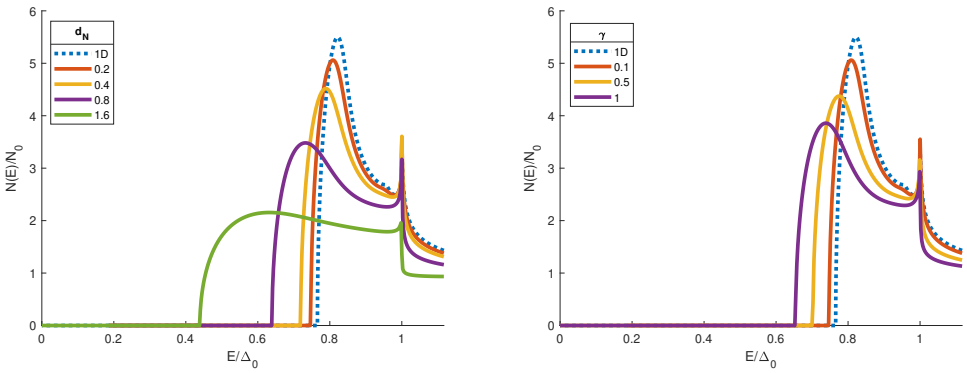

(a) (b)

Figure 4.13: Normalized density of states at the center of a 2D SN-N-NS junction dependence on energy at (a) various values of d_N for $\gamma = 0.1$ (b) various values of γ for $d_N = 0.2$. Other parameters used were $\xi = 1, \gamma_{BM} = 0.3, t = 0.5, s = 1, L = 5$ and $d_S = 5$. The dashed line indicates the density of states calculated using a 1D model with the same parameters.

dependence of the density of states on the phase difference and energy at the center of the normal metal is shown in Figure 4.14. For small phase differences the two peaks in the density of states at $E = \Delta_0$ and $E \approx z_0$ are clearly visible. Both peaks become increasingly more narrow as the phase difference increases and vanish at a phase difference $\varphi = \pi$. The magnitude of the subgap depends on the phase difference as well, having its maximum at zero phase difference and closing completely at $\varphi = \pi$. Even though $\gamma = 1$ and the short junction limit conditions are not satisfied, the shape of the energy gap still resembles the limiting behavior of $\cos(\varphi/2)$ found in the one-dimensional model.

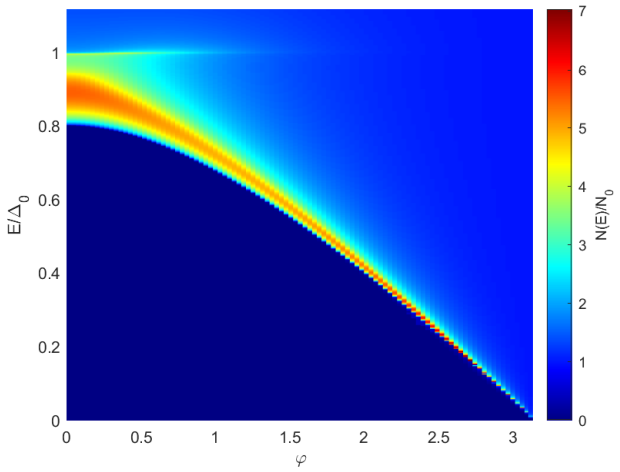

Figure 4.14: Normalized density of states at the center of the normal metal strip in the SN-N-NS junction as a function of energy E and phase difference φ. Other parameters are $\gamma_B = 1.5$, $\gamma = 0.01$, and $t = 0.5, \xi = 1, s = 1, L = 3, d_S = 5, d_N = 0.2$.

4.4 Current Injection

In the previous sections, the superconducting phase was fixed at the left and right boundaries of the superconducting electrodes, where these go over into thicker electrodes. These boundaries were positioned right above the boundaries of the normal metal as shown in Figure 4.1. The normal metal influences, however, the superconductor through the proximity effect and might thus cause a nonuniform phase over this boundary. These boundary conditions are thus only valid whenever the superconductors go over into much thicker electrodes, which are unperturbed by the presence of the normal metal. This situation can be realized when the junction encloses a SQUID ring.

Another interesting situation to analyze is the case when a homogeneous unidirectional supercurrent is sent through the junction. Such a supercurrent in the x-direction can be sustained by a Green's function in the form

$$\Phi = \Delta_0 e^{ikx}. \tag{4.69}$$

This solution corresponds to a homogeneous supercurrent

$$\frac{eR_N I_s}{2\pi T_c} = tlk \sum_{n=0}^{\infty} \left[\frac{\Delta_0^2}{\omega_n^2 + \Delta_0^2} \right]. \tag{4.70}$$

From this expression, it becomes clear that the linear phase gradient k is related to the magnitude of the supercurrent. In real junctions, equation (4.69) is not a valid solution, because due to a process called *depairing*, a large phase gradient will also suppress the supercurrent. This can best be seen in the θ, χ-parametrization using equations (4.7) and (4.8). A large phase gradient $\nabla\chi$ will lead to a suppression of θ, thereby decreasing the energy gap and the current density. The current density will thus attain its maximum value at a finite phase gradient. This maximum value of the current density is called the *depairing current density*.

To model the SN-N-NS junction with these current-injection boundary conditions and determine the depairing current density we consider the geometry shown in Figure 4.15 where the superconducting electrodes now extend a length $(L_2 - L)/2$ beyond the normal metal to ensure that the homogeneous in- and out-flowing current are not disturbed by the presence of the normal metal.

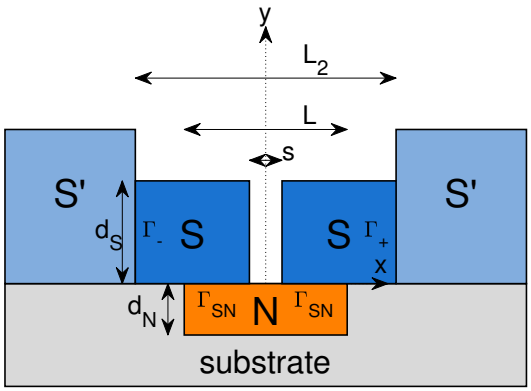

Figure 4.15: Sketch of the SN-N-NS junction. The superconducting material (dark blue) and normal metal (orange) are deposited on a dielectric substrate (grey). Far away from the weak link region, the superconducting materials go over into thicker bulk superconductive electrodes of the same material (light blue). The axis origin lies at the top center of the normal metal strip.

The implementation of the current inflow boundary condition (4.69) in the finite element discretization cannot be done directly since this expression sets different conditions on the absolute value of the Green's function and on its phase gradient, while only the total Green's function Φ can be varied. One way to work around this is to use the two-parameter θ, χ-parametrization and

implement the current-injection boundary condition as

$$\theta = \operatorname{atan}\left(\frac{\Delta_0}{\omega_n}\right) \qquad \text{at } \Gamma_{\pm}, \tag{4.71}$$

$$\nabla\chi \cdot \mathbf{n} = k \qquad \text{at } \Gamma_{\pm}. \tag{4.72}$$

The main problem with this approach is that the self-consistency equation (2.24) cannot always be solved to the required accuracy. It converges to different values depending on the initial guesses chosen for χ. The reason for this behavior is that all boundary conditions on χ are now Neumann type boundary conditions, which causes problems determining the value of χ in the junction.

If $(L_2 - L)/2$ is chosen large enough the ends of the superconductors feel little suppression from the normal metal and the current injection can also be modeled by the regular boundary condition (4.6). This boundary condition enforces zero current in the direction parallel to the boundary, but for large L_2 the current perpendicular to the interface becomes homogeneous as well and the Green's functions gain a constant phase gradient perpendicular to the boundary.

It is interesting to determine how the junction behaves under these current-injection boundary conditions. An interesting quantity to determine is the current-phase relationship shown in Figures 4.16a and 4.16b. The first figure shows the current as a function of the phase applied over the junction, while the second figure shows the dependence on the phase drop over the junction with subtraction of the current-induced linear part

$$\varphi - kL_2, \tag{4.73}$$

where k is the linear phase gradient at the edge of the superconductors, which can be determined from a self-consistent calculation. The presence of this linear phase gradient, stemming from a constant current in the electrodes skews the CPRs. The phase gradient seems to obtain its maximal value around $\gamma \approx 5$.

We wish to investigate whether this constant current in the electrodes suppresses the energy gap due to depairing. For this purpose, we look at the absolute value of the pair potential Δ in the superconducting layer as a function of position to try to see the effect of this current as shown in Figure 4.17.

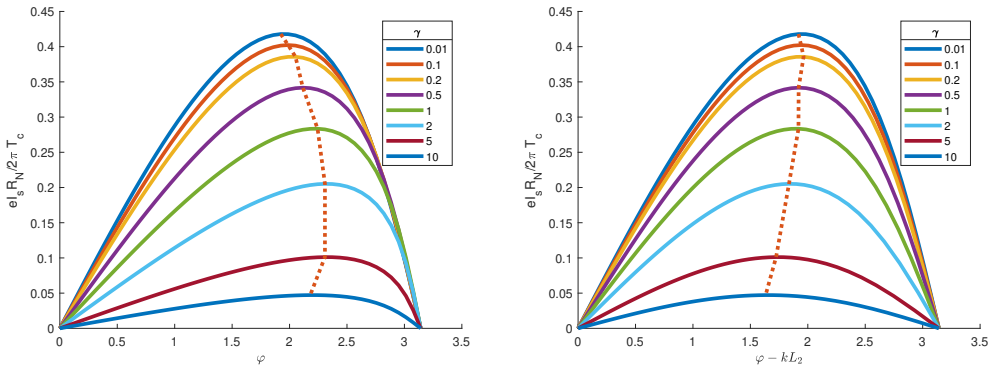

(a) (b)

Figure 4.16: Dependence of the current-phase relationship of the SN-N-NS junction on γ. (a) depicts the dependence of the current on the total junction phase. (b) depicts the dependence of the current on the junction phase with it's linear part subtracted. Parameters used were $\xi = 1$, $\gamma_{BM} = 0.3$, $t = 0.2$, $s = 0.1, L = 5, L_2 = 15, d_S = 5, d_N = 0.2$.

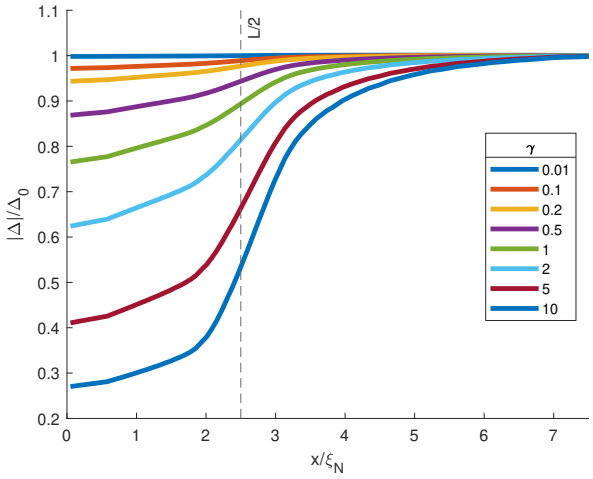

Figure 4.17: Position dependence of the pair potential Δ in the superconductor, calculated for various values of γ. The dashed vertical line corresponds to the edge of the normal metal.

The behavior of Δ shows no sign of suppression due to depairing, it is suppressed in the region above the normal metal and further away grows exponentially towards its bulk value. No region with a reduced value of $|\Delta|$ is found in the superconductors. We believe that this is because the constant

current in the electrodes is not large enough to cause significant suppression. We tried different sets of parameters corresponding to the largest linear phase gradients k, but for none of them we find any sign of depairing.

Chapter 5

SF-F-FS junction

In this chapter, we extend our models for the SN-N-NS junction to the SF-F-FS junction by including the effect of an exchange field. We derive analytical solutions for the current density and the density of states in the 1D limit. Furthermore, we calculate the current density and density of states inside the junction numerically and show that the exchange field can lead to a spin-dependent density of states and a 0-π transition accompanied by the appearance of vortices in the superconductor.

5.1 Mathematical Model

The geometry of the SF-F-FS is identical to that of the SN-N-NS with the normal metal replaced by a ferromagnetic material as sketched in Figure 5.1. This ferromagnetic material has an intrinsic exchange field H. In a ferromagnet the Usadel equation in (2.12) for spin up/down orientations can be written as

$$-iD\nabla\cdot\left[\hat{G}\nabla\hat{G}\right]+\left[\hat{\tau}^3(E\pm H),\hat{G}\right]=0. \tag{5.1}$$

For calculating stationary properties of the SN-N-NS junction we employed the Φ-parametrization. This parametrization is, however, not valid for ferromagnetic materials where the effective Matsubara frequencies $\tilde{\omega}_n=\omega_n+iH$ are not strictly real. Instead we employ an altered version of the Φ-parametrization [47]

$$\hat{G}=\begin{pmatrix}\frac{\tilde{\omega}_n}{\sqrt{\tilde{\omega}_n^2+\Phi_{\omega_n}\Phi^*_{-\omega_n}}} & \frac{\Phi_{\omega_n}}{\sqrt{\tilde{\omega}_n^2+\Phi_{\omega_n}\Phi^*_{-\omega_n}}}\\ \frac{\Phi^*_{-\omega_n}}{\sqrt{\tilde{\omega}_n^2+\Phi_{\omega_n}\Phi^*_{-\omega_n}}} & -\frac{\tilde{\omega}_n}{\sqrt{\tilde{\omega}_n^2+\Phi_{\omega_n}\Phi^*_{-\omega_n}}}\end{pmatrix}. \tag{5.2}$$

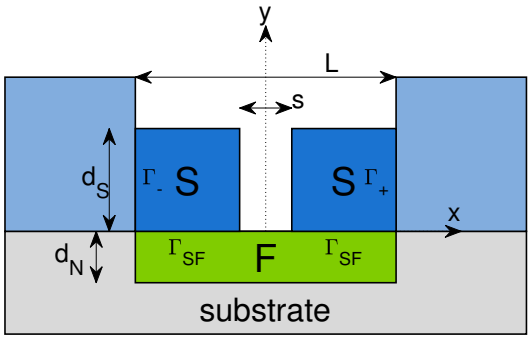

Figure 5.1: Sketch of the SF-F-FS junction. The superconducting material (dark blue) and ferromagnetic material (orange) are deposited on a dielectric substrate (grey). Far away from the weak link region the superconducting materials go over into thicker bulk superconducting electrodes of the same material (light blue). The axis origin lies at the top center of the ferromagnetic strip.

Here $\Phi^*_{-\omega_n}$ denotes the conjugate of the Green's function Φ calculated for the Matsubara frequency $-\omega_n$. This parametrization automatically satisfies the normalization condition. In this parametrization the full Usadel equations in the SF-F-FS junction can be written as

PDEs :

$$\omega_n \Phi_S G_S - \xi^2 \nabla \cdot \left[G_S^2 \nabla \Phi_S \right] = \omega_n \Delta G_S \qquad \text{in } S, \tag{5.3}$$

$$\tilde{\omega}_n \Phi_F G_F - \nabla \cdot \left[G_F^2 \nabla \Phi_F \right] = 0 \qquad \text{in } F, \tag{5.4}$$

Subject to:

$$\nabla \Phi \cdot \mathbf{n} = 0 \qquad \text{on } \Gamma_I, \tag{5.5}$$

$$\frac{\gamma_B G_F}{\tilde{\omega}_n} \nabla \Phi_F \cdot \mathbf{n} = G_S \left(\frac{\Phi_S}{\omega_n} - \frac{\Phi_F}{\tilde{\omega}_n} \right) \qquad \text{on } \Gamma_{SF}, \tag{5.6}$$

$$\frac{\gamma_B \xi G_S}{\omega_n} \nabla \Phi_S \cdot \mathbf{n} = \gamma G_F \left(\frac{\Phi_F}{\tilde{\omega}_n} - \frac{\Phi_S}{\omega_n} \right) \qquad \text{on } \Gamma_{SF}, \tag{5.7}$$

$$\Phi_S = \Delta_0 e^{\pm i\varphi/2} \qquad \text{on } \Gamma_{\pm}, \tag{5.8}$$

where $G_F = \tilde{\omega}_n / \sqrt{\tilde{\omega}_n^2 + \Phi_{F,\omega_n}\Phi^*_{F,-\omega_n}}$.

To calculate the energy-dependent properties of the SF-F-FS junction the Usadel equations need to be solved for real values of E. For this purpose we now do not use the θ, χ-parametrization, which is numerically not always stable, but instead employ the Riccati parametrization. For the SF-F-FS junction the Usadel equations in this parametrization are given by

PDE :

In S :

$$-\xi^2\nabla^2\alpha_S - \xi^2 N_S\beta_S(\nabla\alpha_S)^2 = iE\alpha_S + \frac{\Delta}{2} - \alpha_S^2\frac{\Delta^*}{2}, \tag{5.9}$$

$$-\xi^2\nabla^2\beta_S - \xi^2 N_S\alpha_S(\nabla\beta_S)^2 = iE\beta_S - \frac{\Delta^*}{2} + \beta_S^2\frac{\Delta}{2}, \tag{5.10}$$

In F :

$$-\nabla^2\alpha_F - N_F\beta_F(\nabla\alpha_F)^2 = i(E+H)\alpha_F, \tag{5.11}$$

$$-\nabla^2\beta_F - N_F\alpha_F(\nabla\beta_F)^2 = i(E+H)\beta_F, \tag{5.12}$$

BCs :

On $\Gamma_{\mathbf{I}}$:

$$\nabla\alpha\cdot\mathbf{n} = 0, \tag{5.13}$$

$$\nabla\beta\cdot\mathbf{n} = 0, \tag{5.14}$$

On $\Gamma_{\mathbf{SF}}$:

$$\gamma_B\xi\nabla\alpha_S\cdot\mathbf{n} = \gamma(\alpha_F-\alpha_S)(1-\alpha_S\beta_F)N_F, \tag{5.15}$$

$$\gamma_B\xi\nabla\beta_S\cdot\mathbf{n} = \gamma(\beta_F-\beta_S)(1-\beta_S\alpha_F)N_F, \tag{5.16}$$

$$\gamma_B\nabla\alpha_F\cdot\mathbf{n} = (\alpha_S-\alpha_F)(1-\alpha_F\beta_S)N_S, \tag{5.17}$$

$$\gamma_B\nabla\beta_F\cdot\mathbf{n} = (\beta_S-\beta_F)(1-\beta_F\alpha_S)N_S, \tag{5.18}$$

On $\Gamma_{\pm}$:

$$\alpha_S = \frac{\Delta_0 e^{\pm i\varphi/2}}{-iE + \sqrt{\Delta_0^2 - E^2}}, \tag{5.19}$$

$$\beta_S = \frac{-\Delta_0 e^{\mp i\varphi/2}}{-iE + \sqrt{\Delta_0^2 - E^2}} \tag{5.20}$$

5.2 1D model

In analogy with the SN-N-NS junction, the model of the SF-F-FS junction can be reduced to a one-dimensional model in the limiting case $\gamma \approx 0, d_F \ll 1$. In this case, the Green's functions inside the superconductor are constant and the equations need to be solved only in the ferromagnetic layer.

5.2.1 Supercurrent

The ferromagnetic layer breaks the symmetry of the junction and we can thus not reduce the computations to the region $x \geq 0$ by separating the real and imaginary part of the solution. Instead the equations can be simplified by defining

$$\Phi_+ = \frac{1}{2}(\Phi_{F,\omega_n} + \Phi^*_{F,-\omega_n}), \tag{5.21}$$

$$\Phi_- = \frac{1}{2}(\Phi_{F,\omega_n} - \Phi^*_{F,-\omega_n}). \tag{5.22}$$

These quantities are respectively symmetric and anti-symmetric over the junction. By the assumptions on γ and d_F the Usadel equations in the F layer can be integrated in the y-direction and we obtain the following equations describing the 1D SF-F-FS junction:

$$\frac{d}{dx}\left[G_F^2\frac{d\Phi_+}{dx}\right] = \tilde{\omega}_n\Phi_+ G_F \qquad \text{for } 0 \le x \le s/2, \tag{5.23}$$

$$\frac{d}{dx}\left[G_F^2\frac{d\Phi_-}{dx}\right] = \tilde{\omega}_n\Phi_- G_F \qquad \text{for } 0 \le x \le s/2, \tag{5.24}$$

$$\xi_{eff}^2\frac{d}{dx}\left(G_F^2\frac{d\Phi_+}{dx}\right) - \Phi_+ = -\delta\cos(\varphi/2) \quad \text{for } s/2 \le x \le L/2, \tag{5.25}$$

$$\xi_{eff}^2\frac{d}{dx}\left(G_F^2\frac{d\Phi_-}{dx}\right) - \Phi_- = -i\delta\sin(\varphi/2) \quad \text{for } s/2 \le x \le L/2, \tag{5.26}$$

Subject to :

$$\frac{d}{dx}\Phi_+ = 0,\ \Phi_- = 0 \qquad \text{at } x = 0, \tag{5.27}$$

$$\frac{d}{dx}\Phi_+ = 0,\ \frac{d}{dx}\Phi_- = 0 \qquad \text{at } x = L/2, \tag{5.28}$$

$$\xi_{eff} = \sqrt{\frac{\gamma_{BM}}{G_F(G_S + \tilde{\omega}_n\gamma_{BM})}},$$

$$\delta = \frac{\tilde{\omega}_n\Delta_0 G_S}{\omega_n(G_S + \tilde{\omega}_n\gamma_{BM})}.$$

These equations can be solved analytically in specific cases in analogy with the procedure in [5].

Case 1: $\sqrt{\gamma_{BM}} \ll s \ll \min(1, 1/\sqrt{H})$

In the short junction limit $s \ll \min(1, 1/\sqrt{H})$ the non-gradient terms in (5.23) and (5.24) can be neglected and an analytical solution to these equations can be found satisfying the conditions in (5.27):

$$\Phi_+ = C_1, \tag{5.29}$$

$$\Phi_- = i\sqrt{\tilde{\omega}_n^2 + \Phi_+^2}\tan\left(\frac{2C_2}{s}x\right). \tag{5.30}$$

The coefficients C_1 and C_2 can by found by matching this solution with the one in the region under the S electrodes. From equations (5.25) and (5.28) it is clear that Φ_+ has the constant solution

$$\Phi_+ = \delta\cos(\varphi/2). \tag{5.31}$$

To find Φ_- we try a solution in the form

$$\Phi_- = i\sqrt{\tilde{\omega}_n^2 + \Phi_+^2}\tan(\theta), \tag{5.32}$$

which results in the following equation for the functions θ:

$$\frac{\gamma_{BM}\sqrt{\omega_n^2+\Delta_0^2}}{\Omega_1}\frac{d^2\theta}{dx^2}-\sin\theta=-\frac{\Delta_0\sin\frac{\varphi}{2}}{\Omega_1}\cos\theta, \tag{5.33}$$

with

$$\Omega_1=\sqrt{\Omega^2+\Delta_0^2\cos^2\frac{\varphi}{2}}, \tag{5.34}$$

$$\Omega=\omega_n\Big(1+\frac{\tilde{\omega}_n}{\omega_n}\gamma_{BM}\sqrt{\omega_n^2+\Delta_0^2}\Big). \tag{5.35}$$

From equation (5.33) it follows that the characteristic length scale of θ is

$$\zeta=\left(\frac{\gamma_{BM}\sqrt{\omega_n^2+\Delta_0^2}}{\Omega_1}\right)^{1/2}. \tag{5.36}$$

Now, in the limit $\gamma_{BM}<<s$ the first term can be neglected and we obtain

$$C_2=\operatorname{atan}\left(\frac{\Delta_0\sin\frac{\varphi}{2}}{\Omega_1}\right). \tag{5.37}$$

Then the current density inside the junction can be calculated as

$$J=\frac{i\pi T}{2e\rho}\sum_{\omega_n}\frac{G_F^2}{\tilde{\omega}_n^2}\Big[2\Phi_-\frac{d}{dx}\Phi_+-2\Phi_+\frac{d}{dx}\Phi_-\Big], \tag{5.38}$$

which reduces to

$$\frac{eI_sR_N}{2\pi T_c}=t\sum_{\omega_n}\frac{\Delta_0\cos\frac{\varphi}{2}}{\Omega_1}\operatorname{atan}\left(\frac{\Delta_0\sin\frac{\varphi}{2}}{\Omega_1}\right). \tag{5.39}$$

In the limit $H\to 0$ this reduces to the previously obtained result for the SN-N-NS junction (4.23) and in the limit $H\to 0,\gamma_{BM}\to 0$ this reduces the the KO1 result [43]. In the short junction limit the only difference between a normal metal and a ferromagnetic bridge is thus the additional factor in the definition of Ω. Since this solution is only valid for small values of γ_{BM} and H it cannot be used to explore the full effect of the exchange field. Fortunately, another analytical solution is possible for large values of γ_{BM}.

Case 2:	$s\ll\min(\frac{\gamma_{BM}}{1+\gamma_{BM}},1/\sqrt{H}),\qquad L-S\gg\zeta$

In this limit, equations (5.29)-(5.33) are still valid. The only difference being the constant C_2. To determine this constant we consider the first integral of (5.33)

$$\frac{\gamma_{BM}\sqrt{\omega_n^2+\Delta_0^2}}{2\Omega_1}\left(\frac{d\theta}{dx}\right)^2+\cos\theta-\cos\Theta=\frac{\Delta_0(\sin\Theta-\sin\theta)\sin\frac{\varphi}{2}}{\Omega_1}. \tag{5.40}$$

Here Θ denotes the function θ at $x = L/2$. In the limit $L - S \gg \zeta$ this approaches the value

$$\Theta=\operatorname{atan}\left(\frac{\Delta_0\sin\frac{\varphi}{2}}{\Omega_1}\right). \tag{5.41}$$

A comparison of equations (5.30) and (5.33) at $x = s/2$ shows that the constant C_2 must satisfy

$$\frac{2\eta^2\sqrt{\omega_n^2+\Delta_0^2}}{\Omega_1}C_2^2+\cos C_2-\cos\Theta=\frac{\Delta_0(\sin\Theta-\sin C_2)\sin\frac{\varphi}{2}}{\Omega_1}, \tag{5.42}$$

with $\eta = \sqrt{\gamma_{BM}}/s$. For large values of γ_{BM} the constants C_2 are small and this equation can be reduced to

$$\frac{2\eta^2\sqrt{\omega_n^2+\Delta_0^2}}{\Omega_1}C_2^2+1-\cos\Theta=\frac{\Delta_0(\sin\Theta)\sin\frac{\varphi}{2}}{\Omega_1}, \tag{5.43}$$

which has the solution

$$C_2=\frac{\Delta_0\sin\frac{\varphi}{2}}{\eta\sqrt{2\sqrt{\omega_n^2+\Delta_0^2}}\sqrt{\sqrt{\Omega^2+\Delta^2}+\Omega_1}}. \tag{5.44}$$

The current density inside the junction in this limit is

$$\frac{eI_sR_N}{2\pi T_c}=t\sum_{n=0}^{\infty}\frac{\sqrt{2}\Delta_0^2\sin\varphi}{\Omega_1\sqrt{(\sqrt{\Omega^2+\Delta_0^2}+\Omega_1)\sqrt{\omega_n^2+\Delta_0^2}}}. \tag{5.45}$$

Using this analytical solution we can see the effect of the exchange field by calculating the CPR of the junction as shown in Figure 5.2.

It can be seen that for small values of the exchange field the current-phase relationship has a skewed shape, but by increasing the exchange field the CPR deforms and ultimately changes sign to form a so-called *π-junction*.

The origin of this transition lies at phase jumps at the SF interfaces [21, 47]. In a ferromagnet electrons with different spins have different energies. Ferromagnets thus try to break up Cooper pairs, since these consist of

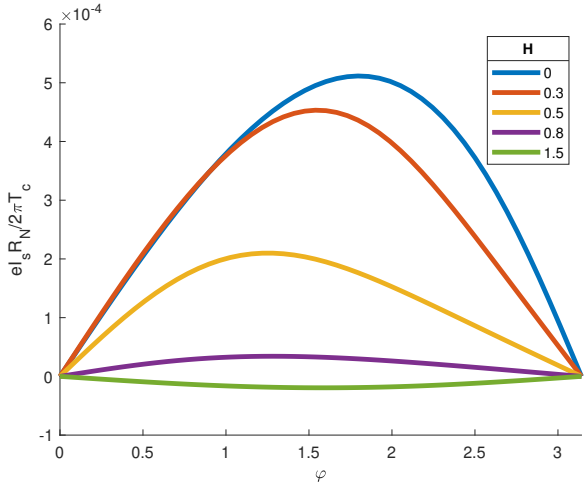

Figure 5.2: Dependence of the current-phase relationship in a short quasi one-dimensional SF-F-FS junction on the exchange field H. Calculated using (5.45) with parameters $\gamma_{BM} = 2, s = 0.01, L = 5, t = 0.1$.

electrons with opposite spin. As a result of this behavior, there is a phase jump at the SF interface that depends on the magnitude of the exchange field. For large enough exchange fields this phase jump reaches its maximum value of $\pi/2$.

The SF-F-FS junction contains two SF interfaces. For a large enough exchange field the total phase over the junction shifts by π resulting in a change of the sign of the supercurrent.

The critical exchange field at which the sign of the current changes depends strongly on the parameter γ_{BM}. Our analytical solutions are only valid for small or large γ_{BM}. For intermediate values of γ_{BM} and larger junction lengths s the one-dimensional Usadel equations need to be solved numerically. A result of this numerical calculation is shown in Figure 5.3, which shows the dependence of the critical current of the SF-F-FS junction on the exchange field H. The kink in the $|I_c(H)|$ graphs occurs at the critical exchange field. This critical exchange field depends on the junction length s, decreasing as s increases.

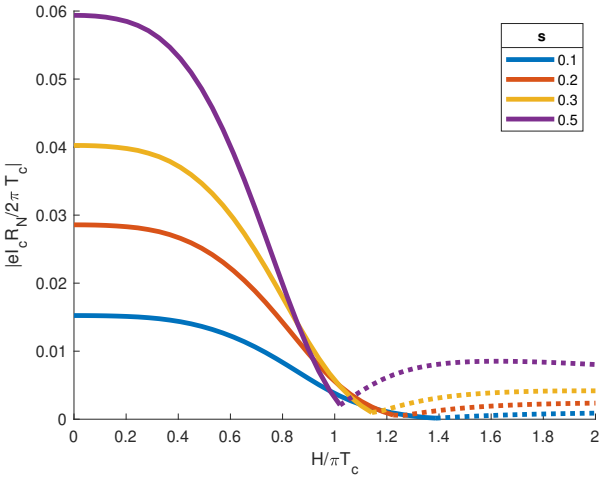

Figure 5.3: Dependence of the critical current in a quasi one-dimensional SF-F-FS junction on the junction length s. Dashed lines indicate the regions with negative critical current. calculated with a FEM model with parameters $\gamma_{BM} = 1, t = 0.1, L = 5$.

It can also be seen that the critical current does not cross zero but makes a jump. This happens because the CPR is not purely sinusoidal but skewed. At the critical temperature the sinusoidal part of the current goes to zero, but the non sinusoidal part does not [48].

For experimentalists it is more convenient to look at the dependence of the critical current on an experimentally variable property such as temperature. This dependence is shown in Figure 5.4. For a large enough exchange field the critical current changes sign as the temperature increases. This effect has been measured to prove the existence of a π-junction [49].

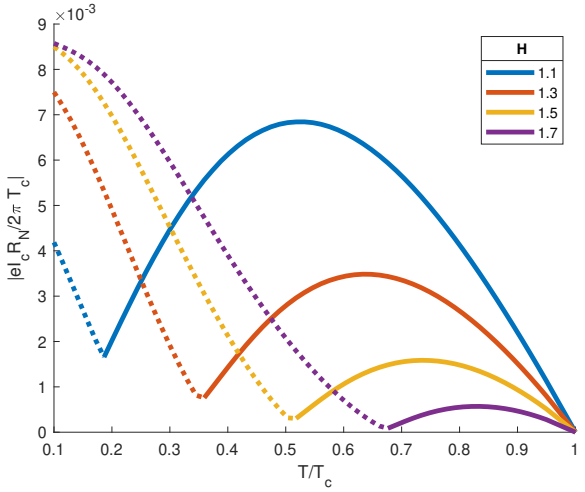

Figure 5.4: Dependence of the critical current in a quasi one-dimensional SF-F-FS junction on temperature. Dashed lines indicate the regions with negative critical current. calculated with a FEM model with parameters $\gamma_{BM} = 1, s = 0.5, L = 1$.

To get a better idea of the location of the transition point we show the dependence of the critical current on the exchange field and the interface transparency in Figure 5.5. It can be seen that a 0-π transition can occur both when increasing the exchange field and when increasing γ_{BM}.

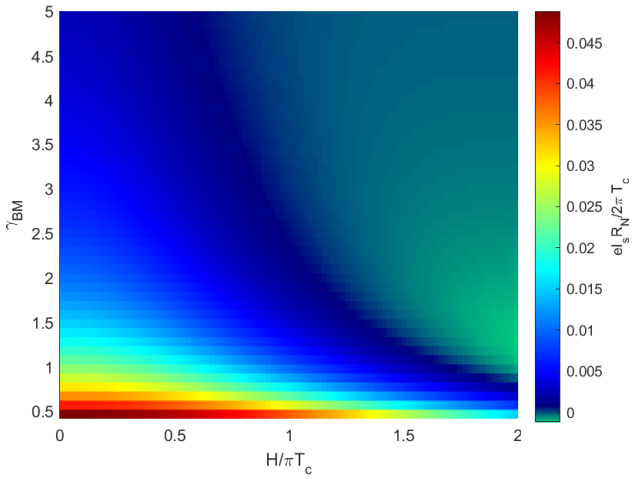

Figure 5.5: Dependence of the critical current of a one-dimensional SF-F-FS junction on the exchange field and the interface transparency. Green colors indicate negative critical currents. calculated with a FEM model with parameters $s = 0.3, L = 1, t = 0.5$.

5.2.2 Density of states

The presence of an exchange field also has an influence on the density of states inside the ferromagnetic layer. This density of states becomes spin-dependent since the exchange field separates the energy levels of particles with different spins. For a particular spin, the exchange field shifts the junction energy, causing an asymmetry between the density of states at positive and negative energies.

Before we give numerical results on the density of states we will first derive an illustrative analytical solution. This can be most conveniently done in the θ, χ-parametrization, using equations (4.26)-(4.31) and by replacing E by $E \pm H$ in the ferromagnetic layer.

In the short junction limit ($s \ll 1/\sqrt{H}$) the solution at the center part of the junction is given by [46]

$$\theta_F = \operatorname{acos}\left(\frac{\sqrt{\alpha^2+1}}{\alpha}\cos[j_E \alpha x]\right), \tag{5.46}$$

$$\chi_F = \operatorname{atan}\left(i\alpha \tan[j_E \alpha x]\right). \tag{5.47}$$

The constants j_E and α can be obtained by enforcing continuity of the solu-

tion at $x = s/2$, which leads to the following equations:

$$\sin\theta_S \sin\theta_F \sin(\chi_S - \chi_F) = 0, \tag{5.48}$$

$$i(E \pm H)\gamma_{BM} \sin\theta_S + \cos\theta_F \sin\theta_S \cos(\chi_S - \chi_F) - \sin\theta_F \cos\theta_S = 0. \tag{5.49}$$

By solving these equations the constants j_E and α can be determined to be

$$\alpha = \frac{\sqrt{\tilde{E}^2 - \Delta_0^2 \cos^2(\varphi/2)}}{\Delta_0 \cos(\varphi/2)}, \tag{5.50}$$

$$j_E = \frac{2\Delta_0 \cos(\varphi/2)}{s\sqrt{\tilde{E}^2 - \Delta_0^2 \cos^2(\varphi/2)}} \operatorname{acos}\left(\sqrt{\frac{\tilde{E}^2 - \Delta_0^2 \cos^2(\varphi/2)}{\tilde{E}^2 - \Delta_0^2}}\right), \tag{5.51}$$

$$\tilde{E} = E + \gamma_{BM}(E \pm H)\sqrt{\Delta_0^2 - E^2}. \tag{5.52}$$

At the center of the junction ($x = 0$) the density of states is then given by

$$N(E, 0) = \mathrm{Re}\left[\frac{\tilde{E}}{\sqrt{\tilde{E}^2 - \tilde{\Delta}_0^2}}\right]. \tag{5.53}$$

The density of states at the Fermi level is

$$N(0, 0) = \mathrm{Re}\left[\frac{\gamma_{BM} H}{\sqrt{(\gamma_{BM} H)^2 - 1}}\right]. \tag{5.54}$$

For small values of the exchange field the density of states contains a gap around the Fermi level, but ones the exchange field surpasses the value $H = 1/\gamma_{BM}$ this gap is completely filled. Further increasing the exchange field reduces the density of states to its normal non-superconducting shape. This formula for the density of states has also been derived for SFIFS type junctions [47].

For numerical calculations of the density of states inside the SF-F-FS junction it is the most convenient to use the Riccati parametrization of the Usadel equations. In the one-dimensional limit these equations reduce to

$$|\mathbf{x}| \leq \mathbf{s/2}:$$

$$-\frac{d^2\alpha_F}{dx^2} - 2N_F\beta_F\left(\frac{d\alpha_F}{dx}\right)^2 = i(E + H)\alpha_F \tag{5.55}$$

$$-\frac{d^2\beta_F}{dx^2} - 2N_F\alpha_F\left(\frac{d\beta_F}{dx}\right)^2 = i(E + H)\beta_F \tag{5.56}$$

$$\mathbf{s/2 \leq |x| \leq L/2}: \tag{5.57}$$

$$-\gamma_{BM}\frac{d^2\alpha_F}{dx^2} - 2\gamma_{BM}N_F\beta_F\left(\frac{d\alpha_F}{dx}\right)^2 = i(E+H)\gamma_{BM}\alpha_F + (\alpha_S - \alpha_F)(1-\alpha_F\beta_S)N_S \tag{5.58}$$

$$-\gamma_{BM}\frac{d^2\beta_F}{dx^2} - 2\gamma_{BM}N_F\alpha_F\left(\frac{d\beta_F}{dx}\right)^2 = i(E+H)\gamma_{BM}\beta_F + (\beta_S - \beta_F)(1-\beta_F\alpha_S)N_S \tag{5.59}$$

Subject to:

$$\frac{d}{dx}\alpha_F = 0, \quad \frac{d}{dx}\beta_F = 0 \qquad \text{at } |x| = \frac{L}{2}, \tag{5.60}$$

$$\alpha_S = \frac{\Delta_0 e^{i\varphi}}{-iE + \sqrt{|\Delta_0|^2 - E^2}}, \tag{5.61}$$

$$\beta_S = \frac{-\Delta_0 e^{-i\varphi}}{-iE + \sqrt{|\Delta_0|^2 - E^2}}. \tag{5.62}$$

Using these equations the density of states can be calculated for each spin projection. For one spin projection the energies are shifted upwards by the exchange field ($E \to E+H$), while for the other spin the energies are lowered ($E \to E-H$). The total density of states is the sum of the two spin resolved densities. The results of an example calculation of these quantities are shown in Figures 5.6a-5.6c.

For nonzero values of the exchange field the spin resolved density of states loses its symmetry around $E = 0$. For spin up electrons the density of states smears out at negative energies, lowering the subgap, while at positive energies the density of states becomes sharper, increasing the subgap. For spin down electrons the effect of the exchange field on the density of states is exactly opposite. The total density of states remains symmetric. In the presence of an exchange field the characteristic peak at $E = \Delta_0$ remains, but decreases in height as the exchange field increases. The subgap decreases with an increasing exchange field and has completely closed at $H = 1.5$.

The dependence of this energy gap on the exchange field is shown more accurately in Figure 5.7. It can be seen that the energy gaps decreases linearly with the exchange field. Furthermore, for large values of the exchange field the density of states converges towards its value in the normal state and the height of the characteristic peaks at $E = \pm\Delta_0$ diminishes.

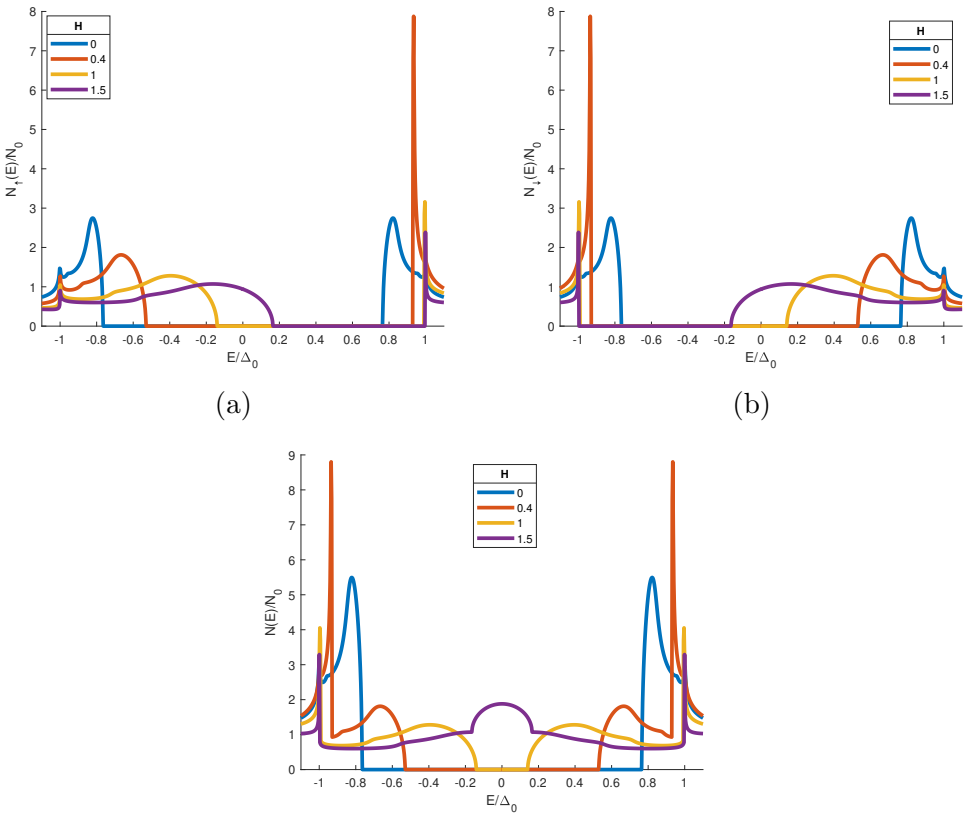

Figure 5.6: Density of states at the center of a one-dimensional SF-F-FS junction for various values of the exchange field. (a) density of states for spin-up electrons (b) density of states for spin-down electrons (c) total density of states. calculated with a FEM model with parameters $\gamma_{BM} = 0.3, \varphi = 0.6, s = 1, L = 5$.

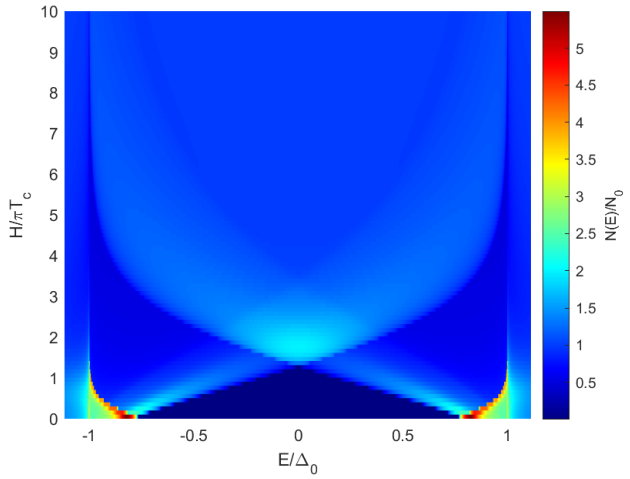

Figure 5.7: Normalized density of states at the center of a one-dimensional SF-F-FS junction as a function of the energy and the exchange field. calculated with a FEM model with parameters $\gamma_{BM} = 0.3, \varphi = 0.6, s = 1, L = 5$.

5.3 2D model

The above described one-dimensional model can be extended to two dimensions to take into account the effect of the ferromagnetic layer thickness d_F and the proximity effect parameter γ and to investigate the behavior of currents inside the superconductors.

Close to the 0-π transition, the current distribution inside the SF-F-FS junction is remarkably different from that of the SN-N-NS junction. This current distribution is shown in Figures 5.8a and 5.8b. The current is mostly located in the ferromagnetic material. In contrast to the non-ferromagnetic case the current density is not highest in the region between the superconducting electrodes, but just outside this region under the electrodes. This shift is accompanied by a vortex-like behavior of the current density in the superconductor. These vortices occur when the exchange field in the ferromagnet is not strong enough to flip the direction of the current in the full superconductor. The two opposite flows of currents in the superconductor cause the vortices. For larger exchange fields the directions of the currents in the superconductors become homogeneous and the vortices vanish.

This occurrence of vortices in the junction is a good example of behavior that can only be described by a two-dimensional model. In the one-dimensional model, the phases inside the superconductors are assumed constant, while vortices can only appear in the presence of phase gradients.

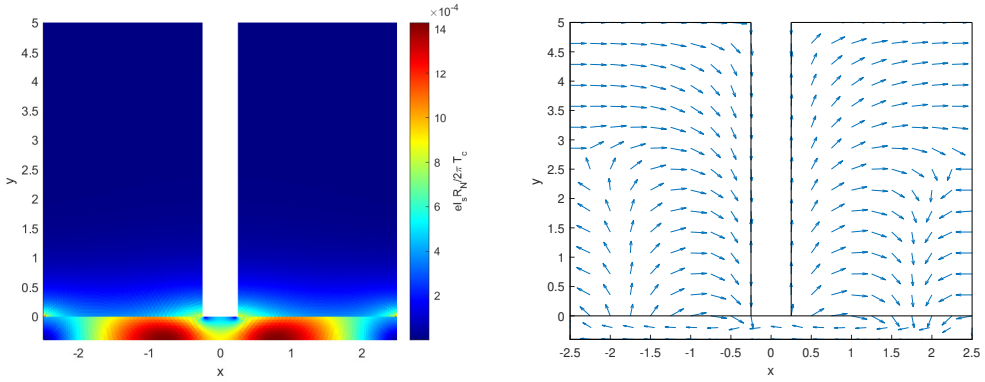

(a) (b)

Figure 5.8: Current density inside an SF-F-FS junction. (a) depicts the absolute value of the current, (b) depicts the direction field inside the junction. calculated with parameters $\gamma_{BM} = 1, \gamma = 0.1, t = 0.1, s = 0.5, L = 5, d_F = 0.4, d_S = 5, \xi = 1, \varphi = \pi/2, H = 1.12$.

The dependence of the critical current on d_F and γ is shown in Figures 5.9a and 5.9b. It can be seen that just as in the SN-N-NS junction the critical current decreases with increasing d_F and γ due to current spreading and suppression of the superconductivity in the electrodes. Only near the critical exchange field this does not hold. Furthermore, it can be seen that the critical exchange field decreases significantly as d_F increases, while it only changes slightly when varying γ. In the limit $d_F \to 0, \gamma \to 0$ the results converge to the result obtained in the 1D model.

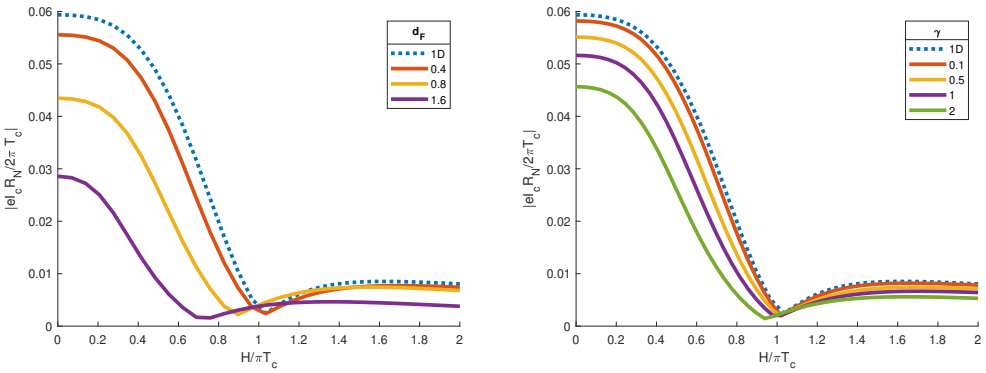

(a) (b)

Figure 5.9: Dependence of the critical current in an SF-F-FS junction on (a) d_F with $\gamma = 0.1$ fixed (b) γ with $d_F = 0.1$ fixed. The dashed line indicates the dependence obtained in the one-dimensional model. calculated with parameters $\gamma_{BM} = 1, t = 0.1, s = 0.5, L = 5, d_S = 5$.

Chapter 6

Conclusion and Outlook

6.1 Conclusion and Discussion

The goal of this thesis was to construct and implement a two-dimensional model of the SN-N-NS Josephson junction and to calculate quantities of interest such as the supercurrent density distribution and the density of states throughout this junction.

We implemented a stable numerical scheme to solve the 1D and 2D Usadel equations on the SN-N-NS junction using the Φ-parametrization and calculated the supercurrent densities. The numerical solutions correspond well to analytical solutions in the 1D limit found in literature. The 2D model allowed us to determine the distribution of the current density not only inside the normal metal but also inside the superconductors. This allowed us to take into account the inverse proximity effect and to accurately calculate current distributions inside the whole junction. Knowledge of these distributions might aid experimentalists in the designing of new junctions with desired properties.

Next, we extended our study of the SN-N-NS junction to real energies and calculated the density of states. We derived analytical expressions for the density of states in the one-dimensional limit, and implemented numerical discretizations for the 1D and 2D junctions based on the θ, χ-parametrization. The numerical results in 1D were consistent with the analytical solutions. The two-dimensional model generalized these results and allowed the determination of the density of states in the complete junction for all junction parameters and geometries.

In hindsight the θ, χ-parametrization was not the most convenient scheme to use for these calculations. Due to the periodicity of the Green's functions in this parametrization it induced additional unphysical solutions, and due

to the unboundedness of θ it was numerically not always stable, requiring a global Newton method and an accurate initial guess for convergence. It is worth noting that the stability of the scheme depends on the phase difference. The scheme is stable for small phase differences, while it becomes less stable as the phase difference approaches π. This makes this parametrization suitable for calculations in bilayers with zero phase difference, but not for Josephson junctions. Other parametrizations, such as the Riccati parametrization promise to be more stable for these junctions.

We also extended our model of the SN-N-NS junction to a junction with current inflow boundary conditions. For this type of junction it is predicted that a large enough current in the superconducting electrodes may cause depairing effects and thereby decreases the pair potential. In our numerical results we however did not observe this phenomenon. One reason for this discrepancy might be that we did not choose optimal junction parameters that maximize the current flowing in the superconductors and therefore the depairing. In addition, in our model we fix the magnitudes of the Green's functions and the pair potential at the boundaries $\Gamma_\pm$ to their bulk value. This might also be the reason of the regular exponential behavior of the pair potential in the electrodes, rather than it having a reduced value.

Lastly, we considered the case of an SF-F-FS junction. We derived analytical solution for the supercurrent density in the one-dimensional limit, illustrating how the exchange field leads to a 0-π transition. We constructed numerical schemes for the solving the full 1D and 2D model and applied it to calculate current distributions inside the junction and showed that near the transition point vortices can appear in the superconductors. We also implemented a numerically stable 1D scheme based on the Riccati parametrization to calculate the density of states and showed how an exchange field leads to a decrease of the energy gap, and eventually an overall decrease of the density of states. Unfortunately, due to time constraints we were not able to extend this model to two dimensions.

6.2 Outlook

Even after one year of hard work we were not able to solve every problem we wanted to tackle. Below we will discuss some interesting starting points and suggestions for future research based on our work:

- **θ, χ-parametrization vs Riccati parametrization** To calculate the density of states in the SN-N-NS junction we used the θ, χ-parametrization. This parametrization proved very useful for deriving analytical solutions, but not for numerical calculations due to instabilities. For cal-

culations on the SF-F-FS junction we instead considered the Riccati parametrization. This parametrization turned out to be much faster and numerically more stable. We thus recommend using the Riccati parametrization for future numerical research on solving the real energy Usadel equations.

- **Depairing in electrodes due to current-injection**
  In section 4.4 we investigated the case of homogeneous current-injection into the SN-N-NS junction. We did, however, not observe any depairing effects in this setting. We believe that this is either because of sub-optimal parameter choices leading to small currents in the superconductor or because of the boundary conditions imposed on the superconductors. For future work we suggest that it should be investigated what the optimal parameters are and whether other types of boundary conditions which better model current inflow might be suitable in this setting.

- **Investigating the SF-F-FS junction**
  In Chapter 5, we investigated the SF-F-FS junction by including the effect of an exchange field. Due to time constraints we did not manage to fully treat this junction. In particular, it would be interesting to further investigate the formation and behavior of vortices in the current density near the critical exchange field and to implement a 2D numerical discretization based on the Riccati parametrization to calculate the density of states inside the full junction and to investigate how this distribution differs from that inside a SN-N-NS junction.

- **Topological junctions**
  In our work we set up the machinery to solve the Usadel equations in two dimensions. This machinery can be used to consider also other types of junctions than the ones considered in this thesis. Recently, versions of the Usadel equations for topological materials have been derived [50, 51]. These equations are very similar to the regular Usadel equations except for their treatment of an exchange field. It might thus be interesting to investigate the properties of junctions consisting of topological and ferromagnetic materials based on our models. To our knowledge this has not been attempted before.

Bibliography

[1] D. S. Holmes, A. L. Ripple, and M. A. Manheimer. Energy-efficient superconducting computing—power budgets and requirements. *IEEE Transactions on Applied Superconductivity*, 23(3):1701610–1701610, June 2013.

[2] S. K. Tolpygo. Superconductor digital electronics: Scalability and energy efficiency issues (review article). *Low Temperature Physics*, 42(5):361–379, May 2016.

[3] A. I. Braginski. Superconductor electronics: Status and outlook. *Journal of Superconductivity and Novel Magnetism*, 32(1):23–44, November 2018.

[4] V. K. Semenov, Yu. A. Polyakov, and S. K. Tolpygo. Very large scale integration of Josephson-junction-based superconductor random access memories. *IEEE Transactions on Applied Superconductivity*, 29(5):1–9, August 2019.

[5] I. I. Soloviev, S. V. Bakurskiy, V. I. Ruzhickiy, N. V. Klenov, M. Yu. Kupriyanov, A. A. Golubov, O. V. Skryabina, and V. S. Stolyarov. Nano-scale Josephson junction for digital superconducting circuits. *preprint*, 2020.

[6] J. C. Cuevas and F. S. Bergeret. Magnetic interference patterns and vortices in diffusive SNS junctions. *Physical Review Letters*, 99(21):217002, November 2007.

[7] F. S. Bergeret and J. C. Cuevas. The vortex state and Josephson critical current of a diffusive SNS junction. *Journal of Low Temperature Physics*, 153(5-6):304–324, October 2008.

[8] M. Amundsen and J. Linder. General solution of 2D and 3D superconducting quasiclassical systems: coalescing vortices and nanoisland geometries. *Scientific Reports*, 6(1), March 2016.

[9] V. S. Stolyarov, T. Cren, C. Brun, I. A. Golovchanskiy, O. V. Skryabina, D. I. Kasatonov, M. M. Khapaev, M. Yu. Kupriyanov, A. A. Golubov, and D. Roditchev. Expansion of a superconducting vortex core into a diffusive metal. *Nature Communications*, 9(1), June 2018.

[10] P. M. Marychev and D. Yu. Vodolazov. A Josephson junction based on a highly disordered superconductor/low-resistivity normal metal bilayer. *Beilstein Journal of Nanotechnology*, 11:858–865, June 2020.

[11] H. K. Onnes. *Leiden Comm.*, page 124c, 1911.

[12] W. Meissner and R. Ochsenfeld. Ein neuer effekt bei eintritt der supraleitfähigkeit. *Die Naturwissenschaften*, 21(44):787–788, November 1933.

[13] F. London and H. London. The electromagnetic equations of the supraconductor. *Proceedings of the Royal Society of London. Series A - Mathematical and Physical Sciences*, 149(866):71–88, March 1935.

[14] V. L. Ginzburg and L. D. Landau. On the theory of superconductivity. *Zhurnal Eksperimentalnoi i Teoreticheskoi Fiziki*, 20:1064, 1950. [Sov. Phys. JETP, 20:1-64, 1950].

[15] J. Bardeen, L. N. Cooper, and J. R. Schrieffer. Theory of superconductivity. *Physical Review*, 108(5):1175–1204, December 1957.

[16] L. P. Gor'kov. On the energy spectrum of superconductors. *Journal of Experimental and Theoretical Physics*, 7(3):505–508, September 1958.

[17] L. N. Cooper. Bound electron pairs in a degenerate Fermi gas. *Physical Review*, 104(4):1189–1190, November 1956.

[18] E. Thuneberg and R Hänninen. Numerical computation of the BCS gap function and other related functions. Unpublished.

[19] A.F. Andreev. The thermal conductivity of the intermediate state in superconductors. *Zhurnal Eksperimentalnoi i Teoreticheskoi Fiziki*, 46(5), 1964. [Sov. Phys. JETP, 46(5):1228-1231, 1964].

[20] B. D. Josephson. Possible new effects in superconductive tunnelling. *Physics Letters*, 1(7):251–253, July 1962.

[21] A. A. Golubov, M. Yu. Kupriyanov, and E. Il'ichev. The current-phase relation in Josephson junctions. *Reviews of Modern Physics*, 76(2):411–469, April 2004.

[22] Stoner criterion — Wikipedia, the free encyclopedia, 2020. accessed 25 May 2021.

[23] R. D. Mattuck. *A Guide to Feynman Diagrams in the Many-Body Problem: Second Edition*. Dover Books on Physics. Dover Publications, 2012.

[24] Y. Nambu. Quasi-particles and gauge invariance in the theory of superconductivity. *Physical Review*, 117(3):648–663, February 1960.

[25] A. I. Larkin and Yu. N. Ovchinnikov. Quasiclassical method in the theory of superconductivity. *Journal of Experimental and Theoretical Physics*, 28(6):1200–1205, June 1969.

[26] Gert Eilenberger. Transformation of Gorkov's equation for type II superconductors into transport-like equations. *Zeitschrift für Physik A Hadrons and nuclei*, 214(2):195–213, April 1968.

[27] Klaus D. Usadel. Generalized diffusion equation for superconducting alloys. *Physical Review Letters*, 25(8):507–509, August 1970.

[28] V. Chandrasekhar. An introduction to the quasiclassical theory of superconductivity for diffusive proximity-coupled systems. In *The Physics of Superconductors*, pages 55–110. Springer Berlin Heidelberg, December 2004.

[29] W. Belzig, F. K. Wilhelm, C. Bruder, G. Schön, and A. D Zaikin. Quasiclassical Green's function approach to mesoscopic superconductivity. *Superlattices and Microstructures*, 25(5-6):1251–1288, May 1999.

[30] T. Matsubara. A new approach to quantum-statistical mechanics. *Progress of Theoretical Physics*, 14(4):351–378, October 1955.

[31] T. H. Stoof and Yu. V. Nazarov. Kinetic-equation approach to diffusive superconducting hybrid devices. *Physical Review B*, 53(21):14496–14505, June 1996.

[32] N. Schopohl and K. Maki. Quasiparticle spectrum around a vortex line in ad-wave superconductor. *Physical Review B*, 52(1):490–493, July 1995.

[33] M. Yu. Kupriyanov and V. F. Lukichev. Influence of boundary transparency on the critical current of "dirty" SS′S structures. *Journal of Experimental and Theoretical Physics*, 67(6):1163–1168, June 1988.

[34] J. van Kan, A. Segal, and F. J. Vermolen. *Numerical methods in scientific computing*, pages 116–117. Delft Academic Press, 2014.

[35] F. Cuvelier, C. Japhet, and G. Scarella. An efficient way to assemble finite element matrices in vector languages. *BIT Numerical Mathematics*, 56(3):833–864, December 2015.

[36] D. Kahaner, C. Moler, and S. Nash. *Numerical Methods and Software*. Prentice-Hall, Inc., USA, 1989.

[37] D. A. Dunavant. High degree efficient symmetrical Gaussian quadrature rules for the triangle. *International Journal for Numerical Methods in Engineering*, 21(6):1129–1148, June 1985.

[38] C. T. Kelley. *Iterative Methods for Linear and Nonlinear Equations*. Society for Industrial and Applied Mathematics, January 1995.

[39] J. E. Dennis and Robert B. Schnabel. *Numerical Methods for Unconstrained Optimization and Nonlinear Equations*. Society for Industrial and Applied Mathematics, January 1996.

[40] D. G. Anderson. Iterative procedures for nonlinear integral equations. *Journal of the ACM*, 12(4):547–560, October 1965.

[41] P. P. Pratapa and P. Suryanarayana. Restarted Pulay mixing for efficient and robust acceleration of fixed-point iterations. *Chemical Physics Letters*, 635:69–74, August 2015.

[42] P. G. Ciarlet. *The Finite Element Method for Elliptic Problems*, pages 79–81. Society for Industrial and Applied Mathematics, January 2002.

[43] I. O. Kulik and A. N. Omelyanchuk. Contribution to the microscopic theory of the Josephson effect in superconducting bridges. *JETP Lett.*, 21(4):96–97, February 1975.

[44] A. A. Golubov and M. Yu. Kupriyanov. The Josephson effect in SNINS and SNIS tunnel junctions with finite transparency of the SN boundaries. *Journal of Experimental and Theoretical Physics*, 96(4):805–812, October 1989.

[45] A. A. Golubov, E. P. Houwman, J. G. Gijsbertsen, V. M. Krasnov, J. Flokstra, H. Rogalla, and M. Yu. Kupriyanov. Proximity effect in superconductor-insulator-superconductor Josephson tunnel junctions: Theory and experiment. *Physical Review B*, 51(2):1073–1089, January 1995.

[46] T. T. Heikkilä, J. Särkkä, and F. K. Wilhelm. Supercurrent-carrying density of states in diffusive mesoscopic Josephson weak links. *Physical Review B*, 66(18):184513, November 2002.

[47] A. A. Golubov, M. Yu. Kupriyanov, and Ya. V. Fominov. Critical current in SFIFS junctions. *Journal of Experimental and Theoretical Physics Letters*, 75(4):190–194, February 2002.

[48] A. A. Golubov and M. Yu. Kupriyanov. The current phase relation in Josephson tunnel junctions. *Journal of Experimental and Theoretical Physics Letters*, 81(7):335–341, April 2005.

[49] V. V. Ryazanov, V. A. Oboznov, A. Yu. Rusanov, A. V. Veretennikov, A. A. Golubov, and J. Aarts. Coupling of two superconductors through a ferromagnet: Evidence for a pi junction. *Physical Review Letters*, 86(11):2427–2430, March 2001.

[50] A. Zyuzin, M. Alidoust, and D. Loss. Josephson junction through a disordered topological insulator with helical magnetization. *Physical Review B*, 93(21), June 2016.

[51] H. G. Hugdal, J. Linder, and S. H. Jacobsen. Quasiclassical theory for the superconducting proximity effect in Dirac materials. *Physical Review B*, 95(23), June 2017.

[52] M. M. Khapaev, M. Yu. Kupriyanov, S. V. Bakurskiy, N. V. Klenov, and I. I. Soloviev. Modeling superconductor SFN-structures using the finite element method. *Differential Equations*, 56(7):959–967, July 2020.

[53] C. Evans, S. Pollock, L. G. Rebholz, and M. Xiao. A proof that Anderson acceleration improves the convergence rate in linearly converging fixed-point methods (but not in those converging quadratically). *SIAM Journal on Numerical Analysis*, 58(1):788–810, January 2020.

Appendix A

Numerical implementation SN-N-NS Junction

In this appendix, we present the solution procedure for the self-consistency equations. We will also discuss the derivation of the weak formulations and resulting systems of algebraic equations obtained by applying the finite element method to the Usadel equations in the different parametrizations. Additionally, we provide a convergence test of our fixed-point iterations to validate our code.

The full code used to obtain all results in this thesis can be found online at https://github.com/vbosboom/Usadel.

A.1 Self-consistency equation

For a complete description of a superconducting junction the Usadel equations need to be solved together with the self-consistency equation

$$\Delta \ln t + 2t \sum_{n=0}^{\infty} \left[\frac{\Delta}{\omega_n} - \frac{\Phi(\omega_n)}{\sqrt{\omega_n^2 + |\Phi|^2}} \right] = 0. \tag{A.1}$$

Solving this equation requires the solution $\Phi(\omega_n)$ of the Usadel equations at all Matsubara frequencies $0 \leq \omega_n < \infty$. For a numerical calculation, a finite cutoff-frequency ω_{max} has to be chosen. A good criterion for this cutoff-frequency is $\omega_{max} \gg \Delta$. In our code we choose $\omega_{max} = 5\Delta$. This provides sufficient accuracy for our calculations.

Since the solutions of the Usadel equations depend on Δ and vice versa these quantities have to be calculated in a coupled fashion. For this purpose

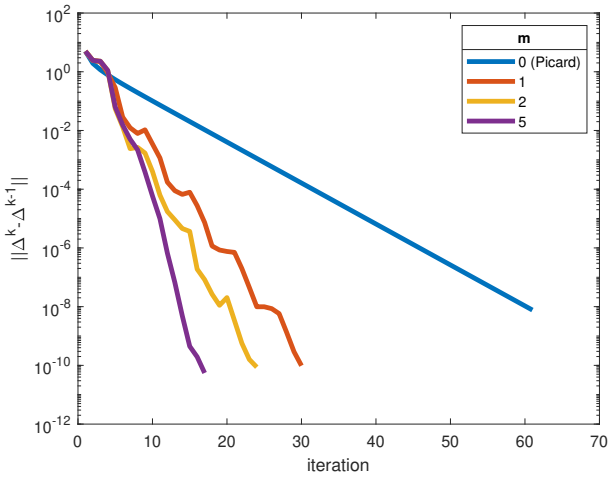

Figure A.1: Convergence of the Anderson-Picard method for the self-consistency equations using different acceleration coefficients m.

the self-consistency equation is rewritten into a different form:

$$\Delta = \frac{2t \sum_{n=0}^{\infty} \frac{\Phi(\omega_n)}{\sqrt{\omega^2 + |\Phi|^2}}}{\ln t + 2t \sum_{n=0}^{\infty} \frac{1}{\omega_n}}. \tag{A.2}$$

In this form the self-consistency equation can be solved using a fixed-point method such as the Picard iteration. This method is very stable, but the convergence is quite slow.

To improve convergence we applied Anderson's acceleration method with restarts to the self-consistency equation [40, 41, 52, 53]. This significantly accelerates the convergence rate of the self-consistency equation as illustrated in Figure A.1. Based on test calculations we chose the acceleration parameter $m = 5$ as parameter during our computations. The iterative process was continued until the pair potential converged within a tolerance of 10^{-5}.

A.2 θ, χ-parametrization

A.2.1 Weak formulation and system of equations

Suppose we want to solve the Usadel equations in the θ, χ-parametrization (4.7)-(4.18) on the SN-N-NS junction shown in Figure 4.1. To derive the weak formulation and the resulting system of algebraic equations we follow a similar approach as we did for the Φ-parametrization in Chapter 3. For

the weak formulation we consider the equations in the S_1 region as an example:

PDE :

In $\mathbf{S_1}$:

$$-\xi^2\nabla^2\theta_S + \xi^2 \sin\theta_S \cos\theta_S (\nabla\chi_S)^2 = iE\sin\theta_S + \frac{1}{2}\cos\theta_S\big(\Delta e^{-i\chi_S} + \Delta^* e^{i\chi_S}\big), \tag{A.3}$$

$$-\xi^2\nabla\cdot\Big[\sin^2\theta_S\nabla\chi_S\Big] = -\frac{i}{2}\sin\theta_S\big(\Delta e^{-i\chi_S} - \Delta^* e^{i\chi_S}\big), \tag{A.4}$$

Subject to :

On $\mathbf{\Gamma_I}$:

$$\nabla\theta_S\cdot\mathbf{n} = 0, \tag{A.5}$$

$$\nabla\chi_S\cdot\mathbf{n} = 0, \tag{A.6}$$

On $\mathbf{\Gamma_{SN}}$:

$$\gamma_B\xi\sin^2\theta_S\nabla\chi_S\cdot\mathbf{n} = \gamma\sin\theta_N\sin\theta_S\sin(\chi_N-\chi_S), \tag{A.7}$$

$$\gamma_B\xi\nabla\theta_S\cdot\mathbf{n} = \gamma\big[\sin\theta_N\cos\theta_S\cos(\chi_N-\chi_S) - \cos\theta_N\sin\theta_S\big], \tag{A.8}$$

On $\mathbf{\Gamma_-}$:

$$\cos\theta_S = \frac{E}{\sqrt{E^2-\Delta_0^2}}, \tag{A.9}$$

$$\chi_S = -\frac{\varphi}{2}. \tag{A.10}$$

In the θ,χ-parametrization the Usadel equations transform into two coupled partial differential equations. The weak formulation will thus consist of two parts as well. Following the same approach as for the Φ-parametrization the following weak formulation is obtained:

$$\begin{aligned}\xi^2\int_S\nabla\theta_S\cdot\nabla\eta_S dS = \int_S\eta_S\big[&-\xi^2\sin\theta_S\cos\theta_S(\nabla\chi_S)^2 \\ &+ iE\sin\theta_S + \frac{1}{2}\cos\theta_S(\Delta e^{-i\chi_S}+\Delta^* e^{i\chi_S})\big]dS \\ +\frac{\xi\gamma}{\gamma_B}\int_{\Gamma_{SN}}&\eta_S[\sin\theta_N\cos\theta_S\cos(\chi_N-\chi_S)-\cos\theta_N\sin\theta_S]d\Gamma,\end{aligned} \tag{A.11}$$

and

$$\xi^2 \int_S \sin^2\theta_S \nabla\chi_S \cdot \nabla\eta_S dS = -\frac{i}{2}\int_S \sin\theta_S(\Delta e^{-i\chi_S} - \Delta^* e^{i\chi_S})dS + \frac{\xi\gamma}{\gamma_B}\int_{\Gamma_{SN}} \eta_S \sin\theta_N \sin\theta_S \sin(\chi_N - \chi_S)d\Gamma. \quad \text{(A.12)}$$

Similar weak formulations can be derived in the S_2 and N regions. We expand the solutions into the Lagrangian basis functions:

$$\theta_{S_1} \approx \tilde{\theta}_{S_1} = \sum_{j=1}^{n_{S_1}} \theta_{1,j}\phi_{S_1,j}, \qquad \chi_{S_1} \approx \tilde{\chi}_{S_1} = \sum_{j=1}^{n_{S_1}} \chi_{1,j}\phi_{S_1,j},$$

$$\theta_{S_2} \approx \tilde{\theta}_{S_2} = \sum_{j=1}^{n_{S_2}} \theta_{2,j}\phi_{S_2,j}, \qquad \chi_{S_2} \approx \tilde{\chi}_{S_2} = \sum_{j=1}^{n_{S_2}} \chi_{2,j}\phi_{S_2,j},$$

$$\theta_N \approx \tilde{\theta}_N = \sum_{j=1}^{n_N} \theta_{N,j}\phi_{N,j}, \qquad \chi_N \approx \tilde{\chi}_N = \sum_{j=1}^{n_N} \chi_{N,j}\phi_{N,j}.$$

Introducing these expansions into the weak formulation (A.11)-(A.12) yields the following system of equations

$$S(u)u = f(u),$$

with

$$S(u) = \text{diag}\begin{pmatrix} S_{1,1} \\ S_{1,2}(u) \\ S_{2,1} \\ S_{2,2}(u) \\ S_{N,1} \\ s_{N,2}(u) \end{pmatrix},$$

$$u = \begin{pmatrix} \tilde{\theta}_1 \\ \tilde{\chi}_1 \\ \tilde{\theta}_2 \\ \tilde{\chi}_2 \\ \tilde{\theta}_N \\ \tilde{\chi}_N \end{pmatrix},$$

$$f(u) = \begin{pmatrix} f_{1,1}(u) + f_{1,2}(u) + f_{1,3}(u) + f_{B1,1}(u) \\ f_{1,4}(u) + f_{B1,2}(u) \\ f_{2,1}(u) + f_{2,2}(u) + f_{2,3}(u) + f_{B2,1}(u) \\ f_{2,4}(u) + f_{B2,2}(u) \\ f_{N,1}(u) + f_{N,2}(u) + f_{BN,1}(u) \\ f_{BN,2}(u) \end{pmatrix},$$

with

$$S_{1,1_{i,j}} = \xi^2 \int_{S_1} \nabla\phi_{S_1,i} \cdot \nabla\phi_{S_1,j} dS, \tag{A.13}$$

$$S_{1,2_{i,j}}(u) = \xi^2 \int_{S_1} \sin^2\tilde{\theta}_{S_1} \nabla\phi_{S_1,i} \cdot \nabla\phi_{S_1,j} dS, \tag{A.14}$$

$$f_{1,1_i}(u) = -\xi^2 \int_{S_1} \sin\tilde{\theta}_{S_1} \cos\tilde{\theta}_{S_1} \nabla\tilde{\chi}_{S_1} \cdot \nabla\tilde{\chi}_{S_1} \phi_{S_1,i} dS, \tag{A.15}$$

$$f_{1,2_i}(u) = \int_{S_1} iE \sin\tilde{\theta}_{S_1} \phi_{S_1,i} dS, \tag{A.16}$$

$$f_{1,3_i}(u) = \int_{S_1} \frac{1}{2} \cos\tilde{\theta}_{S_1} \Big[\Delta \exp(-i\tilde{\chi}_{S_1}) + \Delta^* \exp(i\tilde{\chi}_{S_1})\Big] \phi_{S_1,i} dS, \tag{A.17}$$

$$f_{1,4_i}(u) = \int_{S_1} \frac{1}{2i} \sin\tilde{\theta}_{S_1} \Big[\Delta \exp(-i\tilde{\chi}_{S_1}) - \Delta^* \exp(i\tilde{\chi}_{S_1})\Big] \phi_{S_1,i} dS, \tag{A.18}$$

$$f_{B1,1_i}(u) = \frac{\xi\gamma}{\gamma_B} \int_{\Gamma_{SN}} \Big[\sin\tilde{\theta}_N \cos\tilde{\theta}_{S_1} \cos\Big(\tilde{\chi}_N - \tilde{\chi}_{S_1}\Big) - \cos\tilde{\theta}_N \sin\tilde{\theta}_{S_1}\Big] \phi_{S_1,i} d\Gamma, \tag{A.19}$$

$$f_{B1,2_i}(u) = \frac{\xi\gamma}{\gamma_B} \int_{\Gamma_{SN}} \Big[\sin\tilde{\theta}_N \sin\tilde{\theta}_{S_1} \sin\Big(\tilde{\chi}_N - \tilde{\chi}_{S_1}\Big) \phi_{S_1,i} dS. \tag{A.20}$$

The element matrices and vectors in the S_2 and N layers are similar. Since this weak formulation is differentiable with respect to θ and χ, both the Newton method and the Picard method can readily be applied to solve this system of equations.

A.2.2 Comparison of iterative solvers

In this section we compare the three different fixed-point algorithms we developed to investigate which solver is the most convenient for the θ, χ-parametrization. In Figure A.2 the convergence graphs of these fixed-point methods are shown. The calculations were performed for a real value of the energy E.

Both the Picard iteration and the Anderson accelerated Picard iteration perform poorly. The reason is that the Usadel equation now contains singular (or at least very large) solutions, which violate the contraction property that is needed for the Picard iteration to converge. The Newton method with line search performs as expected. In the last few iterations the convergence is clearly quadratic. In the first few iterations this is not yet the case because of the small step size that the line search algorithm gives.

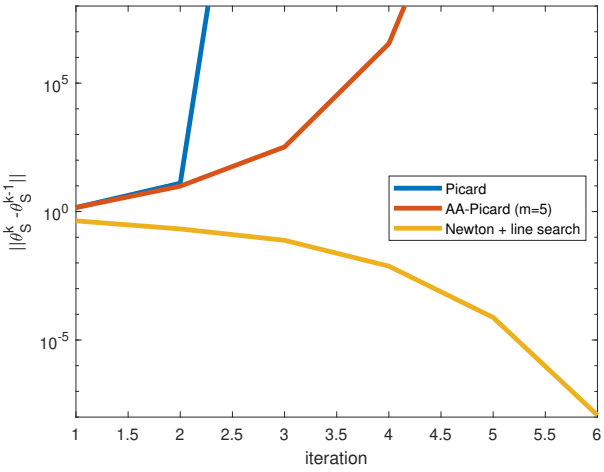

Figure A.2: Convergence graphs for different fixed-point methods applied to the Usadel equations in the θ, χ-parametrization.

A.3 Riccati parametrization

A.3.1 Weak formulation and system of equations

In this section we consider the Usadel equations in the Riccati parametrization (5.9)-(5.20) on the SN-N-NS junction shown in Figure 4.1. To derive the weak formulation we consider these equations in the S_1 region:

PDE :

In S_1 :

$$-\xi^2\nabla^2\alpha_S - \xi^2 N_S\beta_S(\nabla\alpha_S)^2 = iE\alpha_S + \frac{\Delta}{2} - \alpha_S^2\frac{\Delta^*}{2}, \tag{A.21}$$

$$-\xi^2\nabla^2\beta_S - \xi^2 N_S\alpha_S(\nabla\beta_S)^2 = iE\beta_S - \frac{\Delta^*}{2} + \beta_S^2\frac{\Delta}{2}, \tag{A.22}$$

BCs :

On Γ_I :

$$\nabla\alpha_S\cdot\mathbf{n} = 0, \tag{A.23}$$

$$\nabla\beta_S\cdot\mathbf{n} = 0, \tag{A.24}$$

On Γ_{SN} :

$$\gamma_B \xi \nabla \alpha_S \cdot \mathbf{n} = \gamma(\alpha_N - \alpha_S)(1 - \alpha_S\beta_N)N_N, \quad \text{(A.25)}$$

$$\gamma_B \xi \nabla \beta_S \cdot \mathbf{n} = \gamma(\beta_N - \beta_S)(1 - \beta_S\alpha_N)N_N, \quad \text{(A.26)}$$

On Γ_- :

$$\alpha_S = \frac{\Delta_0 e^{-i\varphi/2}}{-iE + \sqrt{\Delta_0^2 - E^2}}, \quad \text{(A.27)}$$

$$\beta_S = \frac{-\Delta_0 e^{i\varphi/2}}{-iE + \sqrt{\Delta_0^2 - E^2}} \quad \text{(A.28)}$$

Following the standard approach and by applying the natural boundary conditions the weak formulation of the Usadel equations in the Riccati parametrization can be found to be

$$\xi^2 \int_{S_1} \nabla\alpha_S \cdot \nabla\eta_S dS - \int_{S_1} \eta_S \big[2N_S\beta_S(\nabla\alpha_S)^2 + iE\alpha_S - \alpha_S^2\frac{\Delta^*}{2}\big]dS \quad \text{(A.29)}$$
$$+ \frac{\xi\gamma}{\gamma_B}\int_{\Gamma_{SN}} \eta_S\alpha_S N_N\big[1 - \alpha_S\beta_N + \alpha_N\beta_N\big]d\Gamma = \int_{S_1}\frac{\Delta}{2}\eta_S dS + \frac{\xi\gamma}{\gamma_B}\int_{\Gamma_{SN}} N_N\alpha_N\eta_S d\Gamma,$$

and

$$\xi^2 \int_{S_1} \nabla\beta_S \cdot \nabla\eta_S dS - \int_{S_1} \eta_S \big[2N_S\alpha_S(\nabla\beta_S)^2 + iE\beta_S + \beta_S^2\frac{\Delta}{2}\big]dS \quad \text{(A.30)}$$
$$+ \frac{\xi\gamma}{\gamma_B}\int_{\Gamma_{SN}} \eta_S\beta_S N_N\big[1 - \beta_S\alpha_N + \beta_N\alpha_N\big]d\Gamma = -\int_{S_1}\frac{\Delta^*}{2}\eta_S dS + \frac{\xi\gamma}{\gamma_B}\int_{\Gamma_{SN}} N_N\beta_N\eta_S d\Gamma.$$

Subsequently, the solutions can be expanded into the Lagrangian basis functions

$$\alpha_{S_1} \approx \tilde{\alpha}_{S_1} = \sum_{j=1}^{n_{S_1}} \alpha_{1,j}\phi_{S_1,j}, \qquad \beta_{S_1} \approx \tilde{\beta}_{S_1} = \sum_{j=1}^{n_{S_1}} \beta_{1,j}\phi_{S_1,j},$$

$$\alpha_{S_2} \approx \tilde{\alpha}_{S_2} = \sum_{j=1}^{n_{S_2}} \alpha_{2,j}\phi_{S_2,j}, \qquad \beta_{S_2} \approx \tilde{\beta}_{S_2} = \sum_{j=1}^{n_{S_2}} \beta_{2,j}\phi_{S_2,j},$$

$$\alpha_N \approx \tilde{\alpha}_N = \sum_{j=1}^{n_N} \alpha_{N,j}\phi_{N,j}, \qquad \beta_N \approx \tilde{\beta}_N = \sum_{j=1}^{n_N} \beta_{N,j}\phi_{N,j}.$$

Using these expansions the weak formulation for the complete junction can be turned into the following system of equations

$$S(u)u = f(u),$$

with

$$S(u) = \text{diag}\begin{pmatrix} S_{1,1} + S_{1,2}(u) + S_{1,3} + S_{1,4} + B_{1,1}(u) + B_{1,2}(u) + B_{1,3}(u) \\ S_{1,5} + S_{1,6}(u) + S_{1,7} + S_{1,8} + B_{1,4}(u) + B_{1,5}(u) + B_{1,6}(u) \\ S_{2,1} + S_{2,2}(u) + S_{2,3} + S_{2,4} + B_{2,1}(u) + B_{2,2}(u) + B_{2,3}(u) \\ S_{2,5} + S_{2,6}(u) + S_{2,7} + S_{2,8} + B_{2,4}(u) + B_{2,5}(u) + B_{2,6}(u) \\ S_{N,1} + S_{N,2}(u) + S_{N,3} + B_{N,1}(u) + B_{N,2}(u) + B_{N,3}(u) \\ S_{N,5} + S_{N,6}(u) + S_{N,7} + B_{N,4}(u) + B_{N,5}(u) + B_{N,6}(u) \end{pmatrix}$$

$$u = \begin{pmatrix} \tilde{\alpha}_1 \\ \tilde{\beta}_1 \\ \tilde{\alpha}_2 \\ \tilde{\beta}_2 \\ \tilde{\alpha}_N \\ \tilde{\beta}_N \end{pmatrix}$$

$$f(u) = \begin{pmatrix} f_{1,1} + f_{B1,1}(u) \\ f_{1,2} + f_{B1,2}(u) \\ f_{2,1} + f_{B2,1}(u) \\ f_{2,2} + f_{B2,2}(u) \\ f_{BN,1}(u) \\ f_{BN,2}(u) \end{pmatrix},$$

with

$$S_{1,1_{i,j}} = \xi^2 \int_{S_1} \nabla\phi_{S_1,i} \cdot \nabla\phi_{S_1,j} dS, \tag{A.31}$$

$$S_{1,2_{i,j}}(u) = -\int_{S_1} 2N_{S_1}\tilde{\beta}_{S_1} \nabla\tilde{\alpha}_{S_1} \cdot \nabla\phi_{S_1,j}\phi_{S_1,i} dS, \tag{A.32}$$

$$S_{1,3_{i,j}} = -\int_{S_1} iE\phi_{S_1,i}\phi_{S_1,j} dS, \tag{A.33}$$

$$S_{1,4_{i,j}} = \int_{S_1} \tilde{\alpha}_{S_1} \frac{\Delta^*}{2} \phi_{S_1,i}\phi_{S_1,j} dS, \tag{A.34}$$

$$B_{1,1_{i,j}}(u) = \frac{\xi\gamma}{\gamma_B} \int_{\Gamma_{SN}} N_N \phi_{S_1,i}\phi_{S_1,j} d\Gamma, \tag{A.35}$$

$$B_{1,2_{i,j}}(u) = -\frac{\xi\gamma}{\gamma_B} \int_{\Gamma_{SN}} N_N \tilde{\alpha}_{S_1}\tilde{\beta}_N \phi_{S_1,i}\phi_{S_1,j} d\Gamma, \tag{A.36}$$

$$B_{1,3_{i,j}}(u) = \frac{\xi\gamma}{\gamma_B} \int_{\Gamma_{SN}} N_N \tilde{\alpha}_N\tilde{\beta}_N \phi_{S_1,i}\phi_{S_1,j} d\Gamma, \tag{A.37}$$

$$f_{1,1_i} = \int_{S_1} \frac{\Delta}{2} \phi_{S_1,i} dS, \tag{A.38}$$

$$f_{B1,1_i}(u) = \frac{\xi\gamma}{\gamma_B} \int_{\Gamma_{SN}} N_N \tilde{\beta}_N \phi_{S_1,i} d\Gamma. \tag{A.39}$$

The rest of the matrices and vectors can be obtained from (A.31)-(A.39) by the substitutions $\alpha \leftrightarrow \beta, \Delta \rightarrow -\Delta^*$. The matrices and vectors in the S_2 and N layers are similar. The resulting system of equations can iteratively be solved using a fixed-point method.

A.3.2 Comparison of iterative solvers

A comparison of the three fixed-point methods discussed in section 3.5 is shown in Figure A.3. This figure shows that the Riccati parametrization is much more stable than the θ, χ-parametrization, since now all three fixed-point methods converge well. The Picard method converges linearly as predicted, but the convergence is quite slow. In this setting it is advantageous to apply Anderson acceleration, which significantly increases the rate of convergence. The fastest method both in the number and iterations and in the overall computing time is, however, still the Newton method with line search, although due to the line search algorithm it seems to only converge quadratically in the last two iterations when the iterates are already very close to the real solution.

In some cases, especially when the energy is close to the superconducting energy gap, the Picard method does not converge. In general, the Newton method with line search is the best performing method.

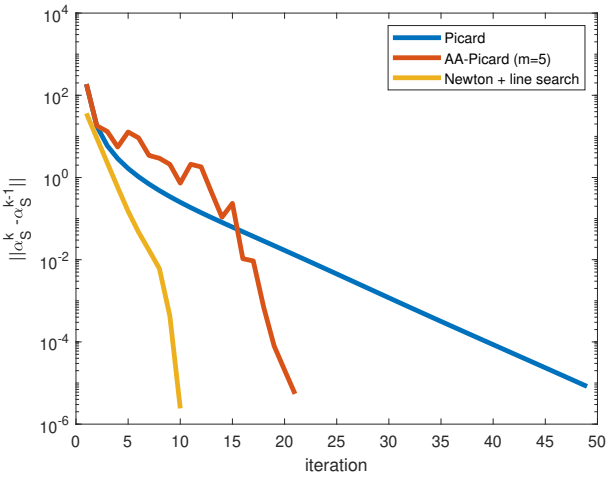

Figure A.3: Convergence graphs for different fixed-point methods applied to the Usadel equations in the Riccati parametrization.

Appendix B

Glossary

B.1 List of symbols

Symbol	Meaning	Unit
D	Diffusion constant	m^2/s
d	Junction thickness	m
e	Elementary charge	C
E	Energy	eV
E_F	Fermi energy	eV
F	Anomalous Green's function	-
G	Regular Green's function	-
H	Exchange field	eV
I_c	Critical current	A
I_s	Supercurrent	A
L	Normal metal length	m
N	Density of states	$eV^{-1}m^{-1}$ or $eV^{-1}m^{-2}$
R_N	Normal state resistance	Ω
s	Electrode spacing	m
T	Temperature	K
T_c	Critical temperature	K
W	Junction width	m
α	Riccati Green's function	-
β	Riccati Green's function	-
Γ	Domain boundary	-
γ	Proximity parameter	-
γ_B	Boundary transparency parameter	-
Δ	Energy gap	eV
θ	θ, χ Green's function	-

ξ	Coherence length	m
ρ	Normal state resistivity	Ωm
Φ	Φ Green's function	eV
φ	Phase difference	-
χ	θ, χ Green's function	-
Ω	Computational domain	-
ω_n	Matsubara frequency	-